Multifractal Analysis of the Performance of Thermally Sprayed Icephobic Coatings

Milad Hassani

A Thesis

in

The Department

of

Mechanical, Industrial and Aerospace Engineering (MIAE)

Presented in Partial Fulfillment of the Requirements

for the Degree of

Master of Applied Science (Mechanical Engineering) at

Concordia University

Montréal, Québec, Canada

January 2026

CONCORDIA UNIVERSITY

School of Graduate Studies

This is to certify that the thesis prepared

By: **Milad Hassani**

Entitled: **Multifractal Analysis of the Performance of Thermally Sprayed Icephobic Coatings**

and submitted in partial fulfillment of the requirements for the degree of

Master of Applied Science (Mechanical Engineering)

complies with the regulations of this University and meets the accepted standards with respect to originality and quality.

Signed by the Final Examining Committee:

______________________________ Chair
Dr. Navid Sharifi

______________________________ External Examiner
Dr. Pantcho Stoyanov

______________________________ Examiner
Dr. Navid Sharifi

______________________________ Supervisor
Dr. Moussa Tembely

Approved by ______________________________
Muthukumaran Packirisamy, Chair
Department of Mechanical, Industrial and Aerospace Engineering (MIAE)

____________ 2026

____
Mourad Debbabi, Dean
Faculty of Engineering and Computer Science

Abstract

Multifractal Analysis of the Performance of Thermally Sprayed Icephobic Coatings

Milad Hassani

Ice accretion remains a critical hazard in aerospace, transportation, and energy applications, and both the design of durable passive coatings and the reliable prediction of ice adhesion remain open challenges. In this work, a comprehensive experimental characterization is performed, from coating deposition to macroscopic icing, in order to link surface microstructure to icephobic performance. Titanium dioxide (TiO_2) coatings were deposited on aluminum substrates by Suspension Plasma Spraying (SPS) to create a library of icephobic surfaces. The resulting multiscale topographies were characterized by confocal profilometry and scanning electron microscopy (SEM); wettability measurements (static, advancing, and receding contact angles); droplet contact time; freezing delay in a controlled chamber; and shear ice adhesion measured after icing-wind-tunnel accretion. Multifractal analysis of the coatings yielded two scale-independent descriptors: the fractal dimension D and the scaling constant G. Despite all fabricated coatings being superhydrophobic, their ice-adhesion strengths varied widely, and no clear trend was observed with contact angles alone. In contrast, the fractal parameters D and G showed strong, monotonic correlations with key icephobic performance metrics, including shear ice-adhesion strength and droplet freezing-delay time. To the best of our knowledge, this study is the first to report a direct quantitative correlation between multifractal surface descriptors and icing outcomes for thermally sprayed coatings. Surfaces that combined a relatively high fractal dimension and low scaling constant consistently yielded the best icephobic performance. These multiscale surface features promote a stable Cassie–Baxter, thereby delaying ice nucleation and reducing ice adhesion. These findings outline a promising design pathway for engineering robust, scalable anti-icing coatings by tailoring surface microstructure.

Acknowledgments

The completion of this thesis, and the successful navigation of my graduate studies, was made possible only through the significant academic and personal support of numerous individuals. I wish to offer my most sincere and lasting gratitude to those who guided, encouraged, and sustained me throughout this endeavor.

I owe my deepest academic and professional appreciation to my primary thesis supervisor, Dr. Moussa Tembely, whose continuous mentorship was truly instrumental. His expert scientific guidance, detailed academic advice, and remarkable enthusiasm provided the necessary structure and inspiration for this research. Beyond the technical aspects of this program, I am grateful for the enduring lessons in professionalism, commitment, creativity, and kindness—principles that have shaped my outlook far beyond the scope of this work.

This academic journey would not have been sustainable without the unwavering, foundational support of my family. To my mother and father, I am forever indebted for the unconditional love, enduring encouragement, and firm foundation that allowed me the emotional space to pursue this degree. Their constant encouragement motivated me to succeed.

Finally, my sincere thanks extend to my exceptional network of colleagues and friends, including Dr. Navid Sharifi, Dr. Mohammad Mahdi Nassiri, Dr. Fadhel Ben Ettouil, and Golnoush AsadianKouhidehkordi. Their mutual support, intellectual collaboration, and genuine friendship enriched the environment and offered essential relief and motivation during the most challenging periods of research.

To all, thank you for being an indispensable part of this academic and personal achievement.

Contents

List of Figures

List of Tables

Chapter 1

Introduction

1.1 The Impact of In-Flight Icing on the Aerospace Industry

Aircraft icing remains one of the most persistent and corrosive meteorological hazards to aviation safety. Recognized as a significant operational hazard since the 1920s, the formation of ice on critical flight surfaces is an active area of research and represents a significant operational and economic burden on the aerospace and aviation industries (Yamazaki, Jemcov, & Sakaue, 2021). The ice that forms on an aircraft can fundamentally alter its carefully engineered aerodynamic properties, leading to degraded performance, reduced stability and control, and, in extreme cases, catastrophic accidents. Beyond the direct threat to human life, icing imposes considerable economic costs through flight delays, diversions, icing-mitigation procedures, and design penalties that persist throughout an aircraft's service life.

1.1.1 Aerodynamic Degradation and Flight Safety

The fundamental risk of in-flight icing is realized in its direct and adverse effect on the aerodynamics of an aircraft. Even small ice accretions can disrupt the laminar flow of air over lift-generating surfaces, altering the aircraft's performance envelope and handling qualities (Ratvasky et al., 2008). Aerodynamically, ice accretion is commonly associated with three major penalties: a severe reduction in lift, a large increase in drag, and a decrease in the angle of attack at which the aircraft stalls.

Ice accretion on the leading edge of a wing or tail surface changes the local airfoil shape and increases surface roughness. This combination promotes earlier flow separation on the upper surface of the airfoil, especially at higher angles of attack (S. Li & Paoli, 2022). The result is a significant reduction in the maximum lift coefficient, $C_{L_{\max}}$. Wind-tunnel tests and flight data show that ice contamination can reduce $C_{L_{\max}}$ by 30–40% or more (Ratvasky et al., 2008). This reduction in lift margin directly translates into an increased stall speed. For example, a clean wing that stalls at 110 kt can experience an increase in stall speed to around 140 kt when contaminated by icing, dramatically shrinking the safety margins during critical phases of flight such as takeoff, approach, and landing (Golding, 2004).

In addition to reduced lift, ice accretion can cause a pronounced increase in drag. This is due both to increased form drag, as the iced shape deviates from the intended aerodynamic profile, and to higher skin-friction drag arising from the rough ice surface. In severe icing conditions, total drag can increase by 47–200% (Ratvasky et al., 2008). To maintain altitude and airspeed under such conditions, pilots must increase engine thrust, which directly increases fuel consumption and reduces aircraft range and endurance (Grzegorczyk, Wajszczak, & Galas, 2013). In some cases, there may be insufficient thrust available to overcome the drag penalty, leading to an uncontrolled loss of airspeed and altitude (Golding, 2004).

Performance is not the only concern. Ice accretion can also severely degrade aircraft stability and control. In-flight icing can reduce the effectiveness of control surfaces (ailerons, elevators, and rudders) and alter control-surface hinge moments, as illustrated in Figure 1.1, which shows the degradation of roll control authority observed in wind-tunnel tests (Ratvasky et al., 2008). Ice accretion can degrade natural aerodynamic damping and make it more difficult for a pilot or autopilot to maintain stable flight (Ratvasky et al., 2008). Two especially hazardous scenarios are asymmetric wing icing and tailplane icing. Asymmetric icing, where ice accumulates at different rates on the left and right wings, can generate large rolling moments that exceed aileron authority and cause an uncontrollable roll (Corcione, De Marco, & Cusati, 2024). Tailplane icing can lead to tailplane stall, typically aggravated by increased downwash from deployed flaps during landing. In this condition, the horizontal tail stalls, producing a sudden, large, and often unrecoverable nose-down pitching moment (Gent, Dart, & Cansdale, 2000).

The danger of icing is compounded by its subtlety and nonlinearity. Ice accretion is not always uniform or gradual, and its aerodynamic effects may not be immediately apparent to the crew. Stall warning systems are calibrated for clean wings and may provide insufficient or no warning that a stall is imminent under icing conditions. The aircraft may stall at a much higher airspeed and lower angle of attack than the pilot expects (Golding, 2004). What begins as a performance problem can quickly escalate into a flight-control problem, as the aircraft's handling qualities change without the pilot's awareness and standard procedures become ineffective. This subtle and progressive degradation makes loss of control in flight the most common and severe outcome of icing-related accidents (Reehorst, Jr., & Colantonio, 2010).

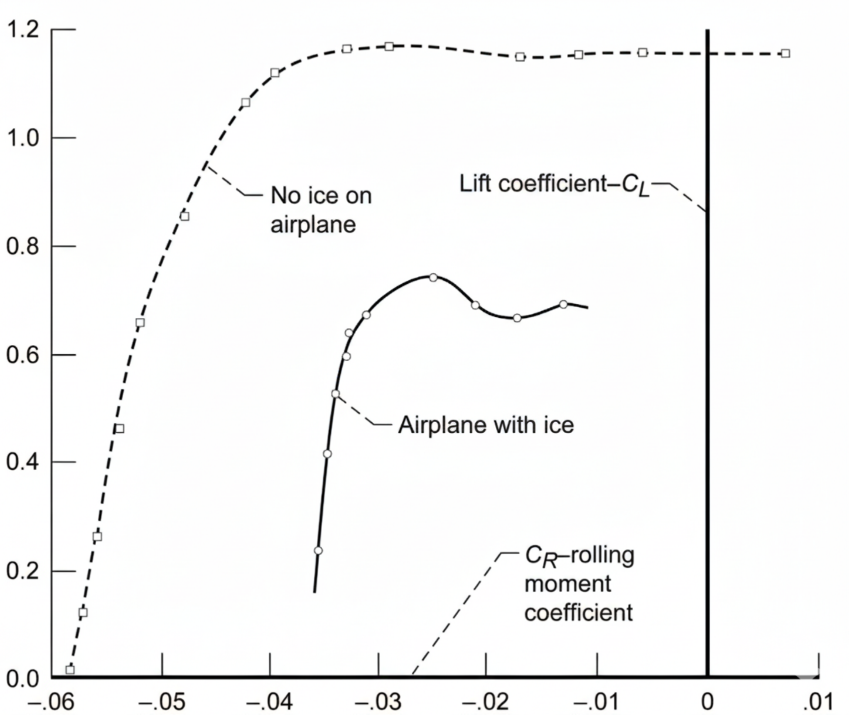

Figure 1.1: Effect of Icing on Aircraft Roll Control.(Ratvasky et al., 2008)

1.1.2 History of Icing-Related Aviation Accidents

The aerodynamic principles outlined above have been tragically confirmed by decades of accident history. Statistical data and accident investigations show that icing has been a persistent contributing factor in hundreds of accidents and thousands of fatalities worldwide. In the United

States alone, from 1982 to 2000, in-flight icing was a factor in 583 accidents, resulting in over 800 fatalities (Petty & Floyd, 2004). Analysis of NTSB data from 2000 to 2019 indicates a small, though not statistically significant, decrease in the rate of icing-related accidents; however, the proportion of these accidents that are fatal has remained high, with more than half resulting in fatalities over that two-decade span (Boyd & Guinn, 2024). While catastrophic icing accidents involving large commercial transport aircraft are rare, the potential for disaster remains. Between 1998 and 2007, more than 600 icing-related incidents involving large commercial airplanes were reported to NASA's Aviation Safety Reporting System (ASRS), underscoring that such events are still frequent precursors to serious incidents and accidents (Safety, 2010).

Several major accidents have served as watershed events, prompting improvements in regulations, aircraft design, and pilot training related to in-flight icing. The 1994 crash of American Eagle Flight 4184 highlighted the unique risks of supercooled large droplet (SLD) conditions, in which ice accumulated aft of the wing's protected region. This led to a loss of control and ultimately to new, more stringent FAA certification rules for icing, especially in SLD conditions (Yamazaki et al., 2021). Similarly, the 1997 crash of Comair Flight 3272 demonstrated that even relatively thin layers of ice could raise stall speeds to critical levels, prompting changes in operating procedures that emphasize maintaining higher airspeeds in known or suspected icing conditions (Golding, 2004).

These historical lessons motivate a deeper understanding of how ice forms and evolves on aircraft surfaces. The next section therefore examines the underlying physics of in-flight ice accretion and the different types of ice morphologies that result.

1.2 The Physics of In-Flight Ice Accretion

Effective mitigation of aircraft icing requires a clear understanding of the physical processes that drive ice formation. Ice accretion during flight is a complex thermo-fluid dynamic phenomenon that arises when aircraft encounter specific combinations of atmospheric conditions. The resulting ice geometry – its shape, density, and adhesion strength –is governed by a delicate interplay between meteorological parameters and aircraft operating conditions. These geometric characteristics, in turn, determine the aerodynamic penalty to the aircraft. This section first describes the fundamental mechanisms of in-flight ice formation and then characterizes the principal structural ice types.

1.2.1 Ice Formation Mechanism during Flight

In-flight icing occurs primarily when an aircraft flies through clouds containing supercooled liquid water droplets, i.e., droplets that remain liquid at temperatures below 0°C (Ratvasky et al., 2008). When these droplets impinge on the forward-facing surfaces of the aircraft, they may freeze on impact and form ice. The characteristics of the resulting ice depend on the local meteorological conditions and the thermodynamic heat balance at the surface.

The key meteorological parameters are the liquid water content (LWC) and the mean volume diameter (MVD) of the droplets (Ratvasky et al., 2008). LWC controls the mass flux of water available for freezing, while MVD characterizes droplet size. Larger droplets, particularly supercooled large droplets (SLDs), have greater inertia and can travel farther around the airfoil before impacting, leading to ice accretion that extends beyond the leading edge and often into regions not protected by traditional de-icing systems (Yamazaki et al., 2021). Outside air temperature (OAT) is also a dominant factor; the most hazardous icing conditions typically occur between 0°C and -20°C (Britton & Bond, 1991).

The type and morphology of the ice that forms are controlled by the surface heat balance, often described by the Messinger model (Grzegorczyk et al., 2013). This model equates the heat added to the surface (from the latent heat of fusion and kinetic heating of impinging droplets) with the heat removed (by convection, evaporation, and radiation). If most of the droplet's water freezes immediately upon impact, rime ice forms. If a significant portion remains liquid and flows along the surface before freezing, glaze ice results. In intermediate conditions, mixed ice forms, exhibiting characteristics of both rime and glaze.

1.2.2 In-Flight Ice Type Characterization

The combination of meteorological and thermodynamic factors discussed above gives rise to three principal types of structural ice, each with distinct physical characteristics and associated aerodynamic penalties. Their morphologies and visual appearances are illustrated in Figure 1.2 (Farabello et al., 2024), and their key properties are summarized in Table 1.1

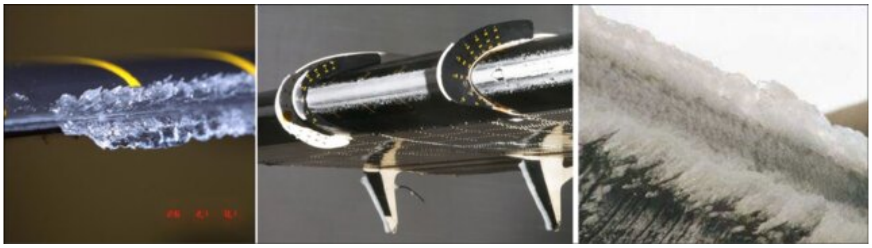

Figure 1.2: Morphologies of In-Flight Ice Accretion: from left to right, glaze ice, rime ice, and mixed ice (Farabello et al., 2024).

Rime Ice

Rime ice typically forms in colder conditions, at temperatures below about -15°C, from small supercooled droplets that freeze almost instantaneously upon impact (S. Li & Paoli, 2022). Rapid freezing traps air within the solidifying structure, giving rime ice a milky-white, opaque appearance and a brittle, relatively low-density morphology (Golding, 2004). Because there is little or no liquid water available to flow downstream, rime ice tends to conform closely to the original airfoil leading edge (Sun, Liu, Li, & Zhang, 2024). While its rough surface significantly increases drag, its conformal shape generally produces less severe shape distortion than glaze or mixed ice. Its brittle structure also makes rime ice comparatively easier to shed or remove, either mechanically or by thermal de-icing (Britton & Bond, 1991).

Glaze Ice

Glaze ice forms at warmer sub-zero temperatures, typically between 0 and -10°C, and is associated with larger droplets and higher LWC (S. Li & Paoli, 2022). In this regime, only a portion of the droplet mass freezes on impact; the remaining liquid forms a thin film that flows (or "runs back") along the surface before freezing (Cebeci & Kafyeke, 2003). This sequence produces a dense, transparent or translucent ice layer with complex shapes, including prominent horns that protrude into the oncoming airflow (Golding, 2004). These horns act as powerful aerodynamic spoilers, greatly reducing lift, increasing drag, and altering local flow separation behavior. Because of its irregular geometry and strong adhesion, glaze ice is widely regarded as the most dangerous form of in-flight icing (S. Li & Paoli, 2022).

Mixed Ice

Mixed ice forms under conditions intermediate between those that favor rime and glaze, typically from about $-10°\text{C}$ to $-20°\text{C}$. It consists of a heterogeneous combination of rime-like and glaze-like structures, giving it a rough, lumpy, whitish appearance (Cebeci & Kafyeke, 2003). Mixed ice is generally dense and strongly adherent. Aerodynamically, it can represent a worst-case scenario, combining the shape distortion and horn formation associated with glaze ice with the pronounced roughness of rime ice (Sun et al., 2024).

The underlying ice accretion process is a nonlinear, multiphase flow problem and is strongly path-dependent (Bragg, Hutchison, & Merret, 2000). Initial ice formation modifies both the thermal and aerodynamic boundary conditions, which in turn alters subsequent ice growth. For example, an initial layer of rime ice can act as an insulating layer that reduces heat transfer from the surface, causing later accretion to transition to more glaze-like forms (S. Li & Paoli, 2022). This feedback mechanism makes the system highly sensitive to initial conditions and notoriously challenging to model accurately. In particular, precise prediction of glaze ice shapes remains a significant challenge for computational icing tools (Milani et al., 2024).

Table 1.1: Characteristics of common in-flight ice types.

Characteristic	Rime Ice	Glaze Ice	Mixed Ice
Formation Temp.	< -15°C	0 to -10°C	-10 to -20°C
LWC / MVD	Low LWC, small droplets	High LWC, large droplets	Variable
Formation Physics	Instant freezing on impact	Partial freezing & runback before freezing	Combination of rime & glaze processes
Appearance	Opaque, milky-white	Transparent, dense, irregular horns	Lumpy, whitish, rough
Shape/Morphology	Conforms to airfoil shape	Horns protruding into airflow	Combination of rime and glaze features
Adhesion	Brittle, easier to remove	Strong adhesion, difficult to remove	Strong adhesion, unpredictable morphology
Primary Hazard	Moderate drag increase	Severe aerodynamic penalties	Combines worst-case features

1.3 Superhydrophobic Surfaces for Wetting Control

Because in-flight icing is rooted in the tendency of supercooled water droplets to impact, spread, and adhere to a surface, one promising approach to mitigation is to engineer surfaces that strongly resist wetting. In pursuing such passive anti-icing strategies, researchers have increasingly turned to nature for inspiration. Over billions of years, evolution has enabled many organisms to develop surfaces with remarkable water-repellent properties (Ge-Zhang, Cai, Yang, Ding, & Song, 2022). The study of these biological systems, known as biomimetics, laid the foundation for the modern science of superhydrophobic surfaces (Z. Wang, Kong, Zhou, & Chen, 2022).

This section begins with the canonical example of the lotus leaf and the physical principles underlying its extreme water repellency. It then introduces wetting models that describe how surface roughness and chemistry combine to produce superhydrophobic states, before broadening the view to show how different organisms exploit a variety of wetting regimes to achieve specific functional outcomes. These natural strategies provide key design cues for engineering anti-icing surfaces.

1.3.1 Lotus Effect: Superhydrophobicity and Self-Cleaning

The surface of the lotus leaf (*Nelumbo nucifera*) is the classical example of a superhydrophobic, self-cleaning surface (Ensikat et al., 2011). The "Lotus Effect" is characterized by two primary features: a very high water contact angle (WCA), often exceeding 160°, and a very low sliding angle (SA), typically less than 5° (Latthe, Terashima, Nakata, & Fujishima, 2014). When water droplets land on the leaf, they form nearly spherical beads that roll off at the slightest tilt, collecting dust and debris and thus passively cleaning the surface (Ensikat et al., 2011).

Early investigations showed that this behavior is not solely due to unusual surface chemistry but arises from the interplay between low surface energy and a complex hierarchical topography (Y. Wang et al., 2025). The lotus leaf is not smooth; instead, its surface is covered with microscopic bumps, or papillae, with characteristic dimensions on the order of several micrometers in height (Ensikat et al., 2011). Each papilla is coated with a dense layer of epicuticular wax crystalloids, which form a secondary nanostructure of fine tubules (Ensikat et al., 2011). Scanning electron microscopy images, such as those schematically represented in Figure 1.3, reveal this hierarchical architecture, from micrometer-scale papillae to nanometer-scale wax tubules (Ensikat et al., 2011).

The combination of low surface energy and multi-scale roughness drastically reduces the solid–liquid contact area. Water droplets rest atop the peaks of the surface micro- and nanostructures, with air trapped within the valleys. The droplet thus sits on a composite solid/air interface, minimizing adhesion and enabling easy roll-off (Ge-Zhang et al., 2022). This entrapped air layer and minimized contact area are central to the Lotus Effect.

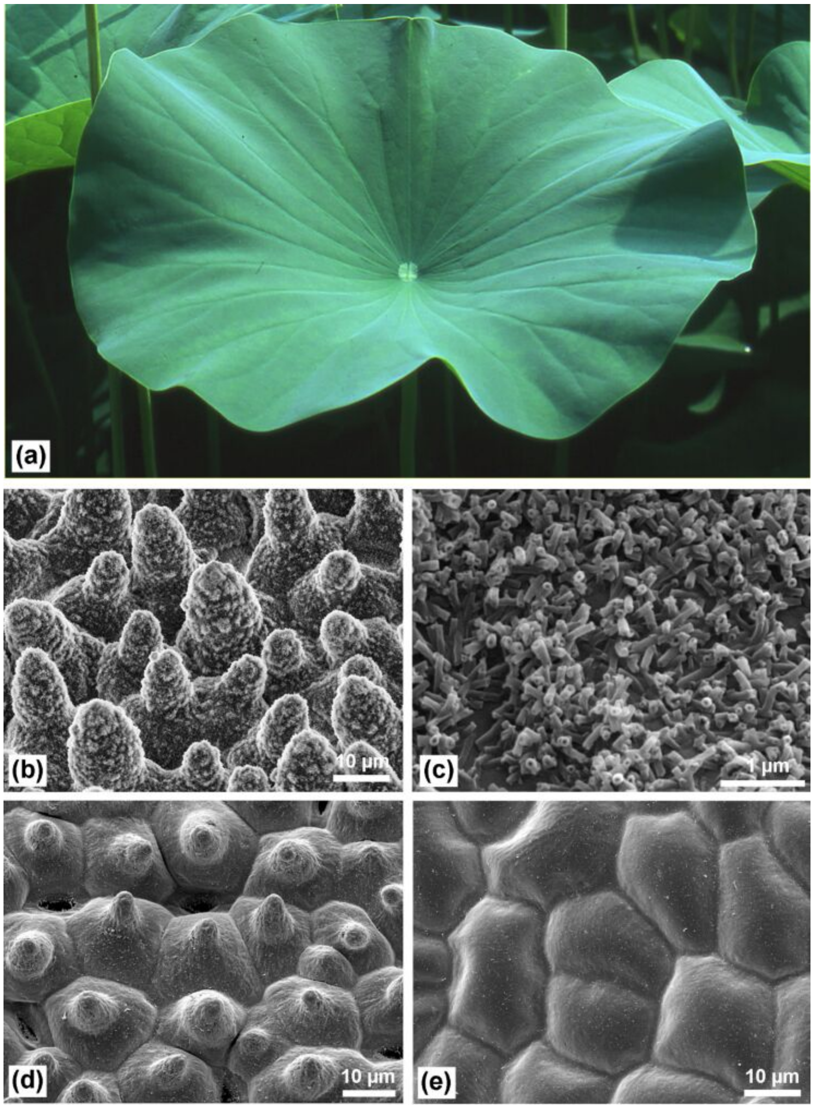

Figure 1.3: Hierarchical microstructure of a lotus leaf, showing micrometer-scale papillae covered with nanostructured wax tubules (Ensikat et al., 2011).

1.3.2 Wetting Models Relevant to Superhydrophobic Surfaces

To understand why the hierarchical roughness of the lotus leaf is so effective in producing the Lotus Effect, it is necessary to consider the basic physics of wetting. Wetting behavior arises from a balance of interfacial energies among the solid, liquid, and surrounding gas phases. This balance is strongly influenced by surface roughness, a topic that is examined in more detail in Chapter 2.

On an ideal, perfectly smooth, rigid, and chemically homogeneous surface, the equilibrium contact angle of a droplet is given by Young's equation, which relates it to the interfacial tensions between the solid–gas, solid–liquid, and liquid–gas interfaces (Z. Wang et al., 2022). However, even for materials with very low surface energy (such as fluoropolymers), the maximum achievable contact angle on a smooth surface is typically around 120° (Ge-Zhang et al., 2022), well below the 150° threshold commonly associated with superhydrophobicity. This limitation highlights the critical role of surface roughness.

Roughness can influence wetting in different ways. In the Wenzel state, the liquid fully penetrates the roughness, increasing the effective contact area and amplifying the intrinsic wettability of the material. In contrast, in the Cassie–Baxter state, the liquid rests on the tops of the roughness features, with air pockets trapped beneath. The lotus leaf operates in a Cassie–Baxter-like regime, where the droplet is supported by a composite solid–air interface. The entrapped air layer drastically reduces adhesion and stabilizes the superhydrophobic, self-cleaning state (Ge-Zhang et al., 2022; Z. Wang et al., 2022). The hierarchical micro/nanostructure of the lotus leaf is particularly effective at maintaining this Cassie–Baxter state even under dynamic conditions such as raindrop impacts.

1.3.3 Bio-Inspired Design: Diverse Natural Wetting States

Although the lotus leaf is the archetype of self-cleaning superhydrophobicity, it represents only one point in a broad design space. Nature employs a wide variety of surface topographies and chemistries to achieve distinct wetting behaviors tailored to specific functional needs (Ge-Zhang et al., 2022). Rather than being a single property, superhydrophobicity forms a tunable platform, where micro- and nanostructures can be engineered to produce low adhesion, high adhesion, directional transport, or other specialized responses.

High-Adhesion Superhydrophobicity: Rose Petal Effect

In striking contrast to the lotus leaf, the surface of a rose petal is also superhydrophobic (WCA $> 150°$) but strongly adhesive (Y. Wang et al., 2025). A water droplet placed on a rose petal remains pinned, even if the petal is inverted. This behavior arises from a different surface architecture: more widely spaced, flat-topped micropapillae, each decorated with radial nanofolds (Y. Wang et al., 2025). This geometry stabilizes a "Cassie-impregnating" state—a hybrid wetting regime in which the droplet simultaneously rests on entrapped air in the surface valleys (Cassie state) and fully wets the flat tops of the papillae (Wenzel state) (Y. Wang et al., 2025). The contact over the flat plateaus creates strong pinning and high adhesion, while the remaining air pockets maintain a high contact angle. Such high-adhesion superhydrophobic states are attractive for controlled, non-destructive liquid manipulation and transfer (Ge-Zhang et al., 2022).

Anisotropic Wetting: Rice Leaf Effect

The surface of a rice leaf offers yet another example: anisotropic, or direction-dependent, wetting (Y. Wang et al., 2025). Water droplets on a rice leaf experience low sliding angles and roll off readily in the direction parallel to the leaf veins, yet they are strongly pinned and exhibit high sliding angles in the transverse direction (Ge-Zhang et al., 2022). This anisotropy is governed by an array of parallel microgrooves aligned with the leaf veins, which guide the three-phase contact line and impose a lower energy barrier for motion along the grooves than across them (Y. Wang et al., 2025).

Rice leaves serve as a biological model for engineered surfaces designed to direct liquid transport, enabling applications such as passive droplet routing, microfluidics, and directional drainage. More broadly, the diversity of natural wetting strategies demonstrates that by carefully controlling the geometry, spacing, and hierarchy of surface features, one can tune a surface's wetting properties across a continuum: from highly repellent and self-cleaning to strongly adhesive or directionally biased.

For anti-icing applications, this insight is crucial. Simply fabricating a generic "superhydrophobic" surface is not sufficient. The surface must be designed to promote rapid shedding of impacting supercooled droplets, inhibit film formation and runback freezing, and minimize the adhesion strength of any ice that does form. Translating these bio-inspired concepts into robust, durable coatings suitable for aircraft environments requires advanced surface-engineering technologies. The next section therefore introduces thermal spray technologies as a versatile platform for realizing such functional micro- and nanostructured surfaces.

1.4 Advanced Surface Engineering via Thermal Spray Technologies

To deploy bio-inspired wetting concepts in demanding aerospace environments, it is necessary to fabricate coatings that are not only functionally sophisticated but also mechanically robust, thermally stable, and compatible with existing components. Thermal spray technologies provide a powerful family of processes for depositing such functional coatings (Tejero-Martin, Rezvani Rad, McDonald, & Hussain, 2019). Widely used in aerospace, power generation, and automotive sectors, thermal spray techniques enhance surface properties such as wear resistance, corrosion resistance, and thermal insulation (Gupta et al., 2021).

This section first reviews the fundamental principles common to all thermal spray processes, then compares the major process variants. Finally, it focuses on plasma-based methods, particularly Suspension Plasma Spray (SPS), which enable the creation of finely engineered microstructures relevant to advanced anti-icing and other functional applications.

1.4.1 Fundamental Principles of Thermal Spray Deposition

"Thermal spray" is a generic term encompassing a set of coating processes that share a common principle: a feedstock material, typically in the form of powder, wire, or rod, is heated to a molten or semi-molten state and simultaneously accelerated by a gas stream toward a prepared substrate (Fauchais, Heberlein, & Boulos, 2014). Upon impact with the cooler substrate, the droplets rapidly deform into thin, flattened lamellae known as "splats" and solidify (C.-J. Li, Yang, & Li, 2013). A coating builds up as successive splats overlap, interlock, and bond to the substrate, forming a lamellar microstructure.

Thermal spray processes offer several key advantages. First, they are extremely versatile, capable of depositing a wide range of materials, including metals, alloys, ceramics, cermets, and some polymers (Fauchais et al., 2014). In principle, any material that can be melted without excessive decomposition can be thermally sprayed. Second, because the substrate typically remains relatively cool (often below about 200°C), high-melting-point materials such as refractory ceramics can be applied to fully heat-treated and finished components without significantly altering the substrate microstructure or causing dimensional distortion (Espallargas, 2015; Fauchais et al., 2014).

The industrial relevance of these techniques is reflected in the size of the global thermal spray market, which is projected to reach approximately $13.5 billion by 2026 (Łatka et al., 2020). A principal limitation of all thermal spray processes, however, is their line-of-sight nature: they can only coat surfaces that are directly exposed to the spray plume (Fauchais et al., 2014).

1.4.2 A Comparative Analysis of Thermal Spray Processes

Thermal spray processes are primarily distinguished by their energy source (e.g., chemical combustion or electric arc), the design of the spray gun, and the resulting particle temperature and velocity regimes. Particle temperature and velocity are the most critical parameters controlling coating microstructure, density, adhesion, and residual stresses (Ang & Berndt, 2014). The main process families can be compared as follows, with their characteristic temperature–velocity ranges summarized in Figure 1.4 and their key features listed in Table 1.2.

Flame Spray

Flame spray is the oldest and one of the simplest thermal spray methods. It relies on the combustion of a fuel gas (such as acetylene) with oxygen as the heat source (Kumar & Kumar, 2018). The process can reach sufficiently high temperatures to melt most engineering metals, but the particle velocities are relatively low, typically below 150 m/s (Kuroda, Kawakita, Watanabe, & Katanoda, 2008). Advantages include low capital cost, portability, and operational simplicity. However, the relatively low kinetic energy of impacting particles generally leads to coatings with higher porosity and lower bond strength than those produced by more advanced methods (Tejero-Martin et al., 2019). Oxidation of the feedstock in the flame can also be a concern.

High-Velocity Oxy-Fuel (HVOF) Spray

Developed in the 1980s, HVOF uses continuous combustion of fuel and oxygen within a pressurized chamber, followed by expansion of the hot gases through a converging–diverging nozzle, creating a supersonic jet (Kumar & Kumar, 2018). Powder feedstock is injected into this jet and accelerated to velocities ranging from about 500 to over 1000 m/s (Kuroda et al., 2008). The flame temperature is moderate (on the order of 3000°C), but the high particle velocity yields dense, well-bonded coatings with low porosity. HVOF is particularly effective for wear- and corrosion-resistant cermet coatings such as tungsten carbide–cobalt (WC–Co) (Kumar & Kumar, 2018).

Atmospheric Plasma Spray (APS)

Atmospheric Plasma Spray (APS) is one of the most versatile thermal spray processes. It employs a high-power DC electrical arc between a cathode and anode to ionize a stream of inert gas (e.g., argon or nitrogen) into a plasma plume (Tejero-Martin et al., 2019). Plasma temperatures can exceed 16,000 K, enabling the melting of virtually any known material, including highly refractory ceramics such as zirconia (ZrO_2) and alumina (Al_2O_3) (Fauchais et al., 2014). Powder is injected into the plasma jet, where it melts and is accelerated to moderate velocities (typically 100–500 m/s). APS is widely used for thermal barrier coatings (TBCs) in gas turbines and for other high-temperature, corrosion-resistant ceramic coatings (Tejero-Martin et al., 2019).

Cold Spray (CS)

Cold spray differs fundamentally from the molten or semi-molten processes described above. It is a solid-state deposition method in which a pressurized gas (usually nitrogen or helium) is moderately heated (typically below 800°C) and expanded through a supersonic nozzle (Łatka et al., 2020). Metal powder particles injected into this gas flow are accelerated to 300–1200 m/s but remain solid (Singh, Sidhu, & Kalsi, 2012). Bonding occurs via high-strain-rate plastic deformation upon impact, which fractures surface oxide films and promotes metallurgical bonding between freshly exposed metal surfaces (Łatka et al., 2020).

The main advantage of cold spray is its low processing temperature, which minimizes oxidation, phase transformations, and thermally induced tensile residual stresses that can occur in molten-spray processes (Łatka et al., 2020). The resulting coatings are typically very dense, with excellent mechanical properties. The main limitation is that cold spray is effective primarily for ductile, plastically deformable materials; brittle materials and most ceramics cannot be deposited efficiently in this manner (Łatka et al., 2020).

Figure 1.4 qualitatively compares the temperature and velocity ranges of the principal thermal spray methods, while Table 1.2 summarizes their key characteristics and trade-offs (Ang & Berndt, 2014; Fauchais et al., 2014; Kumar & Kumar, 2018; Kuroda et al., 2008; Łatka et al., 2020; Singh et al., 2012; Tejero-Martin et al., 2019).

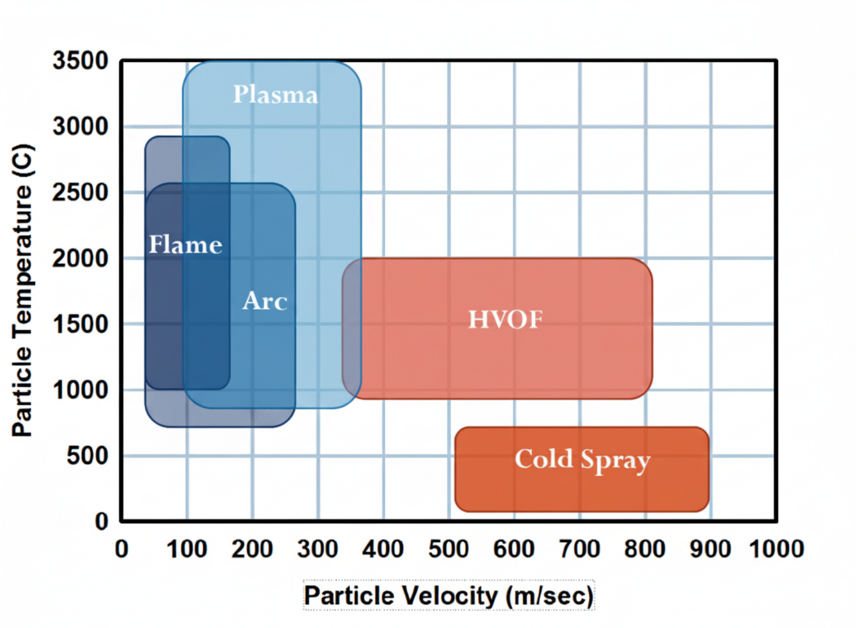

Figure 1.4: Comparison of characteristic temperature and particle velocity ranges for major thermal spray processes (Ang & Berndt, 2014).

1.4.3 Plasma Spraying: A Versatile Platform for Advanced Coatings

Among thermal spray techniques, plasma spraying stands out for its exceptionally high thermal energy and broad material compatibility (Vaßen, Kaßner, Mauer, & Stöver, 2010). A typical plasma gun consists of a tungsten-based cathode and a water-cooled copper anode. A high-frequency arc

Table 1.2: Comparison of key characteristics of major thermal spray processes.

Process	**Heat Source**	**Characteristic Temp. Range**	**Velocity Range**	**Advantages**	**Disadvantages**
Flame Spray	Chemical combustion	High (up to ∼2,500°C flame / particle)	Low (<150 m/s)	Low capital cost; simple operation; portable.	High porosity; lower bond strength; potential feedstock oxidation.
APS	DC electric arc (plasma)	Very high (plasma core >15,000 K; particles sufficient to melt refractory ceramics)	Moderate (100–500 m/s)	Can spray refractory ceramics; high deposition rates; wide material range.	Higher equipment cost; oxidation possible in atmospheric operation.
HVOF	Pressurized combustion	Moderate (∼3,000°C flame)	Very high (500–1200 m/s)	Produces dense, hard coatings with high adhesion; low porosity.	High noise levels; line-of-sight; high gas consumption.
Cold Spray	Heated supersonic gas	Low (<800°C, solid state)	Very high (300–1200 m/s)	Minimal oxidation or phase change; very dense coatings; low tensile stress.	Limited to ductile materials; high-pressure gas requirements; risk of substrate erosion below critical velocity.
SPS	DC electric arc (plasma)	Very high (similar to APS; fine particles heated in plasma jet)	Moderate (100–500 m/s)	Enables deposition of nano/submicron particles; unique microstructures (e.g., columnar, porous).	Complex suspension preparation and stability; lower deposition efficiency than powder-based APS.

struck between these electrodes ionizes the process gas (usually argon, often mixed with hydrogen or nitrogen), creating a high-temperature, electrically conductive plasma (Vaßen et al., 2010).

The plasma is forced through a constricting nozzle, forming a jet with centerline temperatures exceeding 16,000 K and moderate gas velocities. Powdered feedstock is injected, often radially, into this plasma plume, where particles are rapidly heated to a molten or semi-molten state and accelerated toward the substrate (Vaßen et al., 2010). Upon impact, they flatten into splats, cool, and solidify, forming a coating. The extreme thermal energy available in plasma spraying permits the processing of high-melting-point ceramics such as zirconia, making APS a cornerstone of modern thermal barrier coating technology in gas-turbine engines and other high-temperature applications (Tejero-Martin et al., 2019; Vaßen et al., 2010).

Building on this versatility, Suspension Plasma Spray (SPS) extends the capabilities of plasma spraying to the nanoscale, enabling finer control over coating microstructure and opening new opportunities for functional surfaces, including those tailored for anti-icing.

1.4.4 Suspension Plasma Spraying (SPS): Creating Fine and Nanostructured Surfaces

Suspension Plasma Spray (SPS) is an important advancement over conventional powder-based plasma spraying, specifically developed to address the difficulty of feeding very fine (sub-micrometer or nanometer-scale) powders through traditional powder feeders (Vaßen et al., 2010). In SPS, the feedstock is a stable liquid suspension of fine particles in a solvent such as water or ethanol, rather than a dry powder. This suspension is injected into the plasma jet, typically as a liquid stream or as droplets.

Once injected, the liquid undergoes atomization, rapid heating, and evaporation of the solvent. The liberated fine particles are then heated and accelerated toward the substrate by the plasma plume (Łatka, 2018). The sequence of processes—suspension injection, atomization, solvent evaporation, particle heating, and impact—is schematically illustrated in Figure 1.5 (Łatka, 2018).

The use of ultra-fine particles enables SPS to produce coatings with unique microstructures that are difficult or impossible to obtain with conventional APS, such as highly columnar or finely porous architectures, as well as dense nanostructured layers. These microstructures can be tailored

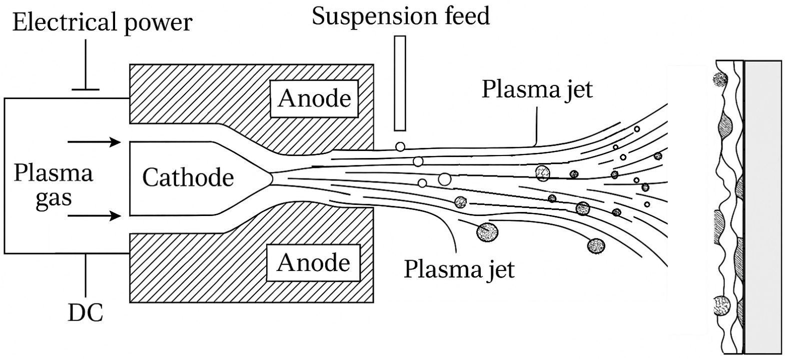

Figure 1.5: Schematic view of the Suspension Plasma Spray (SPS) process, illustrating suspension injection, solvent evaporation, and particle acceleration toward the substrate (Łatka, 2018).

to achieve specific combinations of thermal conductivity, mechanical compliance, permeability, and surface roughness. SPS is being actively investigated for thermal barrier coatings, solid oxide fuel cell electrodes, photocatalytic surfaces, and biomedical implants, among other applications (Łatka, 2018).

More broadly, the evolution from traditional molten-spray processes such as APS and HVOF to solid-state techniques like cold spray and liquid-feedstock processes like SPS represents a paradigm shift in surface engineering. The focus has moved from simply depositing a different material onto a substrate to deliberately engineering coating microstructures at the micro- and nanoscale. Many of the superior properties of modern coatings arise not only from their chemistry but from their hierarchical, finely tuned physical structure. SPS, in particular, offers a route to bio-inspired, multiscale surface architectures whose complex roughness can be quantitatively characterized using fractal geometry. This motivates a final shift in this introductory chapter: from physical processes to the mathematical tools needed to describe and analyze such complexity.

1.5 Fractal Geometry for Multiscale Surface Characterization

While the preceding sections have dealt with aerodynamics, wetting, and materials processing, they all share a common theme: complex, irregular geometries that cannot be adequately described by classical Euclidean shapes. The roughness of an ice accretion, the hierarchical structure of a lotus leaf, and the turbulent features of a plasma jet each exhibit intricate detail over multiple length scales. Euclidean geometry, with its ideal lines, circles, and planes, is poorly suited to capture such complexity. Fractal geometry, in contrast, provides a powerful framework for describing and quantifying irregular, self-similar structures in both natural and engineered systems (Samayoa, Garcia-Otamendi, & Balankin, 2025).

This section briefly introduces the historical development of fractal concepts, outlines the core ideas of self-similarity and fractal dimension, and highlights their relevance to the multiscale surfaces discussed earlier in this chapter.

The foundational ideas arose from a series of mathematical constructions developed in the late 19th and early 20th centuries, including the Weierstrass function, the Cantor set, space-filling curves such as those of Peano and Hilbert, and the Koch snowflake (Debnath, 2006; Guan, Liu, & Zhang, 2024). These objects, along with later examples like the Sierpiński gasket, shared what would later be recognized as fractal properties: fine structure at arbitrarily small scales, self-similarity, and a dimension that did not fit neatly into the integers 1, 2, or 3 (Guan et al., 2024). For many decades, they were regarded as mathematical curiosities with no obvious physical relevance.

The unifying synthesis came from Benoit Mandelbrot, who, while working at IBM in the 1960s and 1970s, exploited emerging computational power to visualize these complex sets (Debnath, 2006). In 1975, he coined the term *fractal*, from the Latin *fractus* (broken or fractured), to describe this family of shapes (Samayoa et al., 2025). His seminal 1982 book, *The Fractal Geometry of Nature*, demonstrated that such “monsters” were in fact the natural language of many real-world phenomena, from coastlines and clouds to financial markets and turbulent flows (Gaddis & Zyda, 1986).

1.5.1 Core Concepts: Self-Similarity and Fractal Dimensions

Fractal geometry is built on two central concepts that distinguish it from classical geometry: self-similarity and non-integer (fractal) dimension.

Self-Similarity

Self-similarity is the most visually intuitive feature of fractals. A set is self-similar if it is composed of smaller parts that resemble the whole in shape or structure (Guan et al., 2024). When one "zooms in" on a fractal, similar patterns recur at smaller and smaller scales (Debnath, 2006). This self-similarity can be exact, as in rigorously defined mathematical fractals like the Koch snowflake or the Sierpiński gasket, where each iteration is an exact scaled copy of the previous one. Figure 1.6 illustrates this idea using these two classic examples, both generated by simple iterative rules (Schaefer et al., 2005).

In natural systems, self-similarity is typically statistical or approximate rather than exact. For example, coastlines, mountain ranges, or branching river networks exhibit similar roughness characteristics across a wide range of scales, even though no two segments are identical (Guan et al., 2024). The same holds for many engineered surfaces where multi-scale roughness is intentionally introduced, such as plasma-sprayed coatings or biomimetic superhydrophobic layers.

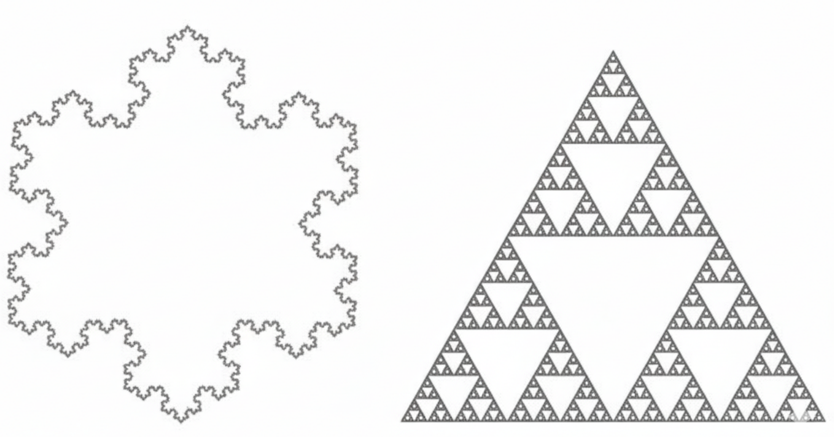

Figure 1.6: Classic examples of iteratively constructed fractals: the Koch snowflake and the Sierpiński gasket (Schaefer et al., 2005).

Fractal Dimensions

Classical geometry assigns integer topological dimensions: a line is one-dimensional (1D), a plane is two-dimensional (2D), and a solid is three-dimensional (3D) (Cannon, 1984). However, many fractal sets fall somewhere between these integers in terms of their space-filling capacity.

The Koch curve, for example, is more complex than a simple 1D line but does not fill a 2D area; its fractal dimension is approximately 1.26 (Samayoa et al., 2025). This non-integer dimension quantifies the degree of complexity or roughness of the object.

Several formal definitions of fractal dimension exist, including the Hausdorff dimension and various box-counting or Minkowski–Bouligand dimensions (Debnath, 2006). Conceptually, these definitions measure how the "apparent size" of an object (e.g., its length, area, or mass) scales with the size of the measurement unit. For a jagged coastline, for instance, the measured length increases as smaller measuring sticks are used, and the rate of this increase is related to its fractal dimension (Krantz, 1989). Higher fractal dimension corresponds to greater irregularity and more efficient filling of space.

Fractal analysis thus provides a quantitative means of describing the complex, multiscale geometries encountered in ice accretion, bio-inspired superhydrophobic surfaces, and thermally sprayed coatings. In subsequent chapters, these concepts will be employed to characterize the morphology of engineered anti-icing surfaces and to link geometrical complexity to functional performance.

1.6 Thesis Objectives

The primary aim of this research was to move beyond conventional surface characterization and establish a quantitative framework for designing icephobic coatings. Specifically, the objectives of this thesis are:

(1) **Fabricate diverse icephobic coatings:** Experimentally create a range of hierarchically structured coatings with varied nano/micro-scale roughness. This included developing novel TiO_2 surfaces via Suspension Plasma Spraying (SPS) and incorporating a commercial superhydrophobic coating as a benchmark, to obtain a broad spectrum of surface textures.

(2) **Evaluate conventional wettability metrics:** Critically assess the limitations of standard wetting measurements (e.g., static contact angle) in predicting macroscale ice adhesion strength and overall anti-icing performance.

(3) **Apply multifractal surface analysis:** Quantify the complex surface topography of all fabricated coatings using multifractal analysis. In particular, employ scale-independent roughness parameters (primarily the fractal dimension D and the scaling constant G) to characterize each coating's micro/nanostructure.

(4) **Correlate fractal parameters with performance:** Establish a clear quantitative correlation between the calculated fractal descriptors (D and G) and the coatings' icephobic performance metrics. Key metrics of interest include shear ice-adhesion strength (critical force to delaminate ice), freezing delay time, and droplet impact contact time (rebound behavior).

(5) **Identify optimal design guidelines:** Determine the combination of fractal parameters that governs superior icephobic behavior. By pinpointing the ranges of D and G associated with minimal ice adhesion and maximum icing delay, provide fundamental design guidelines for next-generation anti-icing surfaces. This objective aims to translate the observed structure–performance relationships into practical criteria for designing durable icephobic coatings.

1.7 Thesis Organization

This thesis is organized into four main chapters to address the research objectives in a systematic manner:

- **Chapter 1: Introduction** – Establishes the context and motivation for the study. This chapter details the critical challenge of in-flight icing and its detrimental impacts on aerospace operations. It provides essential background on the physics of ice accretion and introduces the concept of superhydrophobicity (including nature's Lotus Effect as inspiration). The advanced coating fabrication technique of Suspension Plasma Spraying (SPS) is outlined, and the fundamental principles of fractal geometry are presented as a tool for characterizing multiscale surface roughness.
- **Chapter 2: Literature Review (Passive Icephobic Surfaces)** – Presents a detailed review of the state-of-the-art in passive anti-icing materials and strategies. The chapter analyzes fundamental principles of ice formation and various ice mitigation approaches. It highlights how

surface chemistry and micro/nanostructure modifications influence water wettability and ice adhesion, drawing on examples from recent literature. This review establishes the knowledge gaps and rationale for applying fractal analysis to engineered icephobic coatings.

- **Chapter 3: Multifractal Analysis of Icephobic Coatings** – Describes the experimental methodology and key findings of the research. This chapter covers the fabrication of the TiO_2 SPS coatings and the preparation of the commercial reference surface, followed by the comprehensive characterization techniques used (surface profilometry, microscopy, contact angle measurements, droplet impact testing, etc.). It then presents the experimental results, including the multifractal analysis of surface profiles, and quantifies the relationships between fractal parameters (D and G) and icing performance metrics. The latter part of the chapter provides an in-depth discussion of the results, explaining the physical mechanisms by which surface texture at multiple scales affects ice formation, ice adhesion strength, and water droplet dynamics.

- **Chapter 4: Conclusions and Future Work** – Summarizes the main findings and contributions of this research, linking back to the objectives stated in Chapter 1. It provides conclusive answers to the research questions and discusses the implications of the results for the design of icephobic surfaces. Finally, this chapter proposes several future research directions, including the integration of machine learning and computational surface modeling techniques to optimize coating designs, as well as recommendations for extending the study to broader material systems and long-term durability testing.

Chapter 2

Literature Review

Manuscript under review: M. Hassani and M. Tembely, "A Comprehensive Review of Advances and Challenges in Ice Accretion on Passive Icephobic Surfaces," Processes.

Abstract

Ice accretion on aircraft, wind-turbine blades, power lines, and sensors poses serious safety risks and economic costs. Conventional countermeasures—electro-thermal heaters, pneumatic boots, and glycol-based de-icers—are energy-intensive, heavy, and provide only short-term relief. Passive icephobic surfaces aim to mitigate icing by delaying nucleation, disrupting droplet solidification, and/or weakening the ice–substrate bond so that accreted ice sheds under mild aerodynamic, gravitational, or vibrational loads. This review synthesizes recent progress in materials science, surface engineering, and mechanics to create durable icephobic coatings. The fundamental principles of ice nucleation, droplet dynamics, and accretion are outlined first, followed by an analysis of how surface chemistry and topography—from micro/nano textures to complex hierarchical structures—influence wettability and ice adhesion. Fabrication routes, including laser texturing, sol–gel and thermal-spray coatings, and slippery liquid-infused porous surfaces (SLIPS), are surveyed. Notably, SLIPS and soft elastomeric films have achieved shear ice-adhesion strengths below $\sim 20\,\mathrm{kPa}$—often an order of magnitude lower than classical superhydrophobic coatings—enabling shedding under weak loads. Standard and emerging test methods (push-off, pull-off/tensile, centrifugal) are compared, underscoring the need for harmonized protocols to enable reliable benchmarking. Case studies spanning aircraft, wind turbines, power grids, and sensors highlight demonstrated performance gains alongside durability challenges (abrasion/erosion, lubricant retention, and coating–substrate adhesion). Priorities for eco-friendly chemistries, self-healing or replaceable layers, and machine-learning-guided texture optimization are outlined, charting a path toward long-lived, energy-free ice-mitigation.

Keywords: Icephobic surfaces; ice adhesion; superhydrophobicity; SLIPS; droplet impact; Surface texturing; Durability

2.1 Introduction

Ice accumulation on exposed surfaces is a pervasive hazard across multiple sectors, with significant safety implications and economic losses Kreder, Alvarenga, Kim, and Aizenberg (2016a). In aerospace, ice accretion on wings, inlets, and engines degrades aerodynamic performance and has contributed to incidents and accidents Board (2007); Federal Aviation Administration (2021). In the energy sector, ice build-up on wind-turbine blades reduces power output and can induce hazardous imbalance, while icing on overhead lines and structures leads to outages and mechanical failures Farzaneh (2008); Gao and et al. (2021); Makkonen, Lehtonen, and Hirviniemi (2014); Parent and Ilinca (2011). Transportation infrastructure and telecommunications likewise experience ice-related degradation and downtime Brassard, Laforte, Guerin, and Blackburn (2017). Although chemical de-icers, electric heating, and mechanical removal are widely used, these active methods are energy-intensive, environmentally burdensome, and typically provide only temporary relief C. Laforte, Brassard, and Volat (2019). These limitations motivate passive icephobic surfaces, namely materials that delay the onset of freezing and/or exhibit extremely low ice-adhesion strength so that any ice that does form can be shed with minimal force Golovin et al. (2016); Susoff, Siegmann, Pfaffenroth, and Hirayama (2013).

As summarized in Figure 2.1, passive surface strategies can be broadly categorized as: (i) smooth, low-surface-energy coatings; (ii) textured surfaces, including superhydrophobic designs that minimize solid–liquid contact; (iii) slippery liquid-infused porous surfaces (SLIPS); and (iv) subsurface textured or architected substrates. Superhydrophobicity remains attractive for reducing real contact area and promoting droplet mobility Dhyani, Choi, Golovin, and Tuteja (2022), while engineered roughness/topography is the most extensively exploited lever for controlling wetting, nucleation pathways, and interfacial adhesion Yeadon, Lai, Huang, and Song (2025).

Figure 2.1: Overview of primary strategies for designing icephobic surfaces, categorized by surface properties: smooth, textured (e.g., hierarchical), slippery, and subsurface textured He et al. (2021).

Designing surfaces that are truly icephobic is challenging because ice adhesion emerges from coupled interfacial phenomena, including wetting state (Cassie vs Wenzel), contact-line pinning, impact/solidification dynamics, and interfacial fracture. This review synthesizes the state of the art with an emphasis on the mechanisms that link surface chemistry and topography to icing behavior and adhesion strength. Section 2.2 reviews the fundamentals of ice formation and adhesion, from nucleation thermodynamics to droplet impact and wetting models. Section 2.3 examines how micro/nano-scale and hierarchical roughness govern wettability, pinning, and adhesion. Section 2.4 compares ice-adhesion measurement methods (shear/push-off, tensile/pull-off, and centrifugal), highlighting artifacts and the need for standardized protocols. Section 2.5 surveys fabrication approaches (top-down texturing vs bottom-up coatings) and scale-up/durability considerations. Section 2.6 discusses low-interfacial-toughness strategies, including soft elastomeric films and SLIPS, that enable ultra-low adhesion and size-independent debonding. Section 2.7 presents application case studies (aircraft, wind turbines, power infrastructure, and sensors). Section 2.8 outlines cross-cutting challenges (durability, environmental considerations, standardization) and opportunities, including data-driven surface design, followed by Section 2.9 with concluding remarks.

2.2 Fundamentals of Ice Accretion and Adhesion

Ice formation on engineered surfaces is governed by interfacial thermodynamics, unsteady fluid and heat transfer during droplet impact, and the wetting state set by surface chemistry and topography. This section summarizes key concepts needed to interpret the performance of icephobic materials in subsequent sections.

2.2.1 Thermodynamics of Nucleation

In pure water, homogeneous nucleation of ice requires substantial supercooling, typically to about -35 to $-40\,^{\circ}\mathrm{C}$, to overcome the free energy barrier associated with creating a critical nucleus. The classical expression for the barrier to homogeneous nucleation is

$$\Delta G^*_{\mathrm{hom}} = \frac{16\pi\,\gamma_{sl}^3}{3\,(\Delta G_v)^2}, \tag{1}$$

where γ_{sl} is the solid–liquid interfacial energy and ΔG_v is the volumetric free energy difference between ice and water at the given supercooling.

Most practical icing scenarios involve heterogeneous nucleation catalyzed by a substrate or impurities, which lowers the barrier by a geometric factor $f(\theta)$ that depends on the equilibrium contact angle θ of an ice nucleus on the surface:

$$\Delta G^*_{\mathrm{het}} = f(\theta)\,\Delta G^*_{\mathrm{hom}}, \qquad 0 < f(\theta) \le 1, \tag{2}$$

with the classical spherical-cap factor on an ideal smooth surface given by Liu (2000)

$$f(\theta) = \frac{2 - 3\cos\theta + \cos^3\theta}{4}. \tag{3}$$

Hydrophilic surfaces (small θ) strongly reduce the barrier and promote early ice nucleation, whereas hydrophobic surfaces (large θ) inhibit nucleation by keeping the incipient nucleus from wetting the substrate . This thermodynamic effect delays the onset of freezing but does not, by itself, determine the eventual strength of the ice–substrate bond once solidification proceeds.

2.2.2 Droplet Impact and Solidification Dynamics

In many applications (aircraft in flight, wind turbines), supercooled droplets impinge on surfaces and either rebound, spread, or freeze during the brief contact time. The outcome is governed by inertia, viscosity, capillarity, and heat transfer, which are conveniently expressed using the dimensionless groups

$$We = \frac{\rho V^2 D}{\gamma}, \qquad Re = \frac{\rho V D}{\mu}, \qquad Ste = \frac{c_p \Delta T}{L_f}, \tag{4}$$

where ρ is the liquid density, V the impact velocity, D the droplet diameter, γ the surface tension, μ the dynamic viscosity, c_p the specific heat, ΔT the degree of supercooling relative to the melting temperature, and L_f the latent heat of fusion.

Physically, We measures inertial versus capillary forces and Re measures inertial versus viscous forces; increasing We promotes spreading and possible splashing, whereas low We favors compact shapes or rebound on non-wetting surfaces. The Stefan number Ste compares sensible to latent heat; smaller Ste indicates that freezing during contact is more likely.

Low-hysteresis hydrophobic or superhydrophobic surfaces reduce liquid residence time by promoting recoil, rebound, or roll-off, which can prevent freezing if the solidification time exceeds the contact time. On sufficiently cold substrates, however, contact freezing can occur at the initial liquid–solid contact, anchoring the droplet before it can detach. Surface texture influences these pathways: if capillary pressure forces liquid into the texture (Wenzel wetting), the benefit of non-wetting is lost and solidifying water can mechanically interlock with asperities. Thermal properties also matter. Higher Ste (more sensible heat relative to latent heat) generally lengthens the time to full solidification and increases the chance of shedding before a strong bond develops. Under harsh icing fluxes or very low ambient temperatures, some accretion is expected even on optimized non-wetting surfaces, shifting the design target from anti-icing toward low-adhesion de-icing.

2.2.3 Wetting Models and Wetting Transitions

Apparent wetting on rough surfaces is commonly described by the Wenzel and Cassie–Baxter models Figure 2.2. In the *Wenzel* state, liquid fully penetrates the texture and the apparent contact angle θ^* follows

$$\cos\theta^* = r\,\cos\theta_0, \tag{5}$$

where θ_0 is the intrinsic contact angle on the smooth material and r is the roughness factor (ratio of true to projected area). Roughness amplifies intrinsic wetting: hydrophilic materials become more hydrophilic and hydrophobic materials more hydrophobic.

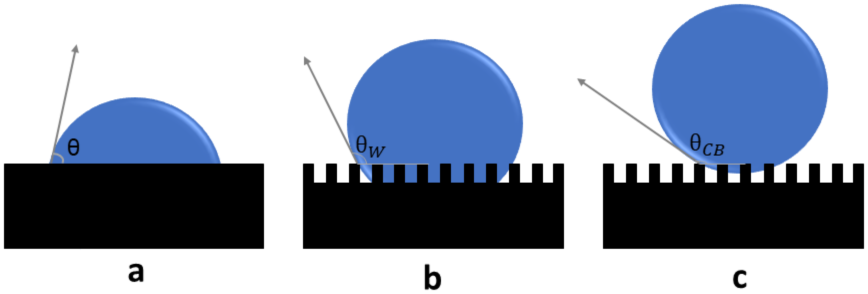

Figure 2.2: Cassie-Baxter and Wenzel models of drops on rough surfaces.

In the *Cassie–Baxter* state, liquid rests on asperity tops while air remains trapped beneath, yielding a composite interface:

$$\cos\theta^* = \phi_s\,\cos\theta_0 - (1-\phi_s)\,, \tag{6}$$

where ϕ_s is the solid fraction in contact with the liquid. For $\phi_s \ll 1$, very high apparent contact angles and very low hysteresis are possible, which minimize real contact area and can lower ice adhesion if freezing occurs.

Wetting transitions from Cassie to Wenzel may be induced by impact pressure, prolonged exposure to liquid water, condensation and frosting, or by the advancing ice front during solidification. Once liquid or ice penetrates the texture, mechanical interlocking and contact-line pinning increase interfacial toughness and adhesion. Accordingly, robust icephobic designs combine low surface energy with textures that resist impalement and preserve a composite interface during both liquid contact and freezing (Lafuma & Quéré, 2003). Hierarchical micro and nano features are often used to stabilize non-wetting states and to limit frost bridging across the texture, thereby reducing the likelihood of strong interlocks forming during accretion.

2.3 Surface Topography, Wettability, and Ice Adhesion

Surface topography and surface chemistry jointly determine wetting state, contact-line mobility, and the extent of mechanical interlocking, and therefore play a central role in controlling ice adhesion. Roughness can either suppress or enhance adhesion depending on length scale, morphology, and whether the texture remains in a Cassie-like or Wenzel-like state during icing (Dhyani et al., 2022; He et al., 2021; Kreder et al., 2016a). This section reviews how single-scale and hierarchical textures affect wetting and ice adhesion, how roughness statistics relate to performance, and how these factors connect mechanically to the work of adhesion and interfacial toughness.

2.3.1 Single-Scale Micro- and Nano-Roughness

Single-scale roughness at the micro- or nano-scale strongly affects both wetting and ice adhesion. Early icephobic work focused on micro-rough or nanoparticle-based coatings that rendered inherently hydrophobic substrates superhydrophobic, achieving water contact angles above 150° with low hysteresis and thereby reducing the real solid–liquid contact area (Kreder et al., 2016a; Menini & Farzaneh, 2011; Parent & Ilinca, 2011). For instance, Menini and Farzaneh showed that rough polymer and composite coatings on aluminum could reduce shear ice-adhesion strength by factors of two to four compared to bare metal, provided that low hysteresis and a Cassie-like wetting state were maintained (Menini & Farzaneh, 2011).

However, a high static water contact angle alone is insufficient for robust icephobicity. Kulinich and Farzaneh demonstrated that rough fluoropolymer coatings with high static contact angles but large contact-angle hysteresis did not perform well: only coatings that were both superhydrophobic and low-hysteresis showed substantial reductions in τ_{ice} (Kulinich & Farzaneh, 2009). These results underscore that contact-line pinning, captured by hysteresis or receding angle, is as important as the apparent contact angle itself (He et al., 2021; Kulinich & Farzaneh, 2009; Menini & Farzaneh, 2011).

Single-scale microtextures (e.g., micropillars, microgrooves) may still permit liquid ingress if the pitch or geometry allows, enabling anchoring of liquid or ice within the texture. Purely nanostructured films such as dense nanoparticle layers can be overwhelmed by condensation or frost, as small pores readily fill by capillary action, converting a Cassie state to Wenzel and greatly increasing adhesion (Dhyani et al., 2022; Nosonovsky & Hejazi, 2012). Systematic studies that vary feature size and spacing indicate an optimal texture that is sparse enough to minimize solid–liquid contact (favoring Cassie) yet not so sparse that liquid sags and penetrates under hydrostatic or impact pressure (Nguyen, Park, & Lim, 2018). If roughness is too coarse (feature size comparable to ice thickness), ice can key into the asperities; if too fine and fully frosted, the texture effectively behaves as a rough, fully wetted solid. Roughness alone is therefore not a panacea; it must be combined with low surface energy and careful control of pinning to avoid unintended Wenzel states during freezing (He et al., 2021; Kulinich & Farzaneh, 2009).

2.3.2 Hierarchical (Dual-Scale) Structures

Natural non-wetting surfaces such as lotus leaves and certain insect wings often exhibit hierarchical structures: micro-scale features decorated with nano-scale textures. Such dual-scale roughness stabilizes non-wetting states and improves robustness against external perturbations. In icephobic design, hierarchical architectures reduce contact area through the micro-scale features while the nano-scale texture helps resist liquid impalement and limits pinning of both water and ice (Dhyani et al., 2022; Kreder et al., 2016a).

Dual- or triple-scale coatings can yield water contact angles above 160° with very low sliding angles, delaying icing under condensing/frosting conditions and reducing adhesion when ice does form (Nguyen et al., 2018; Zhang, Yu, Wu, & Wu, 2012). Nguyen *et al.* showed that superhydrophobic surfaces with optimized dual-scale roughness significantly delayed frost formation and reduced ice adhesion compared with single-scale textures (Nguyen et al., 2018). Zhang *et al.* similarly reported hierarchical nanostructures on aluminum that promoted controlled condensation and delayed icing, highlighting the advantage of multi-scale textures under realistic atmospheric conditions (Zhang et al., 2012). In addition, hierarchical designs can resist frost bridging by limiting the formation of continuous ice layers and interrupting frost-front propagation across the surface (He et al., 2021; Nosonovsky & Hejazi, 2012).

2.3.3 Roughness Metrics, Surface Statistics, and Ice Adhesion

Quantitative roughness metrics help correlate structure with performance. Common 2D parameters include the mean arithmetic roughness R_a and root-mean-square roughness R_q, while 3D profilometry yields areal measures such as S_a, S_q, and the developed interfacial area ratio S_{dr} (percentage increase of true area relative to projected area). Fractal dimension D_f describes multi-scale roughness, ranging from $D_f = 2$ for ideally smooth surfaces to values approaching 3 for extremely rough, multi-scale topographies (He et al., 2021; Nosonovsky & Hejazi, 2012). Increased S_{dr} or true contact area often correlates with higher adhesion if the surface is fully wetted, whereas certain geometries (e.g., rounded or re-entrant asperities) may sustain a composite interface and lower adhesion even at relatively high S_{dr} (He et al., 2021).

Figure 2.3 compiles literature data for smooth, textured, slippery, and subsurface-textured surfaces, grouped by test method and temperature, following the classification in He *et al.* (He et al., 2021). The substantial scatter in τ_{ice} at a given temperature and surface class highlights the combined influence of wetting state, roughness, mechanical compliance, and loading mode. Nevertheless, clear trends emerge: smooth hydrophobic surfaces typically yield moderate adhesion reduction relative to bare metals, topographically textured superhydrophobic surfaces reduce adhesion further but remain strength-limited in many cases, and slippery or subsurface-textured designs can reach much lower apparent adhesion strengths by promoting interfacial crack initiation and propagation (Golovin et al., 2016; He et al., 2021; Wong et al., 2011).

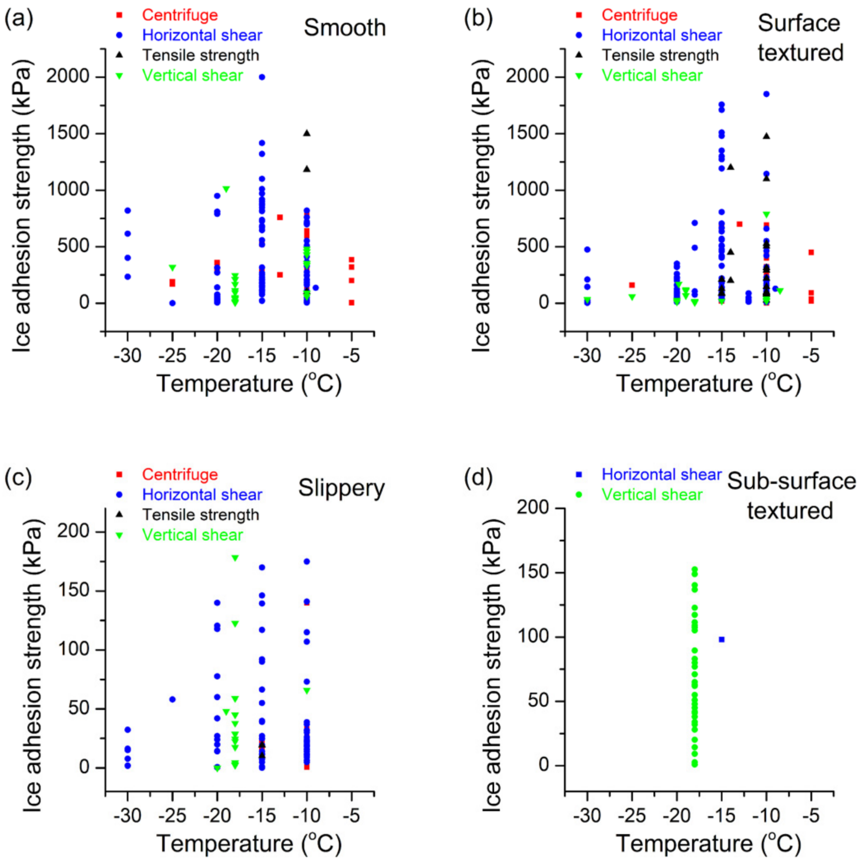

Figure 2.3: Ice adhesion strength versus temperature for four surface categories: (a) smooth, (b) textured, (c) slippery, and (d) subsurface textured. Data points are compiled from the literature and grouped by test method (He et al., 2021).

The relation between roughness and interfacial shear is non-monotonic: increasing developed area S_{dr} can first reduce and then increase τ_{ice} depending on whether the texture remains in a Cassie-like state or becomes impaled and strongly pinned. Figure 2.4 illustrates this trend for multi-scale laser-treated aluminum samples under rime, mixed, and glaze icing conditions from Milles *et al.* (Milles et al., 2021). At low S_{dr}, added roughness decreases adhesion by reducing real contact and enhancing droplet mobility; at higher S_{dr}, however, capillary impalement and mechanical interlocking dominate, and τ_{ice} increases again. These results emphasize the need to design not only the magnitude but also the morphology and distribution of roughness features.

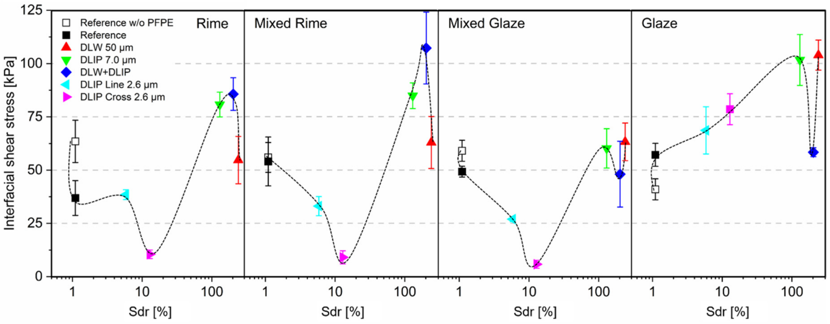

Figure 2.4: Interfacial shear stress of various laser-treated samples as a logarithmic function of the developed interfacial area ratio (S_{dr}) for four icing conditions. The non-linear trend highlights the complex relationship between surface texture and ice adhesion (Milles et al., 2021).

2.3.4 Fractal Roughness and Contact-Line Pinning

Fractal-like rough surfaces present pinning sites across a broad range of scales for advancing and receding contact lines or advancing ice fronts, increasing hysteresis and interfacial toughness. Nosonovsky and Hejazi showed that superhydrophobicity does not guarantee icephobicity: surfaces that bead water extremely well can still anchor solid ice once freezing proceeds into the texture, particularly when frost bridges form between asperities (Nosonovsky & Hejazi, 2012). In their analysis, fractal descriptors and multi-scale roughness statistics correlated better with ice adhesion than a single roughness parameter such as R_a, reflecting the importance of pinning sites across scales.

Conversely, deliberate patterning (e.g., aligned microgrooves or periodic ridges) can guide crack paths and reduce effective interfacial toughness by promoting controlled debonding rather than random fracture (He et al., 2021). Modeling and recent experiments suggest that certain patterns encourage crack initiation or interfacial cavitation at lower driving forces, thereby lowering adhesion (Golovin, Dhyani, Thouless, & Tuteja, 2019; Nistal, Sierra-Martín, & Fernández-Barbero, 2024). In practice, controlled hierarchical structures are preferred over uncontrolled, random fractality to reduce unpredictable pinning and facilitate repeatable ice-shedding behavior.

2.3.5 Mechanistic Links Between Roughness, Wettability, and Ice Adhesion

The Young–Dupré relation links the thermodynamic work of adhesion W_a between a liquid and a solid to the liquid–vapor surface tension γ_{LV} and the equilibrium contact angle θ:

$$W_a = \gamma_{LV} \, (1 + \cos\theta) \, . \tag{7}$$

In practice, using the receding angle θ_{rec} gives a better correlation with measured ice adhesion because it incorporates contact-line pinning and hysteresis (He et al., 2021; Kulinich & Farzaneh, 2009; Menini & Farzaneh, 2011). Low θ_{rec} (strong pinning) typically corresponds to higher τ_{ice}, whereas high θ_{rec} and low hysteresis correlate with lower τ_{ice} across a range of textures and chemistries (Kulinich & Farzaneh, 2009; Menini & Farzaneh, 2011; Nistal et al., 2024).

Roughness that sustains a Cassie state reduces W_a and often τ_{ice} by minimizing true contact area, but complex asperities and deep pores can increase pinning and negate these benefits once liquid or ice penetrates the texture. Mechanical interlocking within deep grooves or undercut pores further increases adhesion. Minimizing true contact area, avoiding interlocks, and limiting pinning via composite interfaces (air pockets or infused lubricants) are therefore key strategies. Representative wetting and ice-adhesion performance for common surface types are summarized in Table 2.1; as discussed in Sections 2.4 and 2.6, achieving ultra-low τ_{ice} (a few kPa or less) often requires moving beyond purely hydrophobic textures toward compliant or liquid-mediated interfaces such as soft elastomeric coatings and SLIPS (Dhyani et al., 2022; Golovin et al., 2019, 2016; Wong et al., 2011).

2.4 Ice-Adhesion Measurement Techniques

Accurately quantifying the adhesion strength of ice to a substrate is non-trivial. Common adhesion tests differ in loading mode, sample geometry, and environmental history, and these differences can lead to widely scattered values even for nominally similar coatings (Brassard et al., 2017; He et al., 2021; Nistal et al., 2024). Most techniques freeze a defined ice volume or layer on a test substrate and then apply a controlled load until detachment, reporting a nominal shear strength

$$\tau_{\text{ice}} = \frac{F}{A}, \tag{8}$$

where F is the peak load at failure and A is the apparent contact area. Variations in loading mode (shear vs. tension), ice morphology (rime vs. glaze), strain rate, and the presence of residual stresses or defects can all influence the measured τ_{ice} (Brassard et al., 2017; Nistal et al., 2024; Susoff et al., 2013). It is worth noting that significant uncertainty remains, as no predictive model yet exists for ice adhesion, and discrepancies persist between molecular-dynamics simulations and laboratory measurements (Chang et al., 2024).

Figure 2.5 schematizes four widely used approaches: horizontal shear (push), vertical shear, tensile pull-off, and centrifugal methods. This section outlines their main features, typical assumptions, and common artifacts, emphasizing how these factors affect interpretation and comparison across studies.

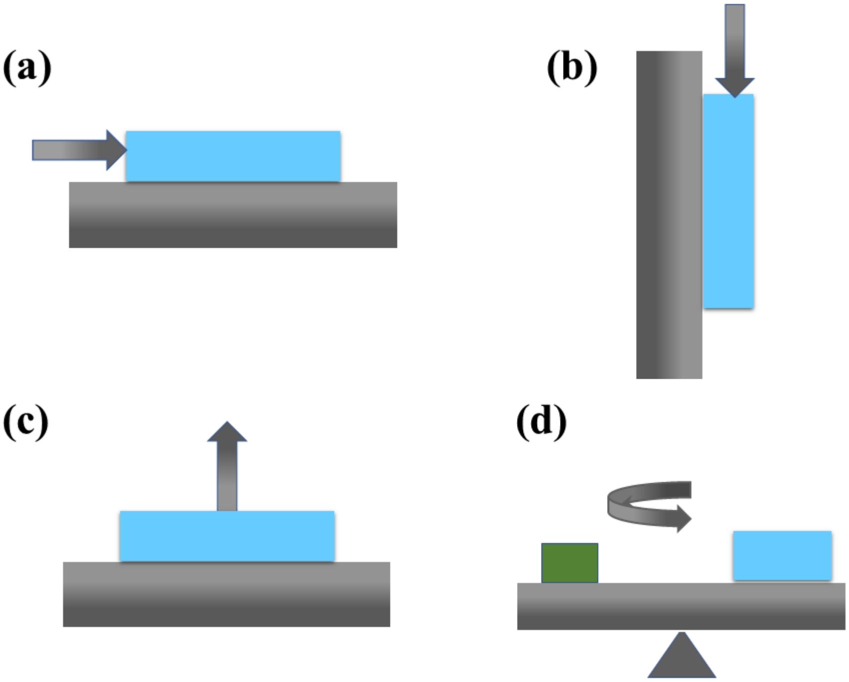

Figure 2.5: Schematic of common ice adhesion testing methods: (a) horizontal shear (push test), (b) vertical shear tensile test, (c) tensile pull-off, and (d) centrifuge.

2.4.1 Shear (Push-Off) Tests

In push-off tests, a cylindrical or prismatic stub of ice is grown or cast on the test surface (often inside a mold) and then loaded laterally until it shears off. The peak force divided by the nominal contact area gives τ_{ice}. Several studies use ice cylinders of 20–30 mm diameter with the load applied close to the interface to reduce bending (Brassard et al., 2017; Menini & Farzaneh, 2011; Susoff et al., 2013). Careful control of icing conditions (water quality, temperature history, and cooling rate) is required to obtain reproducible glaze ice at the interface; otherwise, cohesive failure within a porous rime layer may dominate.

Artifacts include non-uniform stress distributions (especially for tall or slender cylinders that can bend or topple), friction against the mold walls, and mixed-mode loading if the push head is misaligned. To ensure that the ice–substrate interface is the weakest link, many protocols specify a fixed test temperature (e.g., $-10\,^{\circ}\text{C}$), a dwell time after freezing, and a thickness range for the ice layer (Brassard et al., 2017; Nistal et al., 2024). When these conditions are not standardized, direct comparison of τ_{ice} values between different laboratories becomes difficult.

2.4.2 Tensile (Pull-Off) Tests

Tensile or pull-off tests apply a normal load to the ice via a stud or dolly bonded to the ice surface. The assembly is pulled perpendicular to the substrate until failure, ideally probing mode I separation. Such tests are often adapted from paint-adhesion standards (e.g., ASTM D4541), which prescribe dolly geometry and loading rate. Alignment is critical: any tilt or misalignment introduces a shear component that can substantially reduce the apparent tensile strength (Brassard et al., 2017; He et al., 2021).

Although pure tensile loading is less representative of many service conditions (where shear or mixed-mode loading dominates), pull-off tests are valuable for identifying failure modes (adhesive vs. cohesive) and for quantifying the intrinsic normal strength of the interface. They are also convenient when space constraints make lateral loading difficult. However, the need for an adhesive between ice and dolly adds another interface that can sometimes fail first, complicating data interpretation (Nistal et al., 2024).

2.4.3 Centrifugal Tests

Centrifugal adhesion tests mount one or more coated samples with ice layers on a rotating arm or drum and progressively increase the rotational speed until the ice detaches. The critical speed or acceleration at detachment is used to back-calculate an equivalent shear stress at the interface. This approach is attractive for rapid screening because many samples can be tested simultaneously under identical thermal conditions (Brassard et al., 2017; Susoff et al., 2013).

Artifacts arise from aerodynamic drag on the ice, non-uniform ice thickness or density along the sample, and uncertainties in the effective detachment area. Furthermore, centrifugal loading is inherently mixed mode (normal and shear components) and spatially varying. Consequently, care must be taken when comparing centrifugal τ_{ice} values with those from quasi-static push or pull-off tests (He et al., 2021; Nistal et al., 2024). Nevertheless, centrifugal methods are widely used in industrial screening campaigns due to their throughput and relative simplicity.

2.4.4 Other Methods and Normalization Strategies

Additional methods include impact tests (pendulum or drop-weight), torsional loading of ice cylinders, and three-point bending of ice beams bonded to surfaces. These geometries probe different combinations of mode I and mode II fracture and are sometimes used to extract an apparent interfacial toughness rather than just a strength (He et al., 2021). Because results are strongly dependent on loading mode, rate, and ice morphology, it is increasingly common to report an *adhesion reduction factor* (ARF), defined as

$$\text{ARF} = \frac{\tau_{\text{ice, ref}}}{\tau_{\text{ice, surface}}}, \tag{9}$$

where $\tau_{\text{ice, ref}}$ is the adhesion on a reference substrate such as polished aluminum under identical test conditions (Brassard et al., 2017; Nistal et al., 2024). ARF helps to compare coatings tested in different rigs or laboratories, provided the reference surface and protocol are clearly documented.

Across all methods, standardized procedures and detailed reporting of experimental conditions (ice type, temperature, humidity, cooling rate, dwell time, surface roughness, sample geometry, and loading rate) are essential to enable meaningful comparison and meta-analysis of icephobic performance (Brassard et al., 2017; He et al., 2021; Nistal et al., 2024). Ongoing efforts toward consensus standards for ice-adhesion testing should improve reproducibility and help bridge the gap between laboratory measurements and field-relevant performance.

2.5 Fabrication Methods for Icephobic Surfaces

Creating an icephobic surface typically involves sculpting surface texture (top-down), depositing or assembling functional coatings (bottom-up), or combining both approaches in a hierarchical manner. In most practical designs, top-down methods define the geometry and characteristic length scales that control wetting and mechanical interlocking, while bottom-up methods tune surface chemistry, mechanical compliance, and sometimes subsurface architecture (Dhyani et al., 2022; He et al., 2021; Kreder et al., 2016a). The choice of fabrication route is dictated by the target substrate (metal, polymer, composite), component size and shape, allowable surface roughness (particularly critical in aerodynamics), and cost or throughput constraints. This section surveys widely used fabrication strategies, emphasizing how each method links to the icephobic mechanisms discussed in Sections 2.2–2.3 and to durability issues elaborated in Section 2.8.

2.5.1 Top-Down Techniques (Micro/Nano-Texturing)

Top-down methods directly pattern the substrate to create micro- or nano-scale roughness that supports Cassie–Baxter wetting, promotes droplet mobility, and, in some cases, facilitates interfacial crack initiation during de-icing. When combined with a low-surface-energy overlayer, such textures can reduce the real ice–substrate contact area and suppress mechanical interlocking (He et al., 2021; Nosonovsky & Hejazi, 2012).

Laser ablation and texturing: Laser processing can generate microgrooves, microcones, and nano-ripples (laser-induced periodic surface structures, LIPSS) on metals, polymers, and ceramics by tuning wavelength, pulse duration, fluence, and scan speed. Picosecond and femtosecond lasers are particularly attractive because they enable ablative texturing with minimal heat-affected zones and can simultaneously produce multi-scale (micro+nano) roughness in a single step (Kreder et al., 2016a). After hydrophobization with fluorosilanes or fluoropolymer overcoats, such surfaces often show static water contact angles exceeding 160° and low sliding angles, which translates into reduced ice adhesion and delayed frost formation (He et al., 2021). For example, Milles *et al.* created multi-scale laser-textured aluminum surfaces for aeronautic applications and reported ice-adhesion strengths in the range of a few tens of kPa, along with good stability over repeated icing/de-icing cycles (Milles et al., 2021). Similar approaches have been explored on titanium and stainless steel, highlighting the versatility of laser texturing for high-value metallic components. Advantages include maskless processing, digital control of patterns, and applicability to curved or complex geometries, whereas limitations are primarily related to equipment cost and throughput for very large areas.

Lithography and etching: Photolithography or nanoimprint lithography combined with reactive-ion etching, wet chemical etching, or deep-etch processes can produce highly controlled arrays of micro- and nano-features (e.g., posts, cones, overhangs) on silicon, glass, or metal substrates. These methods originated in microelectronics and MEMS fabrication and allow precise tuning of feature size, spacing, and re-entrant geometry—parameters known to govern Cassie-state stability and impact-induced impalement (Dhyani et al., 2022; Kreder et al., 2016a). When subsequently hydrophobized, such patterned substrates have been used as model systems to systematically probe the influence of roughness on condensation frosting, droplet impact, and ice adhesion (Nguyen et al., 2018; Zhang et al., 2012). However, their use in large-scale infrastructure is currently limited by process cost, planar geometry constraints, and the need for cleanroom infrastructure.

Abrasive/mechanical roughening: Sandblasting, shot peening, grit blasting, and micromilling introduce stochastic roughness over areas ranging from cm^2 to m^2. These techniques are widely available in industry and can be applied to large, curved components such as turbine blades or pylons. When followed by hydrophobization (e.g., spraying or dipping in fluorinated or silicone-based coatings), they could reduce ice adhesion relative to smooth substrates, particularly when the resulting morphology supports a partial Cassie state (Menini & Farzaneh, 2011; Susoff et al., 2013).

Anodizing and porous oxides: Anodized aluminum oxide (AAO) and related porous-oxide layers (e.g., on titanium) provide ordered or semi-ordered nanoporous networks with pore diameters typically spanning 20–200 nm and thicknesses up to tens of micrometers. These porous layers can be hydrophobized to obtain superhydrophobicity, or, alternatively, infused with a lubricating liquid to create SLIPS interfaces (see Section 2.6) (He et al., 2021; Wong et al., 2011). The anodic layer is strongly bonded to the underlying substrate, which enhances mechanical robustness compared with loosely attached nanoparticle paints. At the same time, brittleness and susceptibility to cracking under bending or impact, as well as the need for additional surface-energy modification, are important considerations for highly loaded structural components.

Architected and subsurface-textured substrates: Beyond simple surface roughening, there is growing interest in subsurface texturing and architected materials, in which cavities, channels, or compliant interlayers are incorporated beneath the outer surface to manipulate stress distributions during ice detachment (He et al., 2021). For instance, aligned grooves or subsurface voids can act as crack initiators and guide interfacial fractures, effectively reducing the apparent toughness of the ice–substrate interface without compromising the macro-scale integrity of the component. Such concepts are still largely at the laboratory stage but illustrate how top-down patterning can be used not only to control wetting but also to engineer fracture mechanics.

2.5.2 Bottom-Up Techniques (Coatings and Deposition)

Bottom-up approaches build icephobic functionality by depositing thin films, multilayers, or composite coatings onto a substrate. These methods are especially powerful for tailoring surface chemistry (e.g., low surface energy, hydrogen-bonding character), mechanical compliance, and, in some cases, the presence of mobile phases (lubricants, liquid-like polymer segments). In practice, many commercial or field-tested icephobic treatments are based on bottom-up coatings applied to pre-existing components (C. Laforte et al., 2019; Menini & Farzaneh, 2011; Nistal et al., 2024).

CVD and molecular scale coatings: Vapor-phase deposition of organosilanes, fluorocarbons, or organosilazanes via chemical vapor deposition (CVD) or initiated CVD (iCVD) yields conformal, nanometer-scale films with low surface energy and good chemical uniformity. Such monolayers or ultra-thin polymer coatings are particularly attractive for applications where macroscopic roughness and optical clarity must be preserved (e.g., radomes, sensor windows), as they add minimal thickness and do not significantly alter surface topography. Their icephobic performance is typically modest (adhesion reduction factors of $\sim$ 2–3 relative to bare aluminum) because they do not drastically change roughness or compliance (Kreder et al., 2016a; Menini & Farzaneh, 2011).

Nonetheless, they can serve as primer layers that improve the adhesion and durability of thicker icephobic topcoats.

Sol–gel and dip coating: Sol–gel processes allow the formation of silica or hybrid organic–inorganic networks containing embedded hydrophobic moieties and nano- or micro-particles. By adjusting precursor chemistry, condensation conditions, and withdrawal speeds, one can tune film thickness, porosity, and roughness, thereby transitioning from smooth hydrophobic to superhydrophobic states (Dhyani et al., 2022; Menini & Farzaneh, 2011). Dip coating or spin coating of sol–gel formulations onto metals, polymers, or glass has been widely explored for icephobic and anti-fog applications. Incorporating elastomeric binders or flexible organic segments into the sol–gel matrix can mitigate cracking and improve resistance to thermal cycling. However, purely inorganic or brittle networks are susceptible to chipping and microcracking under impact or bending, which may rapidly degrade icephobic performance (Nistal et al., 2024).

Spray coatings (nanocomposites): Spray deposition of polymer–particle suspensions is one of the most scalable routes to superhydrophobic and icephobic surfaces. Typical formulations combine a binder (e.g., silicone, polyurethane, acrylic) with low-surface-energy particles (e.g., fluorinated silica, PTFE, polypropylene, or polyethylene powders) dispersed in a volatile solvent (Menini & Farzaneh, 2011; Susoff et al., 2013). Upon evaporation, a micro/nano-structured coating forms, often displaying water contact angles above 150° and contact angle hysteresis below 10°, while reducing τ_{ice} by factors of 2–3 relative to uncoated aluminum (Menini & Farzaneh, 2011). The binder composition is critical: harder binders enhance abrasion resistance but may increase contact-line pinning, whereas softer binders improve compliance and ice release but can be more vulnerable to erosion. Recent aeronautical studies have demonstrated superhydrophobic spray coatings that maintain low ice adhesion over multiple icing cycles and rain-erosion tests, although some loss of performance with time is unavoidable (Nistal et al., 2024; Piscitelli, Fanciullo, Sarcinella, Costantini, & Frigione, 2025). Spray processes are compatible with large blades, towers, and nacelles, making them attractive for wind and power applications.

Thermal-spray coatings: Thermal spraying (e.g., atmospheric plasma spraying, suspension plasma spraying, or HVOF) of inorganic powders such as TiO_2 or Al-based quasicrystalline alloys produces thick, relatively rough ceramic or metallic-ceramic coatings whose surface topography and porosity can be tuned by process parameters and post-treatments. Plasma-sprayed TiO_2 coatings have been engineered to exhibit hydrophobic or superhydrophobic wetting and reduced ice adhesion by controlling micro-/nano-scale hierarchical morphology (Sharifi, Dolatabadi, Pugh, & Moreau, 2019; Sharifi, Ettouil, Moreau, Dolatabadi, & Pugh, 2017). Quasicrystalline coatings deposited by HVOF and related processes similarly show reduced ice accretion and durable low interfacial toughness with ice (Mohseni et al., 2021; Mora, García, Muelas, & Agüero, 2020). On engineering structures relevant to power transmission and aeronautics, such thermally sprayed coatings offer mechanically robust, scalable icephobic surfaces and can also act as porous scaffolds for lubricant-infused slippery surfaces (SLIPS) or other overcoatings (Koivuluoto, Hartikainen, & Niemelä-Anttonen, 2020).

Electro/electroless deposition and metal–polymer composites: Electroplating or electroless deposition processes can embed low-surface-energy particles (e.g., PTFE) or soft polymer phases within a metallic matrix such as nickel, copper, or zinc. The resulting metal–polymer composite coatings are mechanically robust, electrically conductive, and often exhibit micro- or nano-scale roughness that can be further tuned via processing parameters. These characteristics make them relevant for power infrastructure (where electrical properties matter) and for structural components requiring wear resistance (He et al., 2021; Nistal et al., 2024). Post-treatment with hydrophobizing agents can further lower surface energy and promote Cassie-like states.

Bioinspired polymers, gels, and tethered liquid-like layers: Inspired by natural systems such as pitcher plants and cartilage, several groups have developed soft polymeric and gel-based coatings that achieve low ice adhesion via interfacial compliance and/or the presence of mobile, liquid-like surface segments. Examples include low-crosslink-density silicones, polyurethanes, and hydrogels that that possess high compliance or lubricity (Golovin et al., 2016). Tethered liquid-like polymer layers—in which short, mobile chains are covalently anchored to a solid backbone—have also been proposed as robust, self-healing icephobic interfaces that combine low interfacial toughness with chemical stability (Golovin et al., 2019). These systems often achieve shear ice-adhesion strengths below $10–20\,\mathrm{kPa}$ and can exhibit size-independent debonding behavior (Section 2.6), but their long-term resistance to abrasion, contamination, and UV exposure remains an active research topic (Nistal et al., 2024).

Lubricant-infused porous surfaces (SLIPS): Although discussed in more detail in Section 2.6, it is worth noting here that SLIPS are fundamentally a two-step bottom-up fabrication: first, a porous or rough scaffold (produced by anodizing, sol–gel, etching, or spraying) is created; second, an immiscible lubricant is infused into this scaffold (Kreder et al., 2016a; Wong et al., 2011). The infused liquid forms a smooth, mobile interface that dramatically reduces contact-angle hysteresis and τ_{ice}. Careful matching of lubricant viscosity, surface tension, and chemical affinity with the solid matrix is essential for long-term lubricant retention under shear and thermal cycling.

2.5.3 Durability and Scale-Up

Regardless of fabrication method, a critical challenge is ensuring that the coating or texture can endure the mechanical, thermal, and chemical conditions of its intended use over many icing/deicing cycles. As emphasized in recent durability reviews (Nistal et al., 2024), the micro- and nanoscale features that impart strong icephobicity are often the first to be damaged by abrasion, erosion, or contamination.

Mechanical wear from wind-blown sand, rain, hail, or debris can erode micro/nano-textures or wear away coatings. Many superhydrophobic surfaces lose their properties after relatively mild abrasion, shifting from a Cassie-like to a Wenzel-like state and thereby increasing τ_{ice} (Nistal et al., 2024; Susoff et al., 2013). Strategies to improve wear resistance include using harder materials (ceramic or metallic textures) beneath a thin hydrophobic layer, embedding wear-resistant nanoparticles within elastic binders (nanocomposites), or designing coatings with self-healing capabilities so that scratches can be refilled with hydrophobic material (Golovin et al., 2016; Nistal et al., 2024). A durable icephobic surface developed by Golovin *et al.* used a bulk elastomeric coating with uniform low crosslink density through the thickness, which maintained low ice adhesion even after significant abrasion and cutting damage (Golovin et al., 2016).

Environmental degradation is another important factor. Organic coatings (polymers, monolayers) can degrade under UV light, ozone, humidity, and temperature cycling, leading to embrittlement or loss of hydrophobic functional groups. Fluoropolymers and silicones are generally more

UV-stable than many other polymers, but prolonged exposure still reduces performance (Brassard et al., 2017; Nistal et al., 2024). Consequently, accelerated weathering tests (UV exposure, salt spray, freeze–thaw cycling) are increasingly incorporated into icephobic coating evaluations to assess long-term stability (C. Laforte et al., 2019). Coatings may require UV stabilizers, antioxidant additives, or periodic re-application in harsh outdoor environments.

The adhesion of the coating to the substrate is equally critical. Many nanoparticle-based superhydrophobic paints exhibit poor adhesion and can delaminate under thermal cycling or when ice detaches, effectively "peeling" the coating off with the ice (C. Laforte et al., 2019; Susoff et al., 2013). Surface priming (e.g., grit blasting, chemical etching) and the use of coupling agents (e.g., silanes) or high-adhesion binders (epoxy, polyurethane) can greatly improve coating–substrate bonding. Some recent systems use a layered architecture: a strongly adherent, mechanically robust primer that bonds to the substrate, topped by a thinner, more delicate icephobic layer that can be renewed without removing the primer (Nistal et al., 2024).

Finally, scale-up considerations strongly influence which fabrication methods are viable for specific applications. Techniques such as spraying, roll-to-roll coating, and tape-like films are being developed to apply icephobic treatments to large structural surfaces (e.g., wind-turbine blades, power cables, aircraft wings) in a cost-effective manner (J.-L. Laforte et al., 1998; Parent & Ilinca, 2011; Piscitelli et al., 2025). For example, one concept is an icephobic "tape" for leading edges that can be applied in the factory or in the field and replaced when worn, shifting complex fabrication steps to a controlled industrial environment. In practice, current commercial offerings are often sacrificial coatings or paints that can be re-applied as part of routine maintenance. Even so, by significantly reducing ice accretion between maintenance intervals, such treatments can yield substantial operational and safety benefits. Developing truly long-lived icephobic surfaces—capable of surviving years of service without reapplication—remains a central goal that drives ongoing work in materials selection, coating architecture, and process optimization.

2.6 Low-Interfacial-Toughness and Slippery Approaches

Reducing τ_{ice} is necessary but not always sufficient to ensure easy removal of large ice accretions. On many conventional superhydrophobic or smooth hydrophobic surfaces, adhesion is essentially *strength-limited*: the maximum shear or tensile stress the interface can sustain scales with area, so the total force required to shed a large patch of ice grows approximately as $F = \tau_{\text{ice}} A$ (He et al., 2021). In contrast, for *toughness-limited* interfaces, debonding is governed by interfacial crack propagation rather than local strength, and the force required to remove large ice patches can become nearly size-independent once a crack is nucleated (Golovin et al., 2019; Wong et al., 2011). Low-interfacial-toughness (LIT) materials and architectures are therefore an important complement to low-τ_{ice} designs, as they minimize the energy release rate required to propagate an interfacial crack and can enable large-scale shedding under modest loads (Dhyani et al., 2022; Golovin et al., 2019).

2.6.1 Toughness-Limited vs. Strength-Limited Behavior

Traditional superhydrophobic surfaces typically remain strength-limited: local failure may initiate at relatively low interfacial stress, but large patches still require large total forces because crack propagation is impeded by strong pinning and mechanical interlocking within the texture (He et al., 2021; Nosonovsky & Hejazi, 2012). In such cases, reducing τ_{ice} through lower surface energy or reduced real contact area is beneficial, but the detachment force still grows with ice-covered area.

LIT designs seek to change the failure mode. By tailoring the compliance of the substrate, introducing weak or lubricated interfacial layers, or engineering stress concentrators that promote crack initiation, LIT surfaces encourage controlled interfacial fracture at low driving force (Golovin et al., 2019). Golovin *et al.* showed that for a broad class of soft and slippery coatings, ice detachment could be described in terms of an "ice-reduction potential" ℓ^* that captures the balance between interfacial toughness and the characteristic stress distribution; coatings with low interfacial toughness exhibited a saturation in the force required to shed larger ice patches, indicative of a toughness-limited regime (Golovin et al., 2019). This distinction is crucial for real components (e.g., wings, blades, power lines) where ice-covered areas can be large.

2.6.2 Soft Polymeric Coatings and Gels

Soft elastomers (e.g., PDMS with low crosslink density) and related polymeric gels are prototypical LIT materials. Their low elastic modulus reduces interfacial shear transfer and promotes interfacial cavitation or decohesion at relatively low loads, yielding τ_{ice} below 10 kPa in shear tests and even lower forces in peel configurations (Golovin et al., 2019, 2016). In addition, their compliance allows local stress concentrations to relax, favoring interfacial crack propagation rather than cohesive fracture of the ice.

Systematic studies of crosslink density have revealed clear trends. Golovin *et al.* demonstrated that decreasing the crosslink density ρ_{CL} of PDMS coatings (and related elastomers) leads to a pronounced reduction in τ_{ice}, especially when combined with interfacial slippage at the ice–coating interface (Golovin et al., 2016). Figure 2.6 quantifies how ρ_{CL} and interfacial slippage modulate adhesion and the ice-reducing potential ℓ^*: in the absence of slippage, τ_{ice} scales strongly with ρ_{CL}, whereas in the presence of slippage, τ_{ice} becomes much less sensitive to modulus and can reach very low values across a broad range of formulations.

Trade-offs include wear resistance, contamination, and environmental stability. Very soft polymers are more prone to erosion, scratching, and uptake of oils or particulates, all of which can increase pinning and degrade performance over time (Nistal et al., 2024). Formulation strategies include using block copolymers or nanocomposites that combine a compliant matrix with reinforcing domains, or incorporating self-healing chemistries that can repair surface damage while preserving low interfacial toughness (Golovin et al., 2016; Nistal et al., 2024). Nonetheless, soft coatings have demonstrated some of the lowest repeatable τ_{ice} values reported, and they serve as a key benchmark for LIT behavior.

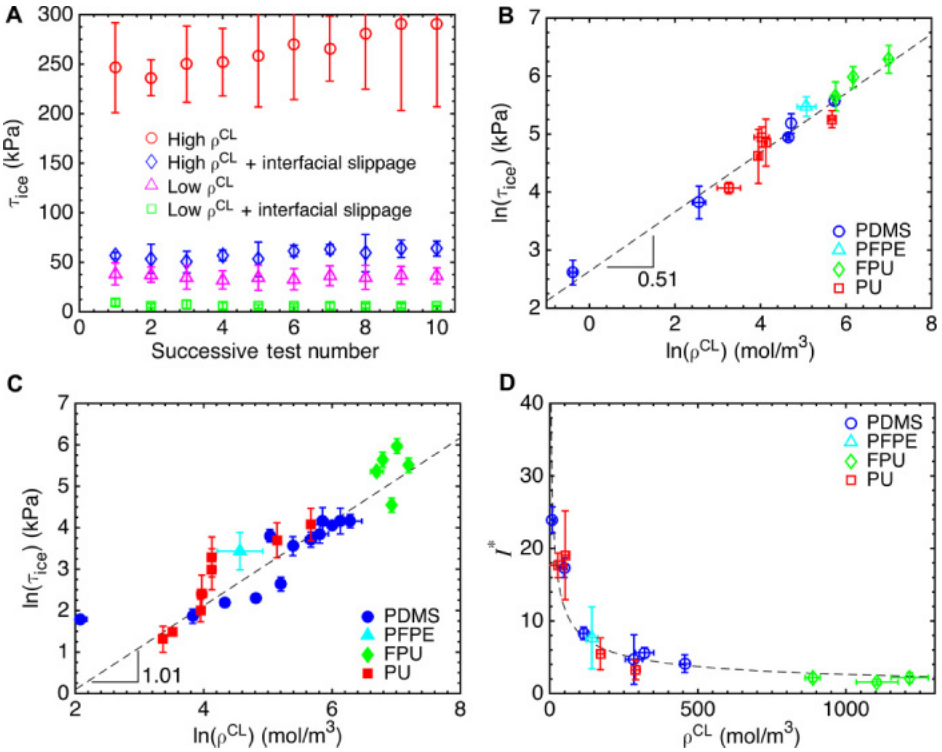

Figure 2.6: Mechanisms responsible for low ice adhesion on elastomeric coatings. (a) Ice adhesion strength for PDMS coatings with varying crosslink density (ρ_{CL}) and with or without interfacial slippage. (b,c) Relationships between τ_{ice} and ρ_{CL} without (b) and with (c) interfacial slippage, revealing different scaling laws. (d) Resulting ice-reducing potential (ℓ^*) as a function of ρ_{CL} (Golovin et al., 2016).

2.6.3 Slippery Liquid-Infused Porous Surfaces (SLIPS)

Slippery liquid-infused porous surfaces (SLIPS) use a textured or porous scaffold infused with an immiscible lubricant to present a smooth *liquid* interface to water and ice. The infused liquid fills the roughness, displacing air and creating a defect-free, mobile interface that exhibits extremely low contact-angle hysteresis and very low τ_{ice} (often a few kPa or less) (Kreder et al., 2016a; Wong et al., 2011). Because the water or ice phase interacts primarily with the lubricant, pinning at solid asperities is suppressed and interfacial toughness is greatly reduced.

Designing effective SLIPS requires careful matching of scaffold geometry, lubricant properties, and working fluid. The solid matrix must be preferentially wetted by the lubricant to ensure capillary retention; pore sizes and surface chemistry are selected so that the lubricant remains stable under shear, gravity, and thermal cycling (Wong et al., 2011). Lubricant retention is the primary challenge; depletion via evaporation, shear-driven drainage, or cloaking by the working fluid can gradually degrade performance. Strategies to mitigate this include using viscous or functionalized lubricants, employing re-entrant or overhanging pore geometries that enhance capillary anchoring, and combining SLIPS concepts with soft elastomeric substrates to further reduce interfacial toughness (Dhyani et al., 2022; Kreder et al., 2016a; Nistal et al., 2024).

Beyond ice, SLIPS also resist other fouling modes (e.g., scale, organisms, particulates), making them attractive for multi-functional anti-fouling and anti-icing applications. However, questions remain regarding long-term durability, environmental impact of lubricants, and performance under severe icing fluxes, which are active topics of research and are critically assessed in recent reviews (Dhyani et al., 2022; Kreder et al., 2016a; Nistal et al., 2024).

2.7 Application Case Studies

The practical value of icephobic surfaces depends not only on their laboratory τ_{ice} but also on how they perform under complex operating conditions, including mixed ice morphologies, erosion, and thermal cycling. This section highlights four representative application areas—aircraft, wind turbines, power infrastructure, and sensors—where passive or hybrid icephobic strategies are being explored.

2.7.1 Aircraft (Aviation)

Transport and commuter aircraft currently rely primarily on active systems (hot bleed air, electrothermal heaters, and pneumatic boots) to meet strict certification requirements (Board, 2007; Federal Aviation Administration, 2021). Passive coatings cannot replace these systems at present, but they can complement them by delaying ice accretion, reducing adhesion, and thereby lowering the duty cycle of de-icing systems and the amount of chemical de-icer required (He et al., 2021; Kreder et al., 2016a).

Coatings for aeronautical applications must withstand UV radiation, cosmic radiation, aerodynamic loads, rain and sand erosion, as well as de-icing chemicals, all while preserving the smoothness of aerodynamic surfaces. Recent icing-tunnel tests on superhydrophobic and icephobic coatings applied to aluminum or composite substrates showed slower ice accretion, reduced residual ice thickness, and easier shedding compared with uncoated controls, particularly under glaze-icing conditions relevant to in-flight icing (Piscitelli et al., 2025). However, performance often degrades after rain-erosion and sand-erosion exposure, highlighting durability limits (Nistal et al., 2024; Piscitelli et al., 2025).

Hybrid solutions pairing low-power electro-thermal heating with passive coatings are especially promising where fully active systems are impractical or too energy-intensive, such as on small unmanned aerial vehicles (UAVs) or rotorcraft components (Dhyani et al., 2022; Parent & Ilinca, 2011). In such concepts, the coating reduces the adhesion strength and required heat flux, while the heater provides robustness under severe icing events.

2.7.2 Wind Turbines

Icing on wind-turbine blades reduces power output, increases aerodynamic noise, and can generate dangerous ice throw. Field measurements and simulations indicate substantial energy losses during icing seasons at cold-climate sites (Gao & et al., 2021; Parent & Ilinca, 2011). Passive icephobic coatings on leading edges and suction sides can facilitate centrifugal shedding and reduce adhesion of wet snow or freezing drizzle, thereby shortening downtime and improving capacity factors (Dhyani et al., 2022; Kreder et al., 2016a).

Field trials and full-scale blade tests have shown that superhydrophobic or icephobic coatings can reduce ice accretion volume and increase shedding frequency, but durability of leading-edge coatings under rain erosion and particulates remains a major hurdle (Nistal et al., 2024; Parent & Ilinca, 2011). Combining coatings with modest blade heating (e.g., embedded resistive elements or warm air) is a promising compromise: coatings lower the energy required to clear ice, while heating ensures recovery during extreme events (Gao & et al., 2021; Parent & Ilinca, 2011). Coatings must also avoid aerodynamic penalties during ice-free operation, which constrains allowable roughness and thickness.

2.7.3 Power Lines and Other Infrastructure

Power transmission lines, insulators, and support structures experience significant icing loads in cold climates. Heavy accretions can cause mechanical overload, galloping, flashovers, and outages (Farzaneh, 2008; Makkonen et al., 2014). Icephobic coatings applied to conductors, insulators, and towers can reduce ice loads and facilitate natural shedding by wind-induced vibration or gravity.

For high-voltage equipment, electrical compatibility, ampacity, corona effects, and pollution flashover performance constrain allowable materials and coating thicknesses. Hydrophobic room-temperature-vulcanizing (RTV) silicone coatings on insulators have been shown to reduce wetting, delay ice accretion, and decrease the likelihood of icing-induced flashovers (Farzaneh, 2008; J.-L. Laforte et al., 1998). For towers, masts, and similar structures, robust polymer or composite coatings can decrease maintenance needs and mitigate hazards from falling ice, although re-application logistics and service life remain key considerations (C. Laforte et al., 2019; J.-L. Laforte et al., 1998; Nistal et al., 2024).

Emerging LIT and SLIPS-inspired coatings are being evaluated on power hardware in cold chambers and field test lines. Early results suggest that even partial reductions in τ_{ice} can significantly decrease the frequency and severity of icing events when combined with appropriate line design and maintenance practices (Farzaneh, 2008; C. Laforte et al., 2019).

2.7.4 Sensors and Devices

Delicate sensors—including airport weather sensors, anemometers, LiDAR units on autonomous vehicles, camera lenses, and drone-mounted cameras—are also prone to icing and frosting. Even a thin ice layer can render such devices inoperative or degrade measurement accuracy. Transparent or translucent icephobic coatings that maintain optical clarity while reducing frost and ice accumulation are therefore of growing interest (Dhyani et al., 2022; Kreder et al., 2016a).

Examples include superhydrophobic or liquid-infused coatings on CCTV domes and optical windows, which can reduce frost formation and promote rapid clearing when subjected to mild heating or airflow. Sol–gel- or nanoparticle-based transparent coatings have been explored for automotive windshields and goggles, combining anti-fog (condensation control) with hydrophobic rain-repellent properties. For small unmanned aircraft, factory-applied hydrophobic or icephobic coatings on rotor blades and airframes have been reported to slow ice buildup and extend flight time in icing fog compared with uncoated vehicles, offering a passive means of risk reduction (Dhyani et al., 2022).

Similar strategies are being considered for sensors on power infrastructure (line monitoring sensors, ice detectors) and wind turbines (blade-mounted ice sensors), where icing of the sensor itself can compromise monitoring and control. In these applications, coatings must not interfere with sensor operation (optical, thermal, or electrical) and may be combined with low-power local heating or self-diagnostic algorithms.

Overall, across these case studies—aircraft, wind turbines, power lines, and sensors—icephobic surfaces show substantial potential to alleviate icing problems. In most realistic scenarios, they are most effective as part of a multi-faceted strategy: combining coatings with targeted heating, mechanical actuation, or design changes to manage ice accretion and shedding in an energy-efficient, robust manner (Dhyani et al., 2022; C. Laforte et al., 2019; Nistal et al., 2024; Parent & Ilinca, 2011).

2.8 Challenges and Future Outlook

While significant progress has been made in understanding and improving icephobic surfaces, several critical challenges remain before they can be widely deployed in industry. In this section, we discuss these challenges and highlight corresponding directions for future research and development.

2.8.1 Durability Under Real-World Conditions

A recurring challenge is the durability (or lack thereof) of many icephobic coatings. The very features that give a surface low ice adhesion—micro/nano textures, soft polymers, lubricant films—are often vulnerable to wear and degradation. Superhydrophobic coatings, for instance, can lose their water repellency if the nano-textures are damaged or contaminated. Lubricant-infused surfaces may gradually lose lubricant through evaporation or washing. UV radiation can break down organic coatings over time. Therefore, enhancing durability is a top priority.

Possible approaches include:

- *Nanocomposites:* Embedding wear-resistant nanoparticles in a resilient matrix to create coatings that are both robust and icephobic. For example, adding silica or alumina particles to a fluoropolymer can improve scratch resistance. Some studies have used inorganic fullerene-like nanoparticles (WS_2) in epoxy to increase durability of icephobic paints.
- *Self-healing coatings:* Incorporating microcapsules or dynamic polymer networks that can repair damage. For example, microcapsules that release a hydrophobic agent when ruptured could help a scratched superhydrophobic coating restore its low hysteresis. While self-healing concepts are often proposed for anti-corrosion, they could benefit anti-icing surfaces as well.
- *Surface renewal:* In some cases, accepting that a coating is sacrificial and making it easy to renew is a practical solution. Examples include adhesive icephobic tapes that can be peeled off and replaced, or blades designed with quick-apply coating cartridges for maintenance crews.

Another aspect of durability is maintaining performance under repeated icing/de-icing cycles. Some coatings show excellent low adhesion on the first cycle, but after many ice detachments, their performance degrades (possibly due to micro-cracks or loss of hydrophobic molecules). Therefore, cyclic testing is important. In the lab, accelerated aging tests such as abrasion, freezing/thawing, and salt spray are being applied to promising coatings to identify failure modes (Nistal et al., 2024). Going forward, a key objective will be to develop coatings that maintain low ice adhesion over many thousands of cycles while resisting mechanical and environmental damage.

2.8.2 Environmental and Safety Factors

New materials for icephobic surfaces must also be evaluated for environmental impact and safety. Some early superhydrophobic coatings used long-chain perfluorochemicals, which are now known to be environmentally persistent and potentially harmful (PFAS chemicals). Future coatings are therefore trending toward fluorine-free formulations, using alternatives such as silicones, hydrocarbon waxes, or zwitterionic polymers that are more eco-friendly while still providing low surface energy.

Additionally, any debris or byproducts from coatings must not introduce other hazards. For instance, if a coating flakes off during ice shedding, those flakes could cause FOD (foreign object debris) issues in aviation or clog filters. Using strongly bonded coatings or soluble films that do not produce hard debris can mitigate such concerns.

Compatibility is another important consideration: an icephobic coating on a power line or aircraft must not adversely affect other properties such as electrical conductivity (for ground equipment), flame retardancy, or radar signature (for stealth surfaces). This means coatings often have to be multifunctional, or at least benign in other respects. Future work is likely to focus on eco-friendly, regulation-compliant formulations and on layered or gradient systems (e.g., a thin icephobic topcoat over a traditional protective coating) that satisfy multiple performance requirements simultaneously.

2.8.3 Standardization of Testing and Certification

Comparing results between different studies is difficult without standardized tests. One important step is the development of consensus standards for ice adhesion measurement (already underway with organizations like ASTM Committee G-21 on Antifreeze and Ice Control). With standard methods, coating developers can have clear targets (e.g., "must achieve ARF of 4 or greater in ASTM XYZ test after 100 abrasion cycles"). Certification processes for aviation or energy applications will likely require demonstrating performance after environmental conditioning (humidity, salt fog, UV exposure, etc.). Thus, test protocols that simulate realistic service conditions are essential.

Another important aspect is the development of reliable accelerated aging tests that correlate with field performance. For example, a rain erosion test rig (such as a whirling arm rain tester) might be used to simulate years of precipitation impact on a blade coating in a matter of hours. Similarly, alternating freezing rain and thaw cycles in a lab chamber could simulate seasonal stresses on a coating. Widespread deployment of prototypes on wind farms, test aircraft, power lines, and other infrastructure will provide valuable field data to validate these protocols. In the long term, harmonized standards and robust laboratory–field correlations will be crucial for certification and large-scale adoption.

2.8.4 Multi-Functionality and Adaptive Systems

Future anti-icing approaches are likely to integrate multiple functions in a single system. For example, an icephobic surface might also incorporate de-icing capability by being electrically conductive (to allow Joule heating) or photothermally active (to absorb sunlight and heat up). A recent trend is the development of photothermal icephobic coatings that are dark-colored or have embedded photothermal particles (such as graphene or gold nanorods); these coatings passively heat under sunlight to prevent ice buildup(Dhyani et al., 2022). Another concept is using magnetically responsive coatings that can vibrate or flex slightly under an external magnetic field, aiding ice detachment.

There is also growing interest in *sensing* capability: a coating that can detect icing (via embedded optical fiber, microwave resonators, or impedance changes) and then trigger an active response or alert operators. For instance, a "smart skin" on a wing could detect a change in dielectric constant when ice forms and then activate a minor heating element only where needed, minimizing energy use.

While these ideas extend beyond purely passive surfaces, they underscore a future in which the boundary between passive and active anti-icing is blurred. Coatings may be mostly passive but incorporate small, intelligent components to improve reliability and efficiency, enabling hybrid systems that combine low ice adhesion with targeted, low-power interventions.

2.8.5 Machine Learning and Computational Design

Machine learning (ML) is increasingly being used to explore complex material design spaces. For icephobic surfaces, ML can help identify patterns in what makes a surface effective. For example, Ringdahl *et al.* (Ringdahl, Xiao, He, & Zhang, 2021) used an ML model to predict ice adhesion from nanoscale roughness parameters and found it could achieve good accuracy . Such models, once trained on sufficient data, could allow researchers to virtually screen thousands of texture–chemistry combinations and pinpoint promising candidates for experimental testing, thereby accelerating discovery.

ML could also help optimize trade-offs—for instance, balancing hydrophobicity with durability. If provided data on both ice adhesion and abrasion resistance for a series of coatings, an ML algorithm might find a ”sweet spot” formulation that sacrifices a small amount of water repellency but gains substantially in toughness, yielding superior overall performance.

Another computational avenue is high-fidelity icing simulation. Combining CFD (computational fluid dynamics) with icing models (Nohooji & Tembely, 2025) and surface physics can predict how ice will accrete and detach on different surfaces. While computational icing models already exist (e.g., for aircraft icing certification), they often assume idealized surface conditions. More refined models that incorporate varying contact angles, contact-angle hysteresis, and surface roughness could provide deeper insight into how different icephobic treatments affect ice accretion. Building shared databases and standardized workflows for such simulations, coupled with ML analysis, is a promising direction for guiding experiments and design.

2.9 Conclusion

Icephobic surface engineering has evolved into an interdisciplinary field aimed at tackling the long-standing problem of ice accretion. In this review, we surveyed the fundamental science of ice formation and adhesion, and how surface wettability and topography influence these processes. We examined how micro- and nano-structured superhydrophobic surfaces can delay ice onset and reduce ice–surface bonding, while also highlighting that extreme water repellency alone does not guarantee ultra-low ice adhesion. The development of low-interfacial-toughness materials and slippery coatings has opened new frontiers, enabling order-of-magnitude reductions in ice adhesion strength compared to traditional materials.

Notably, surfaces such as soft silicone coatings and lubricant-infused porous surfaces have achieved τ_{ice} values in the tens of kPa or below, meaning ice can often shed under its own weight or a light wind. These are promising results that suggest passive de-icing of large structures is within reach. However, we also highlighted the remaining challenges, chief among them durability and long-term performance under realistic environmental exposures. Many icephobic treatments excel under controlled conditions but struggle to maintain performance after prolonged abrasion, UV radiation, contamination, and multiple icing–de-icing cycles.

Looking ahead, research is poised to deliver coatings and surface treatments that are not only highly icephobic but also robust, environmentally benign, and compatible with demanding applications such as aviation, wind energy, and power transmission. Multifunctional and intelligent surfaces—those that combine passive icephobicity with active sensing, photothermal or electrical de-icing, and system-level integration—represent an especially exciting direction. In parallel, the rise of machine learning and advanced simulation in materials science is likely to accelerate innovation, helping to navigate the complex design space of textures, chemistries, and compliance levels more efficiently than before.

The case studies discussed (from aircraft and wind turbines to power lines and sensors) show that applying icephobic coatings can indeed mitigate icing issues, though rarely eliminate them entirely. The emerging consensus is that a holistic approach works best: design surfaces that make it hard for ice to stick, and supplement them with minimal energy input or mechanical action to handle the most stubborn ice. This strategy can dramatically reduce the energy and operational costs associated with de-icing in many sectors.

Ultimately, the goal is to enable critical infrastructure and vehicles to operate safely and efficiently through icing conditions with minimal intervention. Achieving this will require not only breakthroughs in materials and surface design, but also careful integration into systems, rigorous standardized testing, and sustained attention to durability, environmental impact, and maintenance over the lifetime of the application.

Table 2.1: Representative wetting and ice-adhesion performance for common surface types. WCA: static water contact angle; CAH: contact angle hysteresis; τ_{ice}: shear ice adhesion strength at $-10\,^{\circ}\mathrm{C}$ (approximate ranges); ARF: adhesion reduction factor relative to uncoated aluminum (baseline $\tau_{\text{ice}} \approx 200\,\mathrm{kPa}$).

Surface Type	**WCA**	**CAH**	τ_{ice} **(kPa)**	**ARF**	**Reference(s)**
Bare aluminum (polished)	$\approx 75^{\circ}$	high	200 to 300	1.0	(J.-L. Laforte, Allaire, & Laflamme, 1998; Parent & Ilinca, 2011)
Smooth hydrophobic coating (e.g., PTFE)	100 to 115°	10 to 20°	100 to 150	≈ 2	(Menini & Farzaneh, 2011)
Superhydrophobic (micro-rough)	150 to 160°	$< 10^{\circ}$	30 to 60	4 to 8	(Kulinich & Farzaneh, 2009; Nguyen et al., 2018)
Superhydrophobic (nano-rough)	150 to 155°	$< 15^{\circ}$	50 to 80	3 to 5	(Menini & Farzaneh, 2011; **?**)
Soft silicone coating (low modulus)	110 to 120°	$< 20^{\circ}$	5 to 20	> 10	(Golovin et al., 2016)
SLIPS (lubricant-infused)	100 to 115°[a]	$< 5^{\circ}$	10 to 30	≈ 10	(Golovin et al., 2016; Wong et al., 2011)
Hydrogel or ice-like coating	$\approx 90^{\circ}$	n/a	≈ 1	$\gg 10$	(Golovin et al., 2016)

[a] SLIPS typically exhibit very low hysteresis; static WCA may be moderate.

Chapter 3

Towards Predicting Ice Adhesion on Thermally Sprayed Icephobic Surfaces through Multifractal Analysis

Manuscript in preparation for submission to Langmuir: M. Hassani, M. Tembely et al., "Towards Predicting Ice Adhesion on Thermally Sprayed Icephobic Surfaces through Multifractal Analysis."

Abstract

The buildup of ice on operational surfaces poses serious safety and efficiency challenges across key industries, including aviation, energy, and power transmission. While passive ice-mitigation strategies have shown promise, a fundamental knowledge gap persists in quantitatively linking surface microstructural properties to anti-icing and ice-adhesion performance. In addition, existing molecular-dynamics (MD) simulations do not always reproduce laboratory measurements of ice adhesion, highlighting the need for a more realistic description of multiscale ice–surface interactions. To help reconcile these discrepancies, the present study applies multifractal analysis to characterize complex surface topographies obtained from confocal microscopy and to relate them to surface wettability, droplet freezing behavior, and ice adhesion. We investigate a set of samples comprising TiO_2 coatings fabricated on aluminum substrates using the Suspension Plasma Spray (SPS) technique, along with commercial superhydrophobic coatings as benchmarks. These surfaces are comprehensively characterized using standard metrics (roughness, wettability, droplet contact time) and, critically, through multifractal analysis to gain deeper insight into their surface microstructure. The samples are then tested in an icing wind tunnel to evaluate ice accumulation, and ice shear-adhesion strength is measured to assess the icephobic performance of each surface. Our findings reveal that traditional metrics such as static contact angle are poor predictors of ice adhesion, whereas fractal parameters exhibit a strong correlation with icephobic behavior. In particular, optimal icephobicity—characterized by low ice adhesion, long freezing delay, and short droplet contact time—is associated with a high fractal dimension (D) and a low scaling constant (G), a combination that promotes a stable Cassie–Baxter state and reduces the effective solid–liquid contact area. Finally, feature-importance analysis was performed to assess the impact of the icing-metric parameters on ice adhesion. These results have the potential to significantly improve anti-icing strategies in aerospace applications, thereby contributing to safer and more efficient operations.

Keywords: Thermal Spray; Icephobic coatings; Multifractal Analysis; Icing

3.1 Introduction

Ice accumulation on exposed operational surfaces is a widespread and costly challenge across numerous industries Farhadi, Farzaneh, and Kulinich (2011); Zhan, Pang, and Tan (2025). In aviation, ice on aircraft wings and control surfaces can severely alter lift and drag, increasing stall risk and, in extreme cases, leading to loss of control or crashes (J. Chen et al., 2012; Jung et al., 2011; Schutzius et al., 2015; Sojoudi, Wang, Boscher, McKinley, & Gleason, 2016). In the energy sector, icing on wind turbine blades reduces aerodynamic efficiency and power output (Homola, Virk, Wallenius, Nicklasson, & Sundsbø, 2010), while ice accretion on power lines can trigger mechanical failure and widespread outages (Zdero & Turan, 2010).

Traditional mitigation strategies rely on active de-icing systems such as electro-thermal heating, mechanical vibration, or chemical freezing-point depressants (Yang et al., 2025). Although effective, these methods add weight and system complexity, require continuous energy input, and may pose environmental concerns. These limitations have motivated substantial interest in passive surface-based approaches that resist frost, ice accretion, or ice adhesion without external power.

Passive anti-ice surfaces are typically classified into two functional groups: *anti-icing* surfaces, which delay or prevent ice formation, and *icephobic* surfaces, which allow ice that does form to be removed with minimal force. In practice, surfaces with ice adhesion strengths below approximately 100 kPa are often considered icephobic (Kreder, Alvarenga, Kim, & Aizenberg, 2016b). However, anti-icing and icephobic behavior do not always coincide; some textured coatings may delay freezing yet strongly retain ice once formed, whereas others shed ice easily but do little to slow its formation (Sarshar, Song, Swarctz, Lee, & Choi, 2018). Thus, developing surfaces that simultaneously minimize ice accumulation and ice adhesion remains a central research challenge.

One widely studied pathway toward passive ice protection is the use of superhydrophobic surfaces. A surface is classified as superhydrophobic when it exhibits a water contact angle (WCA) above 150° and minimal contact-angle hysteresis ($\leq 10^\circ$) (B. Li et al., 2023; Mohammadi, De Pauw, Tembely, & Dolatabadi, 2013). Such surfaces combine low-surface-energy chemistry with carefully engineered micro- and nanoscale roughness (Giannuzzi et al., 2019; Hoshian, Jokinen, Somerkivi, Lokanathan, & Franssila, 2015). Their non-wetting behavior is explained by the Cassie–Baxter model (W. Chen et al., 2025), which describes water droplets resting atop surface asperities with air trapped beneath (Josyula et al., 2024). This composite solid–air–liquid interface reduces the true solid–liquid contact area, enabling droplets to bead and roll off before freezing. The trapped air layer also provides thermal insulation, reducing heat transfer and delaying ice nucleation (Jiang et al., 2024; L. Wang et al., 2024). To maintain this Cassie state under realistic conditions such as high humidity or droplet impact, hierarchical multiscale roughness is essential; without it, water infiltrates the texture, transitioning the surface to the high-adhesion Wenzel state (Collins & Safiuddin, 2022; Maghsoudi, Momen, & Jafari, 2023). Natural examples such as lotus leaves illustrate how multiscale roughness can stabilize air pockets and prevent wetting. Numerous studies confirm that superhydrophobic surfaces generally delay icing by sustaining a metastable Cassie state.

Despite the recognized importance of surface texture, quantitatively characterizing complex multiscale roughness and linking it to icing performance remains difficult. Conventional roughness metrics such as the average roughness R_a or root-mean-square roughness R_q provide limited insight; they collapse rich topographical information into single-scale averages and are highly sensitive to measurement resolution and scanning window size (Goodhand et al., 2016; Jacobs, Pastewka, & Editors, 2022). To overcome these limitations, fractal analysis has emerged as an alternative approach of describing rough surfaces across a continuum of scales. Fractal approaches capture self-similar features using scale-independent parameters, and the widely used Weierstrass–Mandelbrot (W–M) function models a rough surface as a superposition of sinusoidal components spanning multiple frequencies and amplitudes (Hatte, Kant, & Pitchumani, 2023; Jain & Pitchumani, 2017).

Such fractal descriptions enable predictive models for wetting. Jain and Pitchumani (2017) proposed a theoretical framework relating a surface's fractal dimension D to the projected solid–liquid contact fraction Φ in the Cassie–Baxter state. This framework links measurable fractal parameters to macroscopic wetting behavior. Building on this, Hatte et al. (2023) used numerical simulations to show that increasing D or expanding the scale range L^* promotes a higher apparent contact angle and reduces true solid–liquid contact. Collectively, prior work suggests that fractal descriptors—especially the fractal dimension D—could serve as meaningful parameters to characterize multiscale surfaces.

However, a critical gap remains: no experimental studies to date have directly correlated the fractal characteristics of real, engineered surfaces with their measured icephobic performance. Although many coatings have been experimentally evaluated for icing and adhesion, the link between theoretical fractal descriptors and actual icephobic behavior remains untested. In particular, it is unknown how the fractal features of surfaces produced via Suspension Plasma Spray (SPS)—a highly scalable industrial coating method—relate to icing resistance.

The present work addresses this gap. We systematically investigate a series of SPS-fabricated TiO_2 coatings with varying textures and, for the first time, apply fractal analysis to correlate multiscale roughness with wetting and icing performance. Eleven coating variants were produced by adjusting SPS processing parameters, and a commercial superhydrophobic coating (NeverWet) was included for comparison. We characterized each surface's topography (via confocal microscopy and SEM), wettability (static and dynamic contact angles, droplet impact behavior), and icing response (freezing delay, ice accretion, and ice adhesion strength). By extracting the fractal dimension and scaling parameter from surface profiles, we aim to identify relationships between fractal descriptors and key icephobic metrics.The remainder of this paper details the experimental methods, presents the results, and discusses the implications of multifractal analysis for designing durable icephobic coatings.

3.2 Materials and Methods

The methodology employed in this study was designed to systematically fabricate and evaluate a series of icephobic surfaces, with the goal of correlating their physical and topographical characteristics to their functional performance against ice. Two primary pathways were used to create superhydrophobic surfaces on a common substrate material.

The first pathway involved engineering newly textured surfaces by depositing titanium dioxide (TiO_2) coatings using the Suspension Plasma Spray (SPS) technique, followed by a surface treatment to reduce surface energy. The second pathway employed a commercially available superhydrophobic spray coating, which served as a performance benchmark.

Following fabrication, all surfaces underwent a comprehensive two-stage characterization protocol. The first stage focused on quantifying intrinsic surface properties, including detailed roughness measurements, fractal analysis, wettability characterization, and droplet contact-time assessments. The second stage evaluated functional icephobic performance by measuring key parameters such as freezing-delay time and, critically, ice adhesion strength.

This structured approach enables the development of a clear link between the measured surface descriptors and the resulting ice adhesion behavior, thereby helping to identify the topographical features most responsible for icephobicity. A schematic overview of the complete workflow is presented in Figure 3.1.

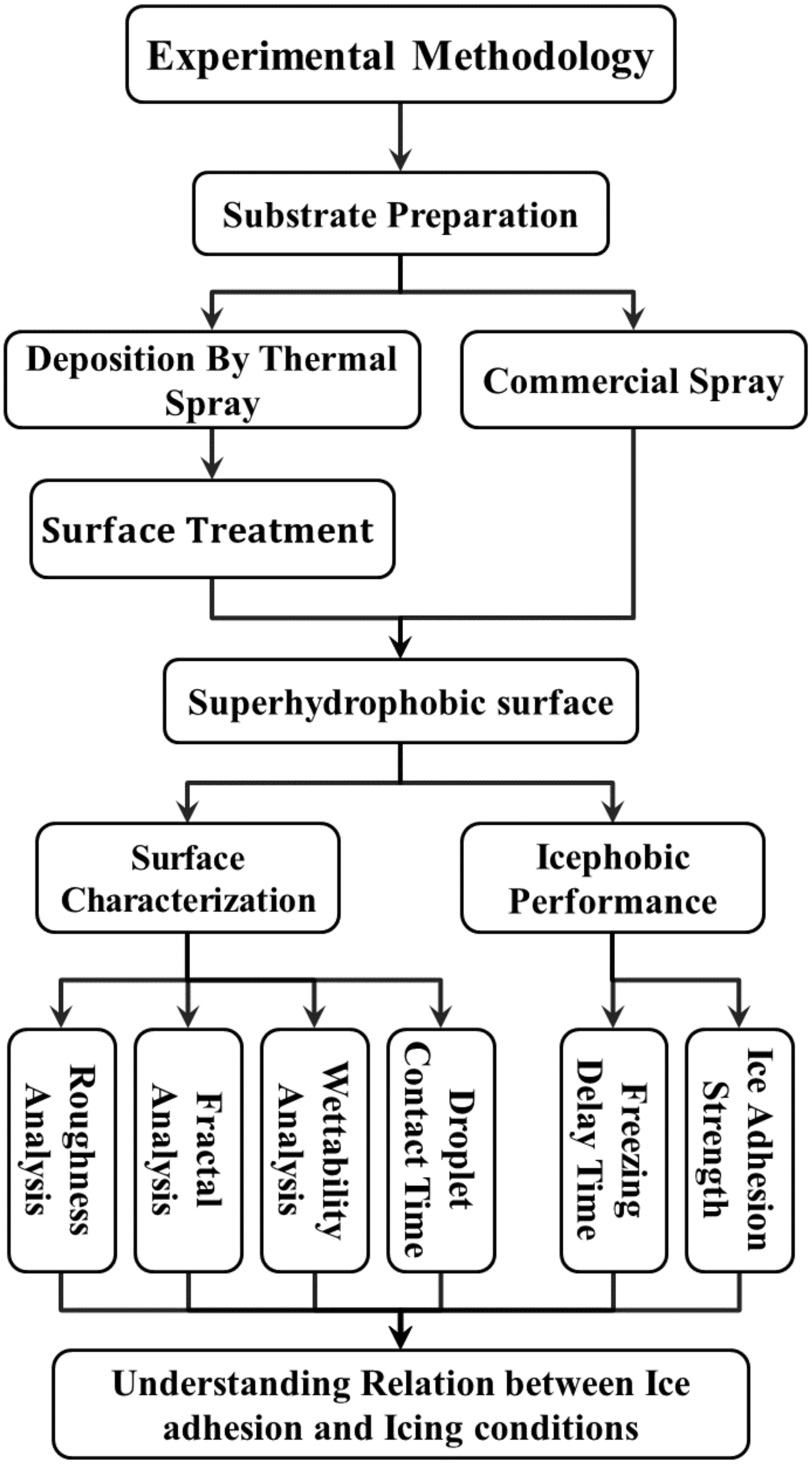

Figure 3.1: A flowchart illustrating the comprehensive experimental methodology, from substrate preparation and surface fabrication to the detailed characterization of surface properties and icephobic performance.

3.2.1 Substrate and Coating Deposition

Substrate Material

All coatings were deposited onto aluminum substrates (Al 6061 alloy, McMaster-Carr, Canada) with dimensions of 20 mm × 40 mm × 10 mm. Prior to coating, each substrate was grit-blasted with alumina abrasive and then ultrasonically cleaned in acetone followed by isopropanol. This surface preparation ensured a clean, roughened substrate to promote good coating adhesion.

Suspension Plasma Spray (SPS) Process

A series of eleven distinct TiO_2 coatings were fabricated using a Suspension Plasma Spray (SPS) technique, in order to generate a broad range of surface topographies. The coatings were deposited using an Oerlikon Metco 3MB plasma torch, a system well-suited for producing microstructured functional coatings. The feedstock was a suspension of sub-micron TiO_2 powder (mean particle size 500 nm) in an ethanol-based solvent with polyvinylpyrrolidone (PVP) added as a dispersant. This suspension formulation is known to yield hierarchical, ”cauliflower-like” surface features that promote superhydrophobicity (Sharifi et al., 2017). To create a diverse library of surface textures, key SPS process parameters were systematically varied from sample to sample. These parameters included the plasma torch stand-off distance, plasma power, number of spray passes, suspension solid concentration, and plasma gas flow rates. Each of these factors influences the coating morphology (for example, higher plasma power generally yields a rougher, more porous deposit, while increased stand-off distance can produce finer textures). The specific parameter combinations used for each of the eleven samples are detailed in Table 3.1. By design, this controlled variation in SPS conditions allows us to later examine how differences in process conditions translate into differences in surface fractal geometry and ultimately icing performance.

Commercial Benchmark Coating

In addition to the SPS-coated samples, a commercially available superhydrophobic coating (NeverWet, Rust-Oleum Corp.) was applied to identical aluminum substrates to serve as a benchmark. The application procedure meticulously followed the methodology reported by Yang et al.

Table 3.1: Suspension Plasma Spray (SPS) Deposition Parameters for TiO_2 Coatings.

Sample ID	Stand-off Distance (mm)	Solid Content (%)	Number of Passes	Plasma Power (kW)	Argon Flow Rate (L/min)
Sample1	30	10	10	25	60
Sample 2	30	10	15	25	60
Sample 3	40	10	10	25	60
Sample 4	50	10	10	25	60
Sample 5	50	10	15	25	60
Sample 6	50	10	10	33	60
Sample 7	50	15	10	25	60
Sample 8	50	10	10	30	60
Sample 9	60	10	10	33	60
Sample 10	60	10	10	30	60
Sample 11	60	10	10	25	75

(Yang et al., 2025) to ensure consistency and robustness. The substrate was first pre-cleaned with isopropyl alcohol (IPA). Subsequently, one layer of the primer (Part A) was applied, followed by five layers of the nanoparticle-based topcoat (Part B). The sample was then allowed to cure at ambient room temperature for 24 hours before any characterization or testing was performed.

3.2.2 Surface Characterization

An integrated approach was used to characterize the surface topography and wettability of each sample

Topography and Roughness Analysis

The surface topography of each coating was measured using a high-resolution confocal laser scanning microscope (Olympus LEXT OLS 4100). This non-contact optical profiler captures three-dimensional surface maps as well as two-dimensional height profiles. All samples were scanned at 50× magnification, covering a representative area of approximately 951 μm × 257 μm on each surface. From the 3D height maps, a comprehensive set of standard roughness parameters was extracted in accordance with ISO 25178. These included (but were not limited to) the arithmetic mean height Ra, root-mean-square height R_q, maximum peak height Rp, maximum valley depth R_v, and skewness R_{sk} of the height distribution. Collectively, these metrics quantify the amplitude and distribution of surface asperities for each sample. An example 2D surface profile extracted from the confocal scan is shown in Figure 3.2, illustrating the height variation across a line on the surface.

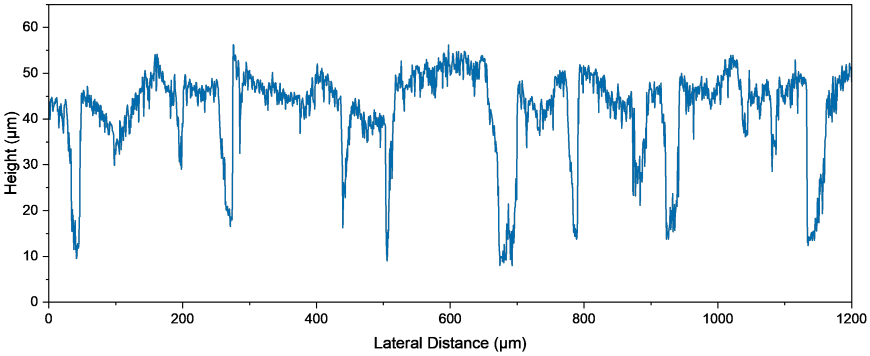

Figure 3.2: An example of a 2D roughness profile extracted from a surface topography scan. The plot shows the surface height variations (y-axis) along a single line across the sample's surface (x-axis).

Fractal Analysis

To overcome the limitations of conventional single-scale roughness metrics, the roughness profiles extracted from the confocal microscopy measurements were analysed within a self-affine fractal framework, following the approach of (Hatte et al., 2023; Jain & Pitchumani, 2017). The procedure comprised the following steps. First, a Fast Fourier Transform (FFT) was applied to each digitized roughness profile, $z(x)$, to obtain its power spectral density (PSD), $S(\omega)$, as a function of spatial frequency ω. The PSD was then represented on a log–log scale, as illustrated in Figure 3.3. The presence of a well-defined linear region in the log–log PSD is characteristic of a self-affine fractal surface and justifies the use of a Weierstrass–Mandelbrot (W–M) model to describe the surface roughness.

Within this framework, two fundamental fractal parameters are used to characterize the multiscale surface topography: the fractal dimension D and the scaling constant G. For a surface profile, the fractal dimension lies in the range $1 < D < 2$ and quantifies the complexity or "richness" of the roughness. Values of D close to 1 correspond to relatively smooth surfaces, whereas values of D approaching 2 indicate highly convoluted surfaces with pronounced fine-scale structure.

The scaling constant G controls the vertical amplitude of the roughness across scales: larger values of G correspond to greater height variations, while smaller values reflect lower-amplitude features superimposed on the surface.

In the W–M formalism, a rough profile can be represented as

$$y(x) = G^{D-1} \sum_{n=n_1}^{n_2} \frac{\cos\left(2\pi\gamma^n x\right)}{\gamma^{n(2-D)}}, \tag{10}$$

where γ^n denotes the wavenumbers associated with the surface features and n_1, n_2 define the range of spatial scales considered. The linear variation is defined over a frequency range from ω_l to ω_h, where $\omega_l = 1/L_{\max}$ corresponds to the maximum length scale of the asperity, and $\omega_h = 1/L_{\min}$ corresponds to the minimum length scale (Hatte et al., 2023).

For a self-affine fractal surface, the corresponding PSD follows a power-law dependence of the form

$$S(\omega) = \frac{G^{2(D-1)}}{2\ln(\gamma)} \frac{1}{\omega^{(5-2D)}}, \tag{11}$$

where γ is the frequency-density parameter. This relation shows that the spectral slope is directly linked to the fractal dimension, while the intercept reflects the scaling constant G. The pair (D, G) therefore provides scale-independent descriptors of the surface roughness, in contrast to classical roughness metrics that capture only single-scale statistics.

The fractal dimension D was obtained from the slope of the linear best-fit region of the log–log PSD curve. For a W–M surface, the slope m is related to D by (Hatte et al., 2023; Jain & Pitchumani, 2017)

$$m = 2D - 5. \tag{12}$$

Thus, D can be determined directly from the measured spectral slope.

Finally, the scaling constant G was computed from the intercept of the same linear regression using the W–M PSD relation in Eq. (11), with the frequency-density parameter typically taken as $\gamma = 1.5$ for random, naturally occurring surfaces (Hatte et al., 2023). Together, these steps yield the unique, scale-independent fractal parameters D and G, which quantitatively describe both the complexity and amplitude of the multiscale surface topography.

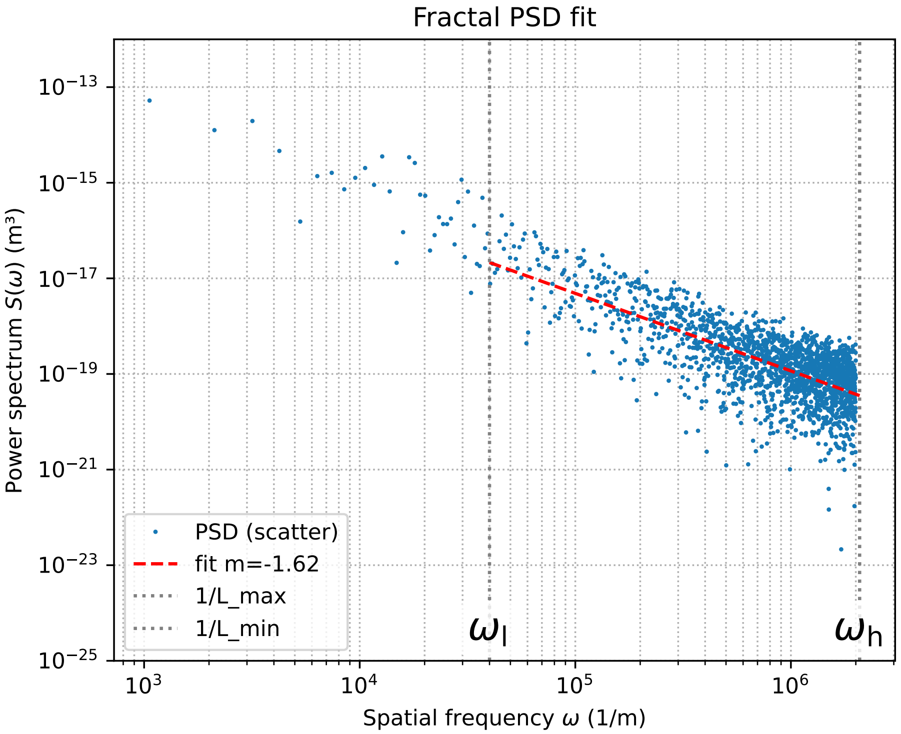

Figure 3.3: Power spectral density (PSD) of a sample surface profile plotted on a log-log scale. The linear fit (dashed red line) to a region of the spectrum is characteristic of a fractal surface and is used to determine the fractal parameters.

3.2.3 Wettability Measurements

Coating wettability characteristics were measured using the experimental setup shown schematically in Figure 3.4. Surface wettability was characterized through contact angle measurements using a goniometer. Static contact angle (SCA) was measured via the sessile drop method: a $\sim 5\,\mu$L water droplet was gently deposited on the horizontal surface, and the equilibrium contact angle was recorded. To assess dynamic wettability, advancing and receding contact angles were measured by expanding and contracting a droplet on the surface (Krishnan et al., 2005; Kwok & Neumann, 1999). Specifically, a droplet was slowly enlarged by adding water (for advancing angle, θ_A) and then slowly withdrawn (for receding angle, θ_R) until the contact line started to recede. The advancing and receding angles were measured at the onset of contact line motion. From these, the contact angle hysteresis (CAH) was calculated as the difference $\theta_A - \theta_R$. Contact angle hysteresis is an indicator of droplet adhesion and surface pinning—lower CAH generally implies that droplets can roll off or rebound more easily (Parvate, Dixit, & Chattopadhyay, 2020). All contact angle measurements were performed at ambient lab conditions ($\sim 22°$). Each reported value is the average of at least five measurements on different areas of the sample, with the uncertainty representing the standard deviation.

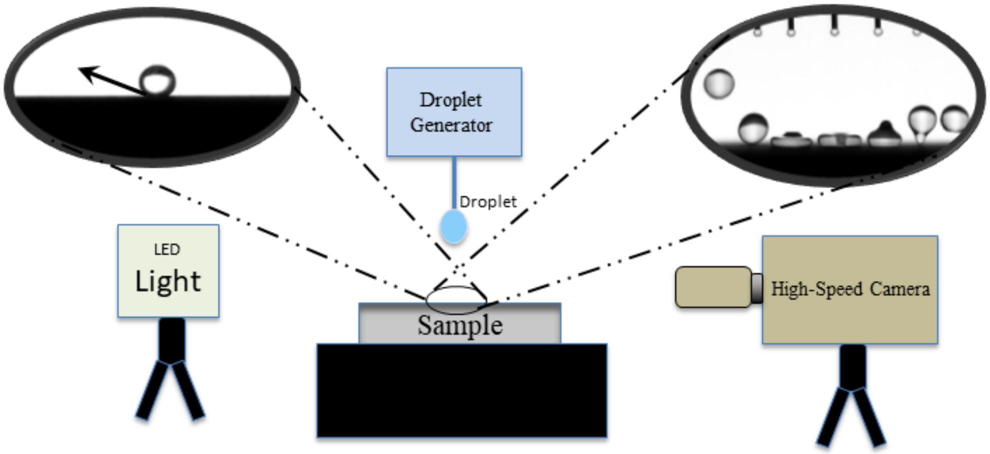

Figure 3.4: Schematic of the experimental setup for wettability and droplet contact time measurements.

Droplet Contact Time

To assess the dynamic water repellency of the surfaces, a droplet impact test was performed using the experimental setup shown schematically in Figure 3.4. This test followed the methodology of Chen et al. (X. Chen, Wang, Yang, Wang, & Lee, 2023). A single water droplet was released from a height of 10 mm above the substrate, ensuring zero initial vertical velocity. The interaction, including the spreading, recoiling, and potential rebound of the droplet, was captured with a high-speed camera. The contact time was precisely measured as the duration from the instant the droplet first made contact with the surface until the moment it completely detached (X. Chen et al., 2023). A typical image sequence illustrating this measurement is presented in Figure 3.5, which shows the droplet's behavior from initial impact to complete rebound. This metric is critical for applications involving impinging supercooled droplets, where minimizing interaction time is paramount to prevent icing.

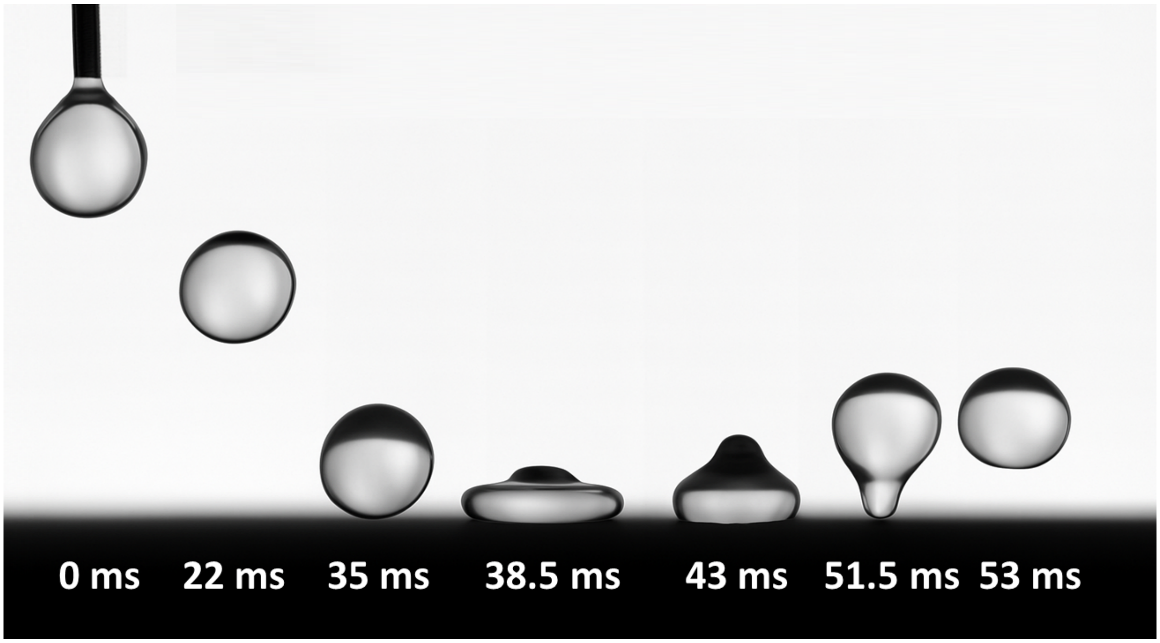

Figure 3.5: High-speed camera sequence showing a water droplet impacting, spreading, and rebounding from the surface. The contact time is the total duration the droplet is in contact with the substrate, from the first frame of impact to the last frame before liftoff.

3.2.4 Ice and Surface Interaction

We conducted three types of tests to evaluate each coating's performance under icing conditions, focusing on: (1) freezing delay time and (2) ice adhesion strength. Below we describe the procedures for these evaluations.

Freezing Delay Time

The anti-icing performance of the surfaces was first evaluated by measuring the freezing delay time of a supercooled water droplet. These experiments were conducted in a custom-built environmental ”Freezing Chamber,” which consists of a transparent, sealed enclosure to control humidity and a Peltier thermoelectric cooler that serves as the cold stage (Binninger, Unmüßig, Vergez, Bartel, & Schäfer-Welsen, 2024). The ability to control environmental conditions, particularly humidity, is critical, as it has been shown to significantly influence icing phenomena and measurement reproducibility (Burdin, Brulez, Mazurczyk, Leclercq, & Benayoun, 2025).

The standardized test procedure was as follows: The sample was mounted on the Peltier stage inside the chamber. The stage was cooled to a stable substrate temperature of -4°C. A single 10 µL droplet with diameter of 2.67 mm of distilled water, initially equilibrated to a temperature of 21°C, was gently deposited onto the center of the cooled surface. The freezing process was monitored and recorded with a high-speed camera. The **freezing delay time** was defined as the time elapsed from the moment of droplet deposition to the onset of nucleation, which is visually identified by the sudden flash of recalescence as the droplet releases its latent heat of fusion (Burdin et al., 2025). An image sequence illustrating this freezing event is shown in Figure 3.6.

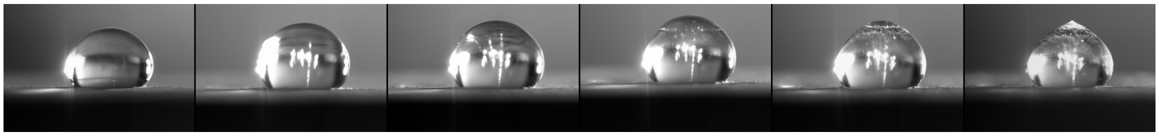

Figure 3.6: Image sequence illustrating the freezing process of a water droplet on the surface.

Ice Adhesion Strength

The force of adhesion between accreted ice and the substrate was measured using a robust, two-step procedure that simulates realistic atmospheric icing conditions, as detailed by Farahani (Farahani et al., 2023).

- **Step 1: Ice Accretion.** Each sample was mounted in an Icing Wind Tunnel (IWT) with its surface oriented at a 90° angle to the direction of the airflow. The IWT was operated under controlled conditions to produce glaze ice, which is known for its high adhesion strength. The specific icing parameters were an air temperature of -10°C, an air velocity of 45 m/s, a liquid water content (LWC) of 0.2±0.02 g/m³, a median volumetric diameter (MVD) of 20±3 µm, and an ice accretion duration of 180 seconds to ensure consistent ice formation across all samples.
- **Step 2: Shear Strength Measurement.** Immediately following the accretion period, the iced sample was quickly removed from the IWT and secured in a custom-built push-off test rig. A schematic of this apparatus is shown in Figure 3.7.

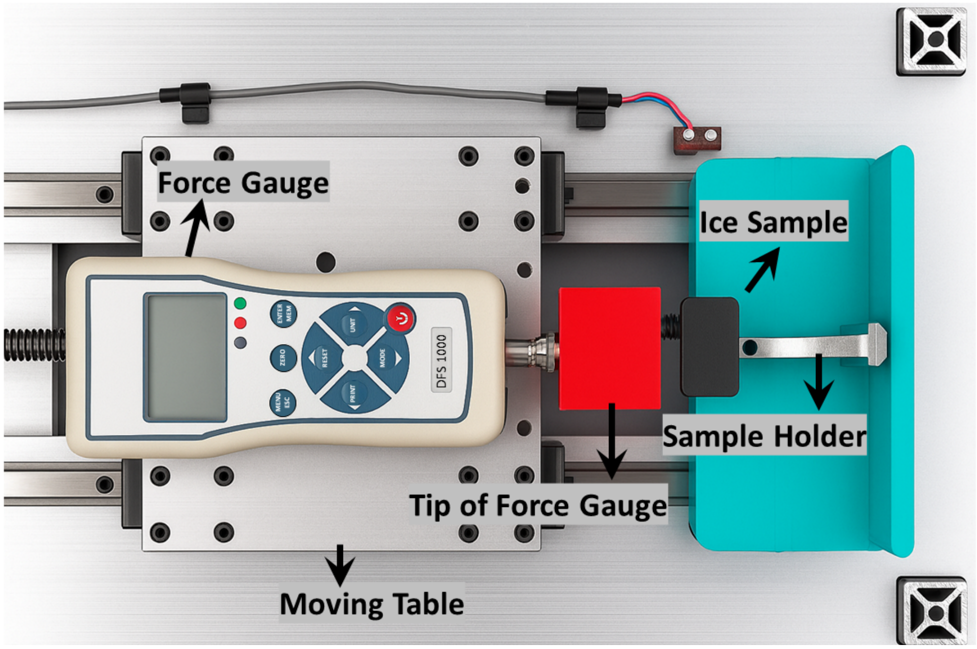

Figure 3.7: The custom-designed push-off apparatus for ice adhesion testing, showing the force gauge mounted on a moving table to apply a shear load to the ice sample.

This rig features a motorized linear stage equipped with a force transducer (Nextech, DFS-1000 series). A shear force was applied at a constant rate of 0.5 mm/s to the base of the accreted ice (Chaudhury & Kim, 2007), parallel to the substrate interface, at a height of approximately 1 mm above the interface to minimize bending moments (Chaudhury & Kim, 2007; Ghatak & Chaudhury, 2003). The maximum force (F_{max}) required to initiate fracture and detach the ice was recorded. The ice adhesion strength (τ_{ice}) was then calculated as the maximum force divided by the nominal ice-substrate contact area ($\tau_{ice} = F_{max}/A$).

3.3 Results and discussion

3.3.1 Surface Topography and Fractal Characterization

Scanning electron microscopy (SEM) confirmed that the superhydrophobic SPS coatings exhibit pronounced hierarchical roughness spanning multiple length scales. At increasing magnifications

(Figure 3.8), the surfaces are seen to consist of micron-scale base features decorated with progressively finer nano-asperities, forming a multiscale texture that is typically associated with robust superhydrophobic behaviour.

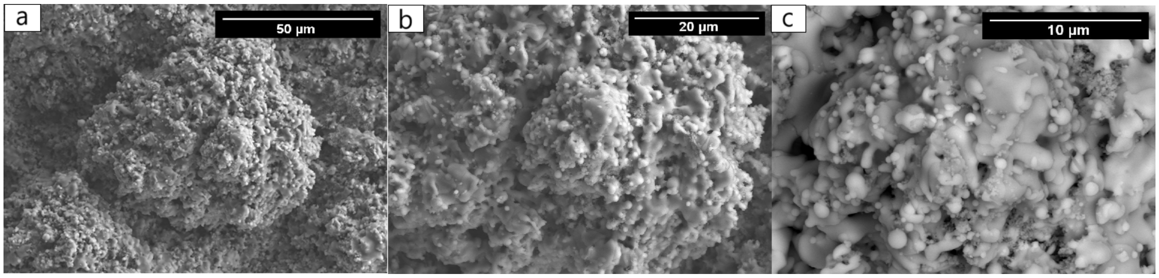

Figure 3.8: SEM images of a representative superhydrophobic SPS coating at increasing magnifications, highlighting the hierarchical micro/nanostructure of the surface.

At intermediate magnifications, the coated surfaces are composed of rounded, cauliflower-like clusters separated by well-defined grooves. These clusters display a multiscale hierarchy, with finer asperities superimposed on larger base structures. Such architectures are consistent with the Cassie–Baxter wetting regime: air pockets are trapped within the grooves and between asperities, reducing the true solid–liquid contact area and thereby increasing the apparent contact angle. This morphology underpins the superhydrophobic response of the coatings.

To further probe the three-dimensional character and orientation of these features, additional SEM images were acquired at a 30° tilt angle and at multiple viewing orientations (Figure 3.9). These tilted views emphasize the depth of the grooves and the overhanging asperities, which are expected to contribute to low water adhesion and, consequently, to favourable icephobic performance by facilitating droplet mobility and shedding.

Confocal laser scanning microscopy provided complementary three-dimensional height information and revealed how variations in SPS processing parameters influence the surface morphology. Coatings produced at lower plasma power and shorter standoff distance generally exhibit finer, more densely packed cauliflower-like features with a pronounced hierarchical structure. In contrast, higher power and larger standoff distances tend to generate larger, more melted and agglomerated surface structures. This trend is illustrated in Figure 3.10, which compares a low-power coating with

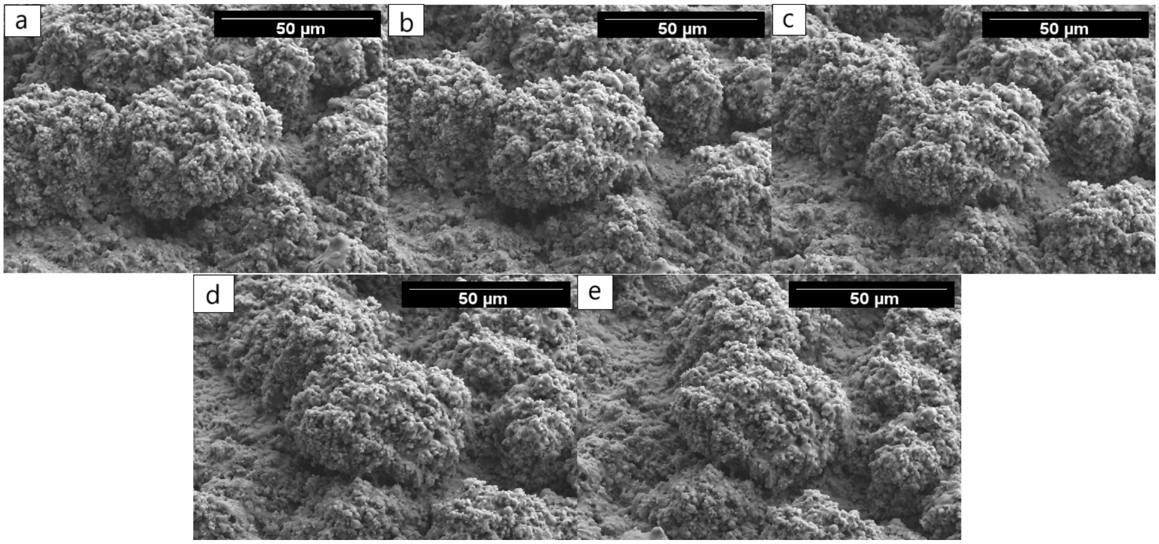

Figure 3.9: Tilted and rotated SEM images (30° increments) of individual cauliflower-like surface features, illustrating the three-dimensional morphology and spatial distribution of the hierarchical asperities that promote air entrapment and reduce the solid–liquid contact area in the Cassie–Baxter state.

fine hierarchical features to a high-power coating with coarser morphology. The commercial NeverWet coating, used as a benchmark, displays a markedly different texture dominated by agglomerated nanoparticles rather than well-defined cauliflower clusters.

Quantitative roughness parameters extracted from the confocal profiles are summarized in Table 3.2. The SPS coatings span a wide range of roughness amplitudes, with R_a values between approximately 5 µm and 13 µm, reflecting the diversity of topographies generated by the different SPS conditions. Most SPS surfaces exhibit positive skewness ($R_\mathrm{sk} > 0$), indicating height distributions dominated by protruding peaks, while the kurtosis values (R_ku) are close to or slightly above 3, consistent with near-Gaussian height distributions with occasional sharp asperities. The NeverWet reference shows a comparatively lower R_a (4.4 µm) and a slightly negative skewness, consistent with a surface dominated by finer asperities and shallow depressions rather than pronounced peaks.

To capture the multiscale character of the surface geometry beyond conventional single-scale roughness metrics, the confocal profiles were further analysed within the self-affine fractal framework outlined in Section 3.2.2. The Suspension Plasma Spray (SPS) process produced a library

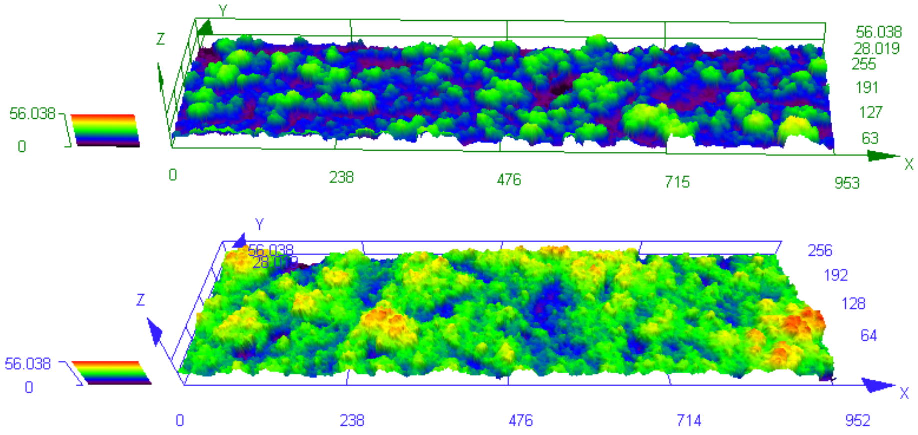

Figure 3.10: Representative 3D confocal microscopy images showing the surface morphology of SPS coatings produced under different conditions: (a) Sample 1 (25 kW power, 30 mm standoff distance), exhibiting fine hierarchical features; and (b) Sample 10 (30 kW power, 60 mm standoff distance), showing larger, more agglomerated structures.

Table 3.2: Roughness parameters measured from confocal microscopy profiles.

	R_p (μm)	R_v (μm)	R_z (μm)	R_c (μm)	R_t (μm)	R_a (μm)	R_q (μm)	R_sk	R_ku
Sample 1	21.4±5.1	15.6±3.6	36.4±9.1	24.7±3.3	36.4±8.1	6.4±1.6	7.8±1.1	0.7±0.2	2.6±0.6
Sample 2	26.4±4.2	21.4±4.1	47.9±8.4	32.4±4.1	47.9±7.2	9.3±1.7	11.4±1.4	0.2±0.3	2.4±0.7
Sample 3	22.4±5.8	21.3±2.8	43.7±6.4	34.5±6.7	43.7±6.4	7.6±1.8	9.3±2.1	0.1±0.4	2.6±0.3
Sample 4	24.6±3.7	22.2±4.8	47.5±6.3	33.0±5.9	47.5±9.4	7.0±0.9	9.1±1.6	0.5±0.1	3.2±0.9
Sample 5	47.5±7.1	22.2±3.9	69.7±8.5	28.5±4.7	69.7±9.8	13.4±1.3	17.2±1.0	1.1±0.5	3.3±1.0
Sample 6	18.2±5.0	16.1±3.9	34.3±7.8	24.1±6.6	34.3±7.8	4.9±1.0	6.2±1.3	0.2±0.3	3.0±0.5
Sample 7	22.5±6.1	23.4±6.2	45.8±10.7	32.0±10.0	45.8±10.7	6.3±1.3	8.2±2.0	-0.2±0.5	3.5±0.8
Sample 8	25.9±3.9	22.3±4.9	48.2±6.4	32.2±6.5	48.2±6.4	7.2±1.1	9.0±1.4	0.4±0.3	3.2±0.8
Sample 9	26.4±5.4	27.8±13.9	54.2±16.4	29.4±2.7	54.2±16.4	6.3±0.9	8.3±1.3	0.2±0.8	4.4±2.4
Sample 10	19.5±3.0	19.7±5.0	39.2±6.0	29.4±7.0	39.2±6.0	5.9±1.0	7.2±1.0	0.2±0.0	2.9±1.0
Sample 11	22.8±5.4	23.1±5.5	45.9±8.1	30.9±4.4	45.9±8.1	7.5±1.4	9.2±1.6	0.2±0.4	2.7±0.4
NeverWet	14.7±1.1	19.4±2.1	34.9±3.3	24.6±1.2	34.9±4.2	4.4±0.4	5.7±1.0	-0.5±0.1	3.4±0.2

of eleven distinct TiO_2 coatings spanning a broad range of morphologies, as illustrated by the representative SEM images in Figure 3.11. For each surface, the fractal dimension D and scaling constant G were extracted from the power spectral density (PSD) of the roughness profiles, and these parameters were related to the measured wettability.

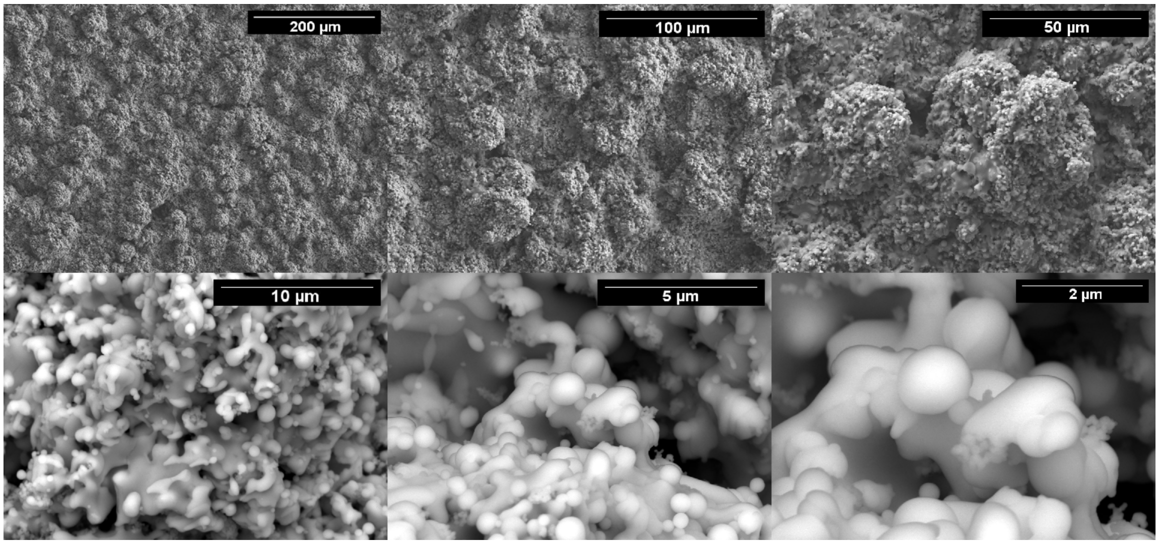

Figure 3.11: SEM images at different magnifications illustrating the fractal-like, multiscale geometry of the SPS-coated surfaces.

All SPS-coated TiO_2 surfaces, as well as the NeverWet benchmark, exhibited superhydrophobic behavior, with static contact angles (SCA) exceeding 150° (Table 3.3). This confirms the presence of a composite solid–liquid–air interface characteristic of the Cassie–Baxter state. Despite this common macroscopic response, the fractal parameters reveal substantial differences in the underlying topographies. The SPS coatings show fractal dimensions in the range $1.55 \leq D \leq 1.72$, indicating moderately to highly complex surface profiles. The corresponding scaling constants G vary by approximately a factor of six across the SPS set, reflecting differences in the amplitude of the roughness features. In contrast, the NeverWet coating exhibits a fractal dimension very close to 2 ($D = 1.98$) combined with a much smaller scaling constant ($G = 1.26$ μm), consistent with an extremely fine-featured hierarchical structure.

The combination of classical roughness metrics and fractal descriptors highlights that there is no simple one-to-one correspondence between a single-scale parameter such as R_a and the wetting

Table 3.3: Summary of fractal and wettability characterization results for all surfaces.

Sample	Fractal dimension D	Scaling parameter G (μm)	SCA (°)	Advancing CA (°)	Receding CA (°)
Sample 1	1.58	113	169 ± 1	170 ± 1	162 ± 2
Sample 2	1.69	25.0	163 ± 1	165 ± 2	156 ± 1
Sample 3	1.60	81.8	154 ± 1	156 ± 2	144 ± 2
Sample 4	1.60	97.0	159 ± 1	161 ± 1	154 ± 2
Sample 5	1.63	47.0	155 ± 2	156 ± 1	148 ± 1
Sample 6	1.55	124	157 ± 1	160 ± 1	148 ± 2
Sample 7	1.69	26.0	157 ± 2	159 ± 1	152 ± 2
Sample 8	1.67	32.0	164 ± 1	168 ± 2	159 ± 1
Sample 9	1.68	40.0	154 ± 1	158 ± 1	146 ± 1
Sample 10	1.72	21.6	156 ± 1	159 ± 1	148 ± 1
Sample 11	1.69	25.0	154 ± 3	159 ± 2	146 ± 2
NeverWet	1.98	1.26	165 ± 1	166 ± 1	164 ± 2

response. For example, Sample 5 has the largest average roughness ($R_A \approx 13.4$ µm) but only a moderate SCA of $155°$, whereas Sample 1 achieves one of the highest SCAs ($169°$) with a significantly lower R_a (≈ 6.4 µm) but a relatively large scaling constant G. This suggests that the distribution of roughness amplitude across scales, captured by (D, G), is more critical for achieving extreme superhydrophobicity than the mean roughness alone. Contact angle hysteresis (advancing–receding) remains below about $15°$ for all SPS coatings and is particularly small for NeverWet ($\sim 2°$), indicating generally low droplet pinning and supporting the potential of these multiscale surfaces for icephobic applications.

3.3.2 Icephobic Coating Performance–Ice Adhesion Estimation

The key icing performance metrics for all surfaces are summarized in Table 3.4. Despite all SPS coatings being superhydrophobic, we observed substantial variability in their freezing delay times, droplet impact contact times, and ice adhesion strengths. The freezing delay time (the time for a supercooled droplet to freeze) ranged from approximately 50 s on the least effective SPS surface (Sample 6) up to about 100 s on the best SPS surface (Sample 7). The droplet contact time during impact spanned roughly 23–31 ms, with the fastest rebounds on Samples 7 and 11 and the slowest on Sample 6. Most strikingly, the ice adhesion strength differed by almost 40% between certain coatings: some SPS samples had ice adhesion exceeding 300 kPa, whereas others were closer to 240–250 kPa. The commercial NeverWet coating exhibited the lowest ice adhesion in these short-term tests ($\sim$ 40 kPa), together with the longest freezing delay ($\sim$ 112 s) and the shortest contact time ($\sim$ 19 ms). However, NeverWet is known to suffer from poor mechanical durability and rapid performance degradation in service; here it is therefore used primarily as a reference for an "upper bound" in icephobic response rather than as a directly comparable engineering coating. Overall, these results underscore that surfaces with similarly high water repellency can nonetheless display very different anti-icing behaviour.

Table 3.4: Summary of icephobic performance test results for all surfaces.

Sample	Freezing delay time (s)	Contact time (ms)	Ice adhesion (kPa)
Sample 1	56.5 ± 3.22	29.00 ± 1.7	302 ± 41
Sample 2	84.4 ± 5.91	26.67 ± 0.5	241 ± 18
Sample 3	81.6 ± 6.35	26.33 ± 0.5	282 ± 23
Sample 4	92.7 ± 8.30	25.00 ± 1.0	310 ± 29
Sample 5	76.3 ± 11.2	27.67 ± 1.5	273 ± 26
Sample 6	50.2 ± 9.30	31.00 ± 1.0	330 ± 43
Sample 7	100.3 ± 5.60	23.36 ± 0.6	266 ± 13
Sample 8	73.6 ± 5.30	29.67 ± 0.5	259 ± 16
Sample 9	72.3 ± 4.70	26.67 ± 0.5	280 ± 25
Sample 10	63.6 ± 9.60	25.67 ± 0.5	271 ± 28
Sample 11	85.4 ± 7.10	23.67 ± 0.5	249 ± 24
NeverWet	112.0 ± 9.20	19.00 ± 1.0	40 ± 11

Surface wettability vs. ice adhesion: To assess whether conventional wettability metrics correlate with icephobicity, Figure 3.12 plots ice adhesion strength against the static (SCA), advancing (ACA), and receding (RCA) contact angles for all surfaces. The SPS coatings exhibit a relatively narrow but high range of static contact angles (approximately 154–168°); the corresponding advancing and receding angles also vary only modestly within the superhydrophobic regime. Within this window, all three contact-angle metrics show only weak trends with adhesion: the fitted linear regressions have coefficients of determination $R^2 \approx 0.11$ for SCA, $R^2 \approx 0.09$ for ACA, and $R^2 \approx 0.27$ for RCA. In particular, coatings with nearly identical SCAs can differ in adhesion by almost 100 kPa. The slightly stronger correlation with the receding angle reflects that lower contact-angle hysteresis (i.e. larger RCA) is somewhat beneficial, but the overall scatter demonstrates that contact angles alone are poor predictors of ice adhesion for these textured surfaces. Achieving a high static contact angle therefore appears necessary (none of the lower-angle surfaces were ice-phobic), but it is not sufficient; microstructural features beyond equilibrium wettability must be taken into account.

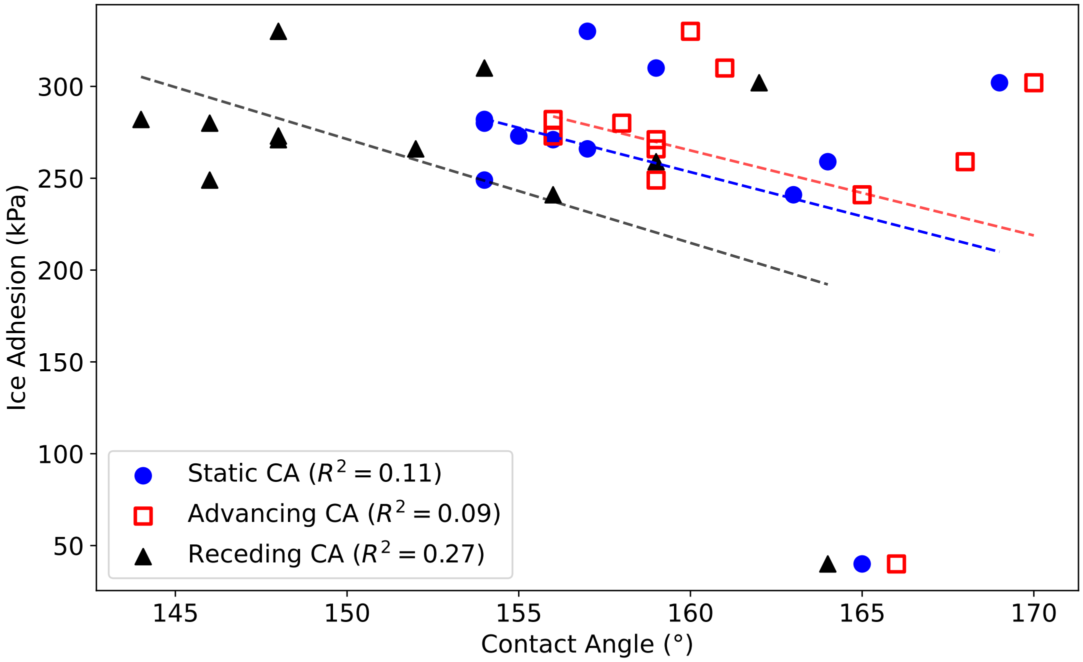

Figure 3.12: Ice adhesion strength as a function of static, advancing, and receding contact angles for all tested surfaces.

Droplet freezing and contact time vs. ice adhesion: We also examined how the dynamic anti-icing metrics—freezing delay time and droplet contact time—relate to ice adhesion (Figures 3.13 and 3.14). For the SPS coatings alone there is no one-to-one relationship: surfaces that delay freezing longer do not always show proportionally lower adhesion, and some coatings with relatively fast droplet rebound still exhibit comparatively high adhesion. Nonetheless, when the full set of surfaces is considered, a broader trend emerges. Figure 3.13 shows that, overall, longer freezing delay tends to coincide with lower adhesion (linear fit $R^2 \approx 0.47$), while Figure 3.14 indicates that coatings with shorter droplet contact times generally have lower adhesion ($R^2 \approx 0.60$). The NeverWet surface sits at the extreme of these trends, combining the longest freezing delay and shortest contact time with the lowest ice adhesion. Taken together, these observations suggest that the same surface characteristics that promote delayed icing and rapid droplet rebound also tend to weaken the ice–substrate bond, consistent with the picture of a stable Cassie–Baxter state and a reduced real ice–solid contact area.

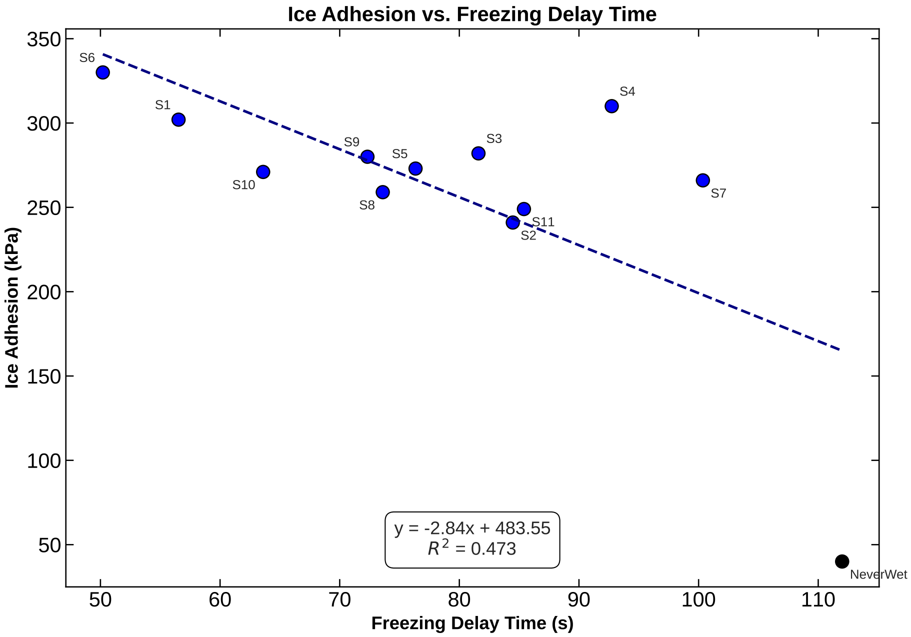

Figure 3.13: Ice adhesion strength as a function of freezing delay time for all tested surfaces.

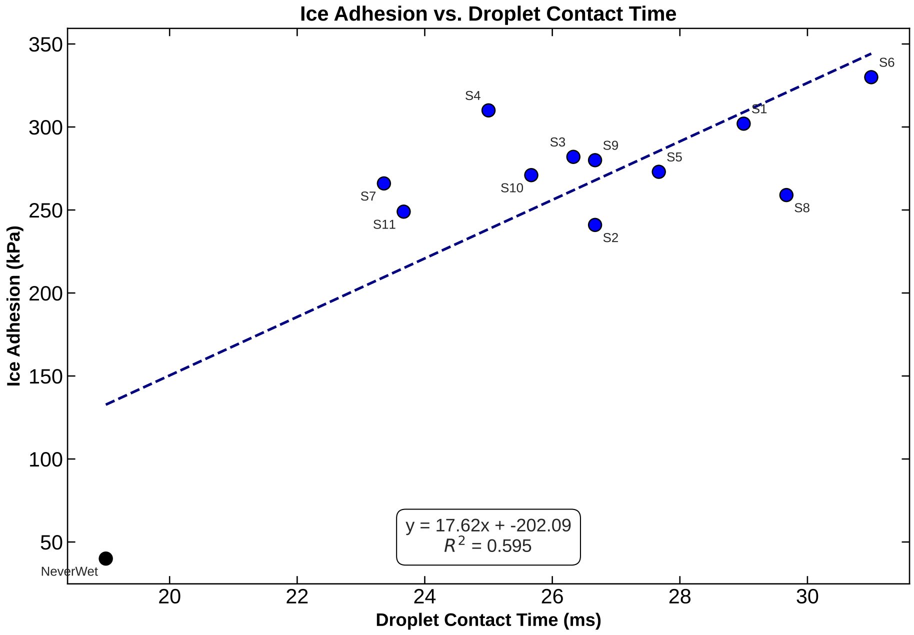

Figure 3.14: Ice adhesion strength as a function of droplet contact time.

Fractal dimension vs. ice adhesion: In contrast to the weak dependence on contact angle, a much clearer trend emerged when ice adhesion was plotted against the fractal dimension D of the surfaces (Figure 3.15). In general, ice adhesion strength decreases as D increases. SPS coatings with lower fractal dimensions ($D \approx 1.55$–1.60) tend to have higher adhesion (in the 280–330 kPa range), whereas those with higher fractal dimensions ($D \approx 1.7$) have lower adhesion (typically less than 270 kPa). Extrapolating this trend, the NeverWet surface—with the highest $D \approx 1.98$—exhibits the lowest adhesion ($\sim$ 40 kPa). Excluding NeverWet, the linear fit to the SPS data has a high coefficient of determination ($R^2 \approx 0.93$), indicating a strong correlation. Physically, a surface with higher fractal dimension possesses richer multiscale roughness and therefore more trapped air and less real contact area with the ice. Even though all surfaces here are nominally superhydrophobic, those with a more complex texture (higher D) make actual ice–solid contact over a smaller fraction of their area, leading to weaker adhesion. Additionally, hierarchical roughness can promote crack deflection or local stress concentrations at the interface, further lowering the force required to detach ice.

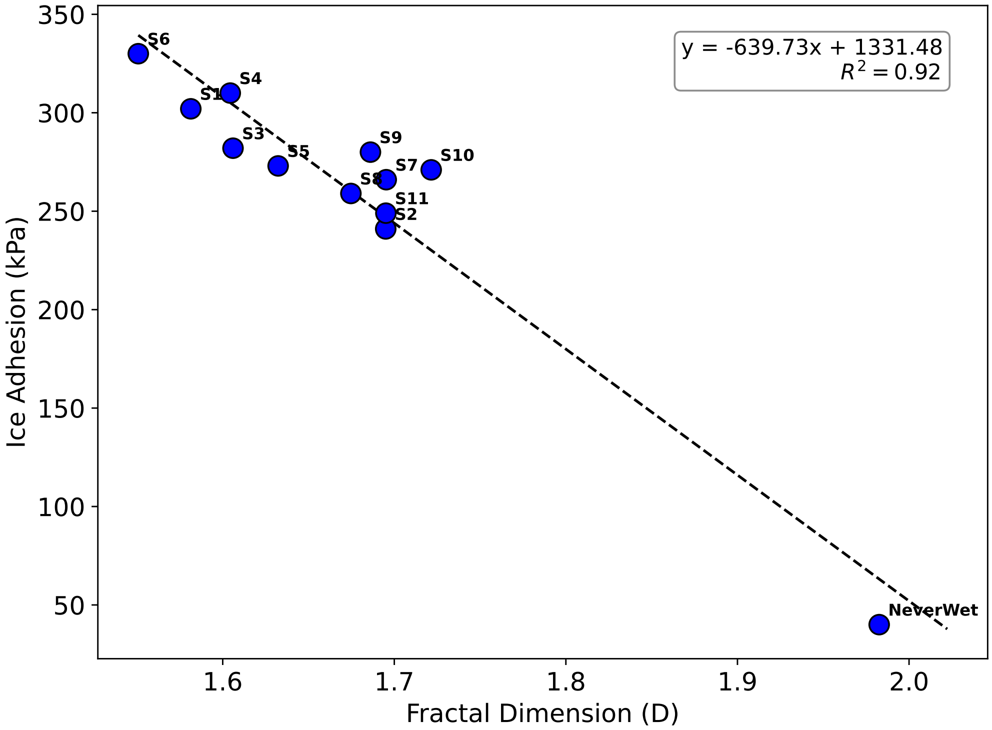

Figure 3.15: Ice adhesion strength as a function of fractal dimension D.

Scaling constant vs. ice adhesion: A similar correlation is observed for the fractal scaling constant G, which captures the vertical scale of the surface features. Figure 3.16 shows that coatings with lower G (finer, lower-amplitude roughness) generally exhibit lower ice adhesion. On a linear scale (top panel), there is a modest increase of adhesion with G ($R^2 \approx 0.44$), whereas plotting adhesion against $\log_{10} G$ (bottom panel) yields a much clearer approximate linear relationship ($R^2 \approx 0.92$). In other words, decreasing G corresponds to improved icephobicity. A small G implies that the surface roughness consists of numerous but shallow asperities that do not protrude far into the liquid/ice phase; the ice remains largely supported by an air cushion and can be sheared off with relatively little force. By contrast, high-G surfaces possess taller asperities that can penetrate through the air layer and form strong anchors for ice. Again, NeverWet lies at the extreme end of this trend, with the smallest G (by roughly an order of magnitude) and the weakest ice adhesion, while the SPS coatings populate the intermediate region.

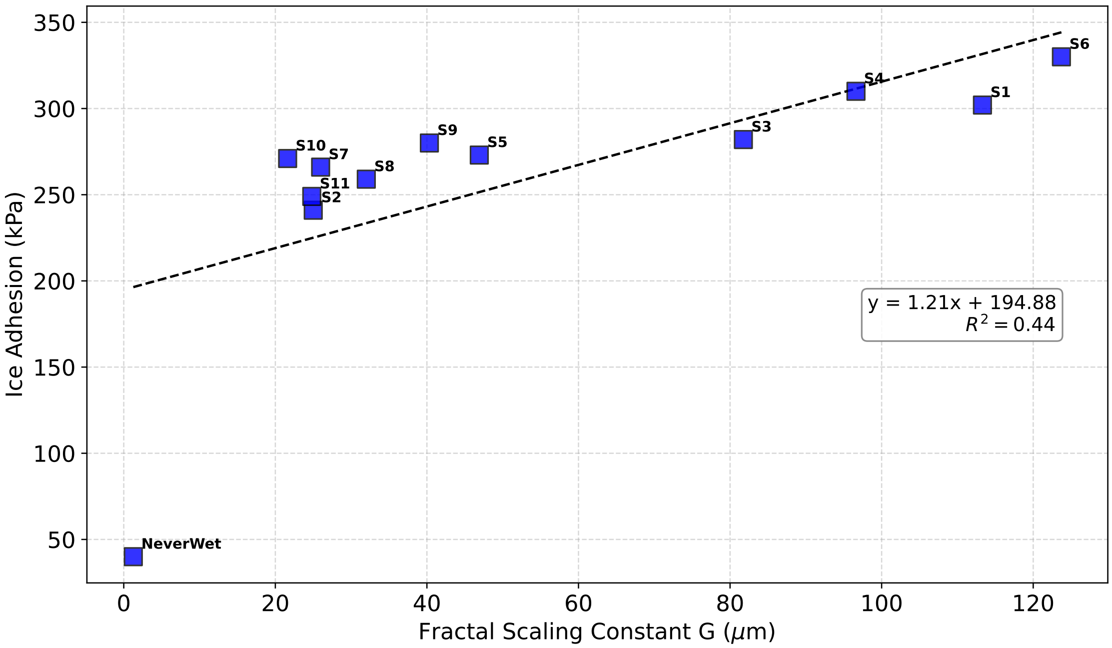

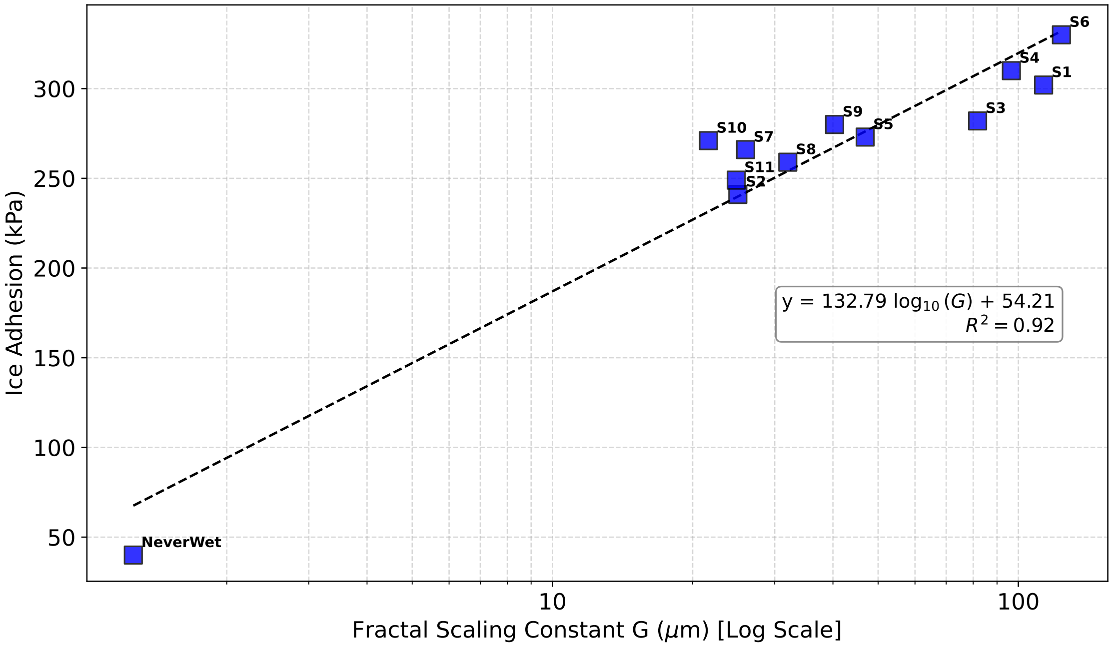

Figure 3.16: Ice adhesion strength as a function of scaling constant G plotted on (top) a linear scale and (bottom) a logarithmic scale.

Interplay of icing metrics and fractal descriptors: To further clarify the role of fractal geometry, we also examined how the icing dynamics vary with D and G. Figure 3.17 shows that surfaces with higher fractal dimension generally have longer freezing delay times. Among the SPS coatings, those with $D \approx 1.70$ sustain supercooled droplets roughly 1.5–2 times longer than those with $D \approx 1.55$ before freezing occurs. This positive correlation is consistent with the idea that a more intricate, fractal surface traps more insulating air beneath the droplet and reduces the solid fraction in contact, thereby slowing the heat transfer required for ice nucleation. In our dataset, coatings that combine high D with low G not only show lower adhesion (Figures 3.15 and 3.16), but also tend to sit at the long-delay end of Figure 3.17.

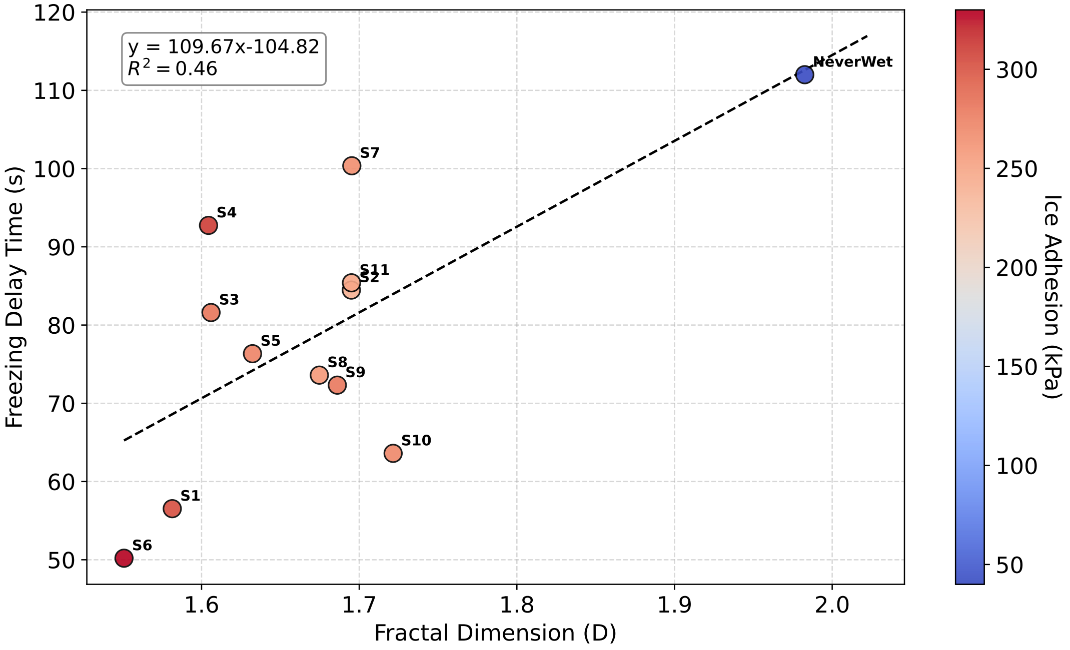

Figure 3.17: Freezing delay time as a function of fractal dimension D.

Dynamic droplet shedding follows the same qualitative pattern. From Table 3.4, surfaces with higher D and lower G (in particular, Sample 7 and NeverWet) are found at the lower end of the contact-time range, indicating faster droplet rebound, whereas coatings with lower D/higher G (such as Sample 6) show longer contact times. This is consistent with a reduction in contact-line pinning: surfaces with abundant micro–nano asperities and trapped air provide fewer continuous wetting paths, so an impacting droplet has less opportunity to dissipate energy and can recoil more easily. Finally, Figure 3.18 summarizes the interplay between D and G by plotting fractal dimension against scaling constant. The best-performing surfaces cluster in the quadrant of relatively high D and low G, further supporting the conclusion that a complex yet low-amplitude fractal texture is favourable for all three aspects of icephobic performance: low ice adhesion, long freezing delay, and short droplet contact time.

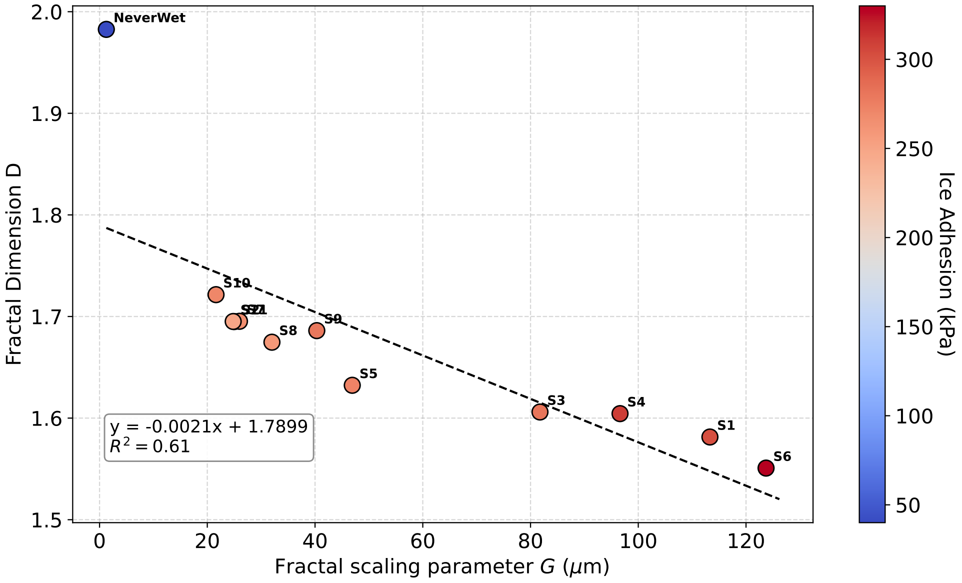

Figure 3.18: Fractal dimension D as a function of scaling constant G for all surfaces; marker colouring indicates ice-adhesion level.

In summary, the performance tests demonstrate that fractal descriptors correlate strongly with all aspects of icephobic behaviour. Neither traditional roughness averages nor contact angles alone can reliably distinguish the best from the worst performers among our superhydrophobic samples. By contrast, fractal dimension and scaling constant show clear, physically interpretable relationships with ice adhesion, freezing delay, and droplet bounce-off time. Surfaces that combine a high D with a low G consistently excel, whereas those lacking in either aspect exhibit at least one weakness (either freezing faster, retaining ice more strongly, or allowing droplets to linger longer on the surface).

3.3.3 Exploratory data analysis

To further interpret the experimental data, we performed an exploratory data analysis (EDA) examining the correlations among all measured surface characteristics and outcomes. Figure 3.19 presents a Pearson correlation matrix that includes surface roughness parameters, fractal parameters, wettability metrics, freezing delay, contact time, and ice adhesion.

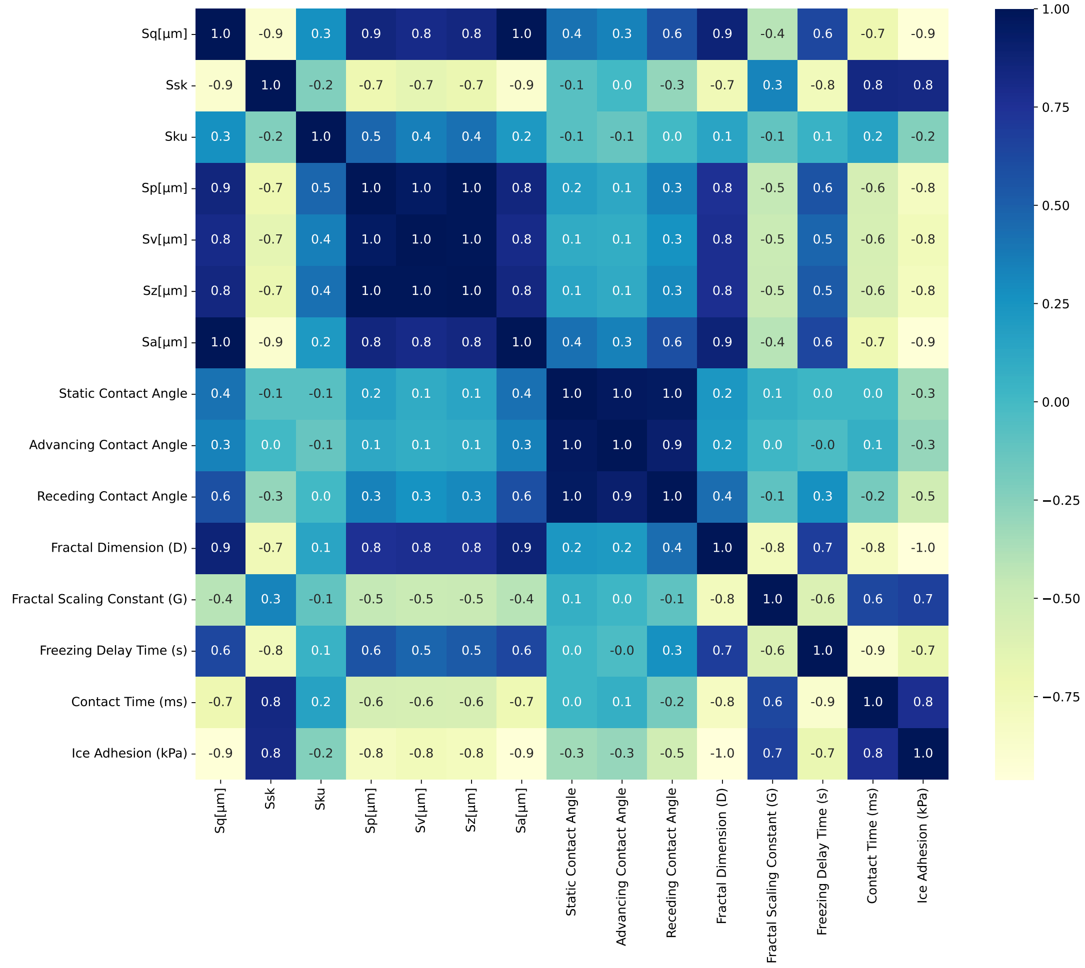

	Sq[µm]	Ssk	Sku	Sp[µm]	Sv[µm]	Sz[µm]	Sa[µm]	Static Contact Angle	Advancing Contact Angle	Receding Contact Angle	Fractal Dimension (D)	Fractal Scaling Constant (G)	Freezing Delay Time (s)	Contact Time (ms)	Ice Adhesion (kPa)
Sq[µm]	1.0	-0.9	0.3	0.9	0.8	0.8	1.0	0.4	0.3	0.6	0.9	-0.4	0.6	-0.7	-0.9
Ssk	-0.9	1.0	-0.2	-0.7	-0.7	-0.7	-0.9	-0.1	0.0	-0.3	-0.7	0.3	-0.8	0.8	0.8
Sku	0.3	-0.2	1.0	0.5	0.4	0.4	0.2	-0.1	-0.1	0.0	0.1	-0.1	0.1	0.2	-0.2
Sp[µm]	0.9	-0.7	0.5	1.0	1.0	1.0	0.8	0.2	0.1	0.3	0.8	-0.5	0.6	-0.6	-0.8
Sv[µm]	0.8	-0.7	0.4	1.0	1.0	1.0	0.8	0.1	0.1	0.3	0.8	-0.5	0.5	-0.6	-0.8
Sz[µm]	0.8	-0.7	0.4	1.0	1.0	1.0	0.8	0.1	0.1	0.3	0.8	-0.5	0.5	-0.6	-0.8
Sa[µm]	1.0	-0.9	0.2	0.8	0.8	0.8	1.0	0.4	0.3	0.6	0.9	-0.4	0.6	-0.7	-0.9
Static Contact Angle	0.4	-0.1	-0.1	0.2	0.1	0.1	0.4	1.0	1.0	1.0	0.2	0.1	0.0	0.0	-0.3
Advancing Contact Angle	0.3	0.0	-0.1	0.1	0.1	0.1	0.3	1.0	1.0	0.9	0.2	0.0	-0.0	0.1	-0.3
Receding Contact Angle	0.6	-0.3	0.0	0.3	0.3	0.3	0.6	1.0	0.9	1.0	0.4	-0.1	0.3	-0.2	-0.5
Fractal Dimension (D)	0.9	-0.7	0.1	0.8	0.8	0.8	0.9	0.2	0.2	0.4	1.0	-0.8	0.7	-0.8	-1.0
Fractal Scaling Constant (G)	-0.4	0.3	-0.1	-0.5	-0.5	-0.5	-0.4	0.1	0.0	-0.1	-0.8	1.0	-0.6	0.6	0.7
Freezing Delay Time (s)	0.6	-0.8	0.1	0.6	0.5	0.5	0.6	0.0	-0.0	0.3	0.7	-0.6	1.0	-0.9	-0.7
Contact Time (ms)	-0.7	0.8	0.2	-0.6	-0.6	-0.6	-0.7	0.0	0.1	-0.2	-0.8	0.6	-0.9	1.0	0.8
Ice Adhesion (kPa)	-0.9	0.8	-0.2	-0.8	-0.8	-0.8	-0.9	-0.3	-0.3	-0.5	-1.0	0.7	-0.7	0.8	1.0

Figure 3.19: Pearson correlation matrix between surface topography, wetting, freezing variables and ice-adhesion strength.

Several notable patterns emerge from the correlation matrix:

- Many of the standard roughness amplitude parameters (such as R_a, R_q, R_p, R_v, S_z, etc.) are highly intercorrelated (pairwise $|r| \approx$ 0.8–0.9). They essentially form a redundant block of information: a sample that is rough in terms of one parameter tends to be rough in terms of all. This is not surprising, as a surface with large peaks (high R_p) often also has a high average roughness R_a, high R_q, etc.

- These roughness parameters also showed strong positive correlation with the fractal dimension D. In our dataset, surfaces with higher D tended to have higher overall roughness amplitudes. This indicates that, while D captures something beyond a single-scale roughness, it is still related to the general magnitude of surface features. However, the fractal scaling constant G did not cluster with the R parameters; G was relatively independent, reflecting a different aspect of topography (feature height scaling rather than combined amplitude).

- Looking at icephobic performance metrics, ice adhesion had a negative correlation with fractal D (consistent with the earlier analysis) and positive correlation with G (i.e., lower G leads to lower adhesion). Ice adhesion also correlated moderately with freezing delay and contact time (surfaces with longer delays and shorter contact times tended to have lower adhesion), but these correlations were not as strong as those with the fractal parameters. This again highlights that fractal descriptors capture critical surface characteristics affecting ice adhesion.

- Interestingly, among the wettability metrics, the receding contact angle θ_R showed a stronger (negative) correlation with ice adhesion than did the static or advancing angles. In other words, surfaces with higher receding angles (and thus lower CAH) generally had lower ice adhesion. This makes sense because a high θ_R indicates that water has difficulty pinning on the surface, which is favorable for both shedding liquid droplets and preventing solid ice from anchoring. In fact, our feature importance analysis (described next) found that θ_R was more informative for predicting ice adhesion than θ_{static} or θ_A. This observation aligns with the idea that contact line mobility (low hysteresis) is more relevant to ice release than the initial droplet wettability.

We also carried out a preliminary feature importance analysis using a machine learning random forest regression model to gauge which variables were the most important predictors of ice adhesion in our dataset. The outcome (illustrated in Figure 3.20) was that the fractal parameters (D and

G) and the icing-related variables (freezing delay time and contact time) ranked at the top in importance. In particular, fractal dimension D was typically the single most important predictor, followed by the droplet contact time and freezing delay. The scaling constant G also had a significant contribution. Traditional roughness metrics (such as R_a) and static/advancing contact angles were ranked lower, implying they add comparatively less predictive value once fractal and dynamic wetting parameters are accounted for. This analysis reinforces our experimental findings: the fractal nature of the surface and its dynamic wetting behavior are the dominant factors governing ice adhesion. Notably, the receding angle (or conversely CAH) featured more prominently than the static angle, consistent with the correlation matrix insight that low CAH surfaces perform better in terms of ice adhesion. Although our dataset is limited in size, these trends align well with physical expectations and suggest that future data-driven models for icephobic surfaces should include fractal descriptors and dynamic wettability metrics as key input features.

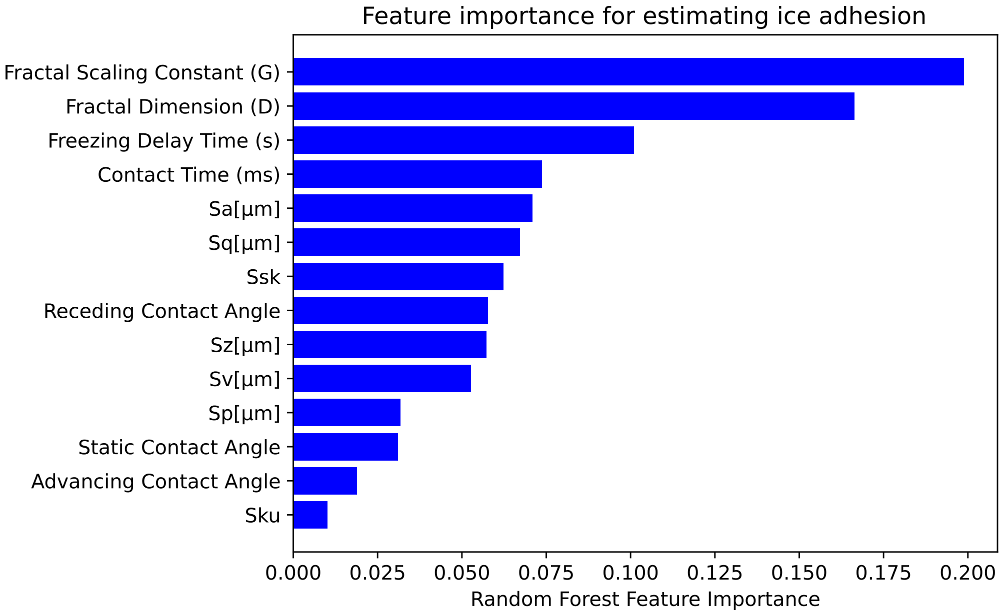

Figure 3.20: Feature-importance ranking from the baseline regression model, highlighting the dominant role of amplitude roughness parameters, geometric descriptor D, and freezing time compared with equilibrium contact angle.

3.4 Conclusion

In this study, a series of superhydrophobic TiO_2 coatings with diverse surface topographies were synthesized using the Suspension Plasma Spray (SPS) technique and benchmarked against a commercial NeverWet coating. Their icephobic behavior was quantified in terms of freezing delay time, droplet impact contact time, and shear ice-adhesion strength. The main conclusions are as follows:

(1) **Fractal parameters as key performance indicators:** The fractal dimension (D) and scaling constant (G) were found to be far more robust predictors of icephobic performance than the conventional static contact angle (SCA) and simple roughness amplitudes. Although all fabricated coatings were superhydrophobic, their performance in ice adhesion, freezing delay, and droplet repellency varied significantly. Neither SCA nor amplitude roughness metrics could reliably distinguish the best from the worst performers, whereas D and G showed clear and physically interpretable correlations with all three icing metrics and were ranked as the most important features in the Random-Forest analysis.

(2) **Topographical requirements for high icephobicity:** The results point to a common topographical signature for effective icephobic surfaces. Coatings with relatively high fractal dimension ($D \approx 1.7$ for the best SPS samples and $D \approx 2$ for NeverWet) and low scaling constant G (fine, low-amplitude asperities) consistently exhibited lower ice adhesion, longer freezing delay, and shorter droplet contact time than coatings with lower D and higher G. NeverWet represents an extreme case with very high D and very small G, yielding outstanding short-term icephobic response but limited mechanical durability; the SPS coatings approach this fractal regime while offering a more robust, thermally sprayed architecture.

(3) **Physical interpretation:** A higher fractal dimension corresponds to a more complex, multiscale surface that reduces the true solid–liquid/solid–ice contact fraction and promotes air entrapment. A lower scaling constant indicates that these features have small vertical amplitude, so the surface is "complex but relatively flat." This combination favours a stable

Cassie–Baxter state, which (i) provides an insulating air layer that delays freezing, (ii) reduces contact-line pinning and energy dissipation, enabling rapid droplet rebound, and (iii) minimizes the effective bond area, thereby lowering ice adhesion.

Overall, this work demonstrates that the strategic engineering of surface topography, quantified through fractal analysis, is central to developing advanced materials with superior icephobic properties. Rather than targeting high hydrophobicity alone, future anti-icing coatings should be designed to achieve an optimized fractal geometry—combining high D with low G—while maintaining sufficient mechanical robustness for practical applications.

Chapter 4

Summary and Future Work

4.1 Summary – Main Findings

This study addressed a critical knowledge gap by quantitatively linking surface roughness characteristics to icephobic performance in thermally sprayed coatings. The central hypothesis – that classical wettability metrics (such as static contact angle) are not reliable predictors of ice adhesion – was strongly supported by the results. Instead, a multifractal description of surface texture proved to be a robust framework for understanding and predicting anti-icing behavior. The major findings of the research can be summarized as follows:

- **Limited efficacy of conventional metrics:** All fabricated surfaces were superhydrophobic (static contact angle $> 150^{\circ}$), yet their measured ice adhesion strengths varied significantly. Traditional roughness and wettability indicators (including static contact angle and surface roughness) showed only weak and inconsistent correlations with ice adhesion force, freezing delay, or droplet rebound time. This confirms that surface hydrophobicity alone does not guarantee icephobicity; a smooth, water-repellent coating can still allow strong ice bonding.
- **Fractal descriptors as reliable predictors:** In contrast, scale-independent fractal parameters extracted from the surface profiles correlated strongly with icephobic performance. The fractal dimension D (which quantifies surface complexity) and the scaling constant G (feature size amplitude) emerged as effective predictors for all key metrics. Surfaces with higher D

and lower G consistently exhibited lower ice adhesion strength, longer freezing delays, and more rapid droplet bouncing (shorter contact times). These trends suggest that icephobic performance is governed by the multiscale organization of surface roughness rather than by any single scale of texture.

- **Optimal roughness regime identified:** An optimal design space in terms of fractal parameters was identified for minimizing ice adhesion. Coatings that combined a relatively high fractal dimension with a low scaling constant achieved the best icephobic outcomes. The best-performing thermally sprayed coatings fell in a parameter range (e.g., $D > 1.7$ and $G < 10\ \mu m$) that promotes a stable Cassie–Baxter wetting state with minimal real contact area.
- **Icephobic mechanism insights:** The enhanced performance of high-D/low-G surfaces can be attributed to their multi-scale roughness architecture. Such surfaces trap a layer of air within their asperities, effectively reducing the solid–liquid contact fraction and increasing the thermal resistance at the interface. This combination delays the initial ice nucleation and growth (by slowing heat transfer into the droplet) and also reduces ice–substrate adhesion by limiting anchor points. In practical terms, droplets impacting these fractal surfaces experience less contact-line pinning and lose less energy to the surface, resulting in faster rebound and less ice accumulation. Overall, these mechanisms lead to significantly lower forces required to dislodge ice, validating the benefit of multifractal surface design for passive anti-icing performance.

4.2 Future Work – Promising Research Directions

Building on the above findings, several avenues for future research are recommended to advance the development of icephobic coatings:

- **Computational design and simulation:** Leverage the established relationship between fractal parameters (D, G) and icing performance to design new surfaces *in experiment*. By using algorithms (e.g., Weierstrass–Mandelbrot functions or Fourier synthesis) to generate synthetic surface profiles with target fractal properties, one could simulate droplet impact and freezing processes on virtual surfaces. This approach would allow researchers to screen a wide range of roughness combinations computationally, identifying promising surface designs before committing to fabrication. Such simulation-driven exploration of the fractal design space can greatly reduce trial-and-error in coating development.

- **Broader material systems and machine learning:** Extend the multifractal analysis framework to a broader set of materials and coatings beyond the TiO_2/SPS system studied here. This could include other spray coatings, laser-textured or etched metals, icephobic polymers, and hybrid composites. By building a more diverse dataset of surfaces (with their corresponding D, G, and icing performance metrics), advanced machine learning (ML) techniques can be employed. ML algorithms (e.g., regression models or random forests) could identify deeper nonlinear correlations or interactions between surface parameters and icing outcomes. In the long term, a trained model might predict ice adhesion or freezing delay for a given set of fractal descriptors, enabling rapid optimization of coating recipes and process parameters.

- **Long-term durability studies:** A crucial next step is to assess the long-term durability of fractal-optimized icephobic surfaces under realistic operating conditions. Future work should investigate how repeated icing–deicing cycles, abrasion, erosion by particles, UV exposure, and other environmental stressors affect the surface fractal parameters (D and G) over time. Correlating the degradation of the surface texture with any loss in icephobic performance will help establish durability limits and guide the development of robust coatings. These studies will ensure that the proposed roughness designs remain effective after prolonged use in the field.

- **Hybrid and adaptive anti-icing approaches:** Another promising direction is to combine passive fractal-based coatings with active or adaptive de-icing technologies. For example, integrating self-healing materials into the coating could allow it to restore its critical microstructure after damage. Similarly, embedding micro-heaters or utilizing photothermal additives within a fractal-textured surface could provide on-demand de-icing capability while maintaining low intrinsic ice adhesion. Such hybrid systems (passive plus active) might achieve durable ultra-low ice adhesion with minimal energy input, offering practical solutions for aviation, wind turbines, and power lines in harsh icing environments.

In summary, this thesis establishes fractal analysis as a rigorous and practical tool for designing and evaluating icephobic surfaces. The multifractal approach provides a compact descriptor set (D, G) that captures the essential geometrical features governing ice adhesion. By extending this framework to a wider range of materials, operating conditions, and adaptive designs, researchers can accelerate the development of the next generation of anti-icing coatings and treatments. The insights gained here lay the groundwork for creating durable, high-performance icephobic surfaces that meet the demanding requirements of aerospace, energy, and infrastructure applications.

References

Ang, A. S. M., & Berndt, C. C. (2014). A review of testing methods for thermal spray coatings. *International Materials Reviews*, *59*(4), 179–223.

Binninger, R., Unmüßig, S., Vergez, M., Bartel, M., & Schäfer-Welsen, O. (2024). Customized measuring station for peltier modules. *Heliyon*, *10*(4).

Board, N. T. S. (2007). *Safety study: Aircraft icing* (Tech. Rep. No. NTSB/SS-07/01). NTSB.

Boyd, D., & Guinn, T. (2024). Deficiencies in safe practices by pilots operating general aviation aircraft in weather conducive for icing. *Journal of Aviation Technology and Engineering*, *13*(1), 2.

Bragg, M., Hutchison, T., & Merret, J. (2000). Effect of ice accretion on aircraft flight dynamics. In *38th aerospace sciences meeting and exhibit* (p. 360).

Brassard, J.-D., Laforte, C., Guerin, F., & Blackburn, C. (2017). Icephobicity: Definition and measurement regarding atmospheric icing. In *Contamination mitigating polymeric coatings* (pp. 123–143). Cham, Switzerland: Springer.

Britton, R., & Bond, T. (1991). A review of ice accretion data from a model rotor icing test and comparison with theory. In *29th aerospace sciences meeting* (p. 661).

Burdin, L., Brulez, A.-C., Mazurczyk, R., Leclercq, J.-L., & Benayoun, S. (2025). Proposal for a controlled humidity environment test bench for the accurate characterization of icephobic properties. *Micromachines*, *16*(7), 756.

Cannon, J. (1984). The fractal geometry of nature. by benoit b. mandelbrot. *The American Mathematical Monthly*, *91*(9), 594–598.

Cebeci, T., & Kafyeke, F. (2003). Aircraft icing [Journal Article]. *Annual review of fluid mechanics*, *35*(1), 11-21.

Chang, Y., Xiao, S., Yu, H., Ma, R., Skallerud, B. H., Zhang, Z., & He, J. (2024, August). Unraveling Ice–Solid Interface Rupture Dynamics: Insights from Molecular Dynamics Simulations. *Langmuir*, *40*(32), 17090–17097.

Chaudhury, M., & Kim, K. (2007). Shear-induced adhesive failure of a rigid slab in contact with a thin confined film. *The European Physical Journal E*, *23*(2), 175–183.

Chen, J., Liu, J., He, M., Li, K., Cui, D., Zhang, Q., . . . Song, Y. (2012). Superhydrophobic surfaces cannot reduce ice adhesion. *Applied Physics Letters*, *101*(11).

Chen, W., Huang, Z., Xiao, T., Jiang, L., Tan, X., & Lei, Y. (2025). Advancing superhydrophobic surfaces: From mechanism insights and design strategies to intelligent applications. *APL Materials*, *13*(6).

Chen, X., Wang, Y.-F., Yang, Y.-R., Wang, X.-D., & Lee, D.-J. (2023). Contact time of droplet impact on superhydrophobic cylindrical surfaces with a ridge. *Langmuir*, *39*(50), 18644–18653.

Collins, C. M., & Safiuddin, M. (2022). Lotus-leaf-inspired biomimetic coatings: different types, key properties, and applications in infrastructures. *Infrastructures*, *7*(4), 46.

Corcione, S., De Marco, A., & Cusati, V. (2024). A cost-efficient predictive method for aerodynamic performance degradation of horizontal tail under icing conditions.

Debnath, L. (2006). A brief historical introduction to fractals and fractal geometry. *International Journal of Mathematical Education in Science and Technology*, *37*(1), 29–50.

Dhyani, A., Choi, W., Golovin, K., & Tuteja, A. (2022). Surface design strategies for mitigating ice and snow accretion. , *5*(5), 1423–1454.

Ensikat, H. J., Ditsche-Kuru, P., Neinhuis, C., & Barthlott, W. (2011). Superhydrophobicity in perfection: the outstanding properties of the lotus leaf. *Beilstein journal of nanotechnology*, *2*(1), 152–161.

Espallargas, N. (2015). Introduction to thermal spray coatings. In *Future development of thermal spray coatings* (pp. 1–13). Elsevier.

Farabello, L., Scarabino, A., & Bacchi, F. (2024, 12). Numerical analysis of ice accretion on an airfoil: A case study. *Revista Facultad de Ingeniería*, *115*. doi: 10.17533/udea.redin

.20241145

Farahani, E., Liberati, A. C., Mahdavi, A., Stoyanov, P., Moreau, C., & Dolatabadi, A. (2023). Ice adhesion evaluation of ptfe solid lubricant film applied on tio2 coatings. *Coatings*, *13*(6), 1049.

Farhadi, S., Farzaneh, M., & Kulinich, S. A. (2011). Anti-icing performance of superhydrophobic surfaces. *Applied Surface Science*, *257*(14), 6264–6269.

Farzaneh, M. (2008). *Atmospheric icing of power networks*. London, UK: Springer.

Fauchais, P. L., Heberlein, J. V., & Boulos, M. I. (2014). *Thermal spray fundamentals: from powder to part*. Springer Science & Business Media.

Federal Aviation Administration. (2021). *Advisory circular 20-117: Hazard potential of aircraft ice accumulation.* (Current revision, accessed 2025-05-31)

Gaddis, M. E., & Zyda, M. J. (1986). *The fractal geometry of nature; its mathematical basis and application to computer graphics* (Tech. Rep.).

Gao, L., & et al. (2021). A field study of ice accretion and its effects on the power production of utility-scale wind turbines. *Renewable Energy*, *167*, 917–928.

Gent, R. W., Dart, N. P., & Cansdale, J. T. (2000). Aircraft icing. *Philosophical Transactions of the Royal Society of London. Series A: Mathematical, Physical and Engineering Sciences*, *358*(1776), 2873–2911.

Ge-Zhang, S., Cai, T., Yang, H., Ding, Y., & Song, M. (2022). Biology and nature: Bionic superhydrophobic surface and principle. *Frontiers in Bioengineering and Biotechnology*, *10*, 1033514.

Ghatak, A., & Chaudhury, M. K. (2003). Adhesion-induced instability patterns in thin confined elastic film. *Langmuir*, *19*(7), 2621–2631.

Giannuzzi, G., Gaudiuso, C., Di Mundo, R., Mirenghi, L., Fraggelakis, F., Kling, R., … Ancona, A. (2019). Short and long term surface chemistry and wetting behaviour of stainless steel with 1d and 2d periodic structures induced by bursts of femtosecond laser pulses. *Applied Surface Science*, *494*, 1055–1065.

Golding, W. L. (2004). In-flight icing and how airlines are coping. *Journal of Aviation/Aerospace Education & Research*, *13*(3), 5.

Golovin, K., Dhyani, A., Thouless, M. D., & Tuteja, A. (2019). Low-interfacial-toughness materials for effective large-scale deicing. *Science*, *364*, 371–375.

Golovin, K., Kobaku, S. P. R., Lee, D. H., DiLoreto, E. T., Mabry, J. M., & Tuteja, A. (2016). Designing durable icephobic surfaces. *Science Advances*, *2*(3), e1501496.

Goodhand, M. N., Walton, K., Blunt, L., Lung, H. W., Miller, R. J., & Marsden, R. (2016). The limitations of using "ra" to describe surface roughness. *Journal of Turbomachinery*, *138*(10), 101003.

Grzegorczyk, K., Wajszczak, E., & Galas, D. (2013). The issue of icing in aviation. study with the use of numerical simulation. *Advances in Science and Technology. Research Journal*, *7*(17), 42–46.

Guan, Y., Liu, S., & Zhang, Y. (2024, 03). The origin, development, and application of fractal geometry theory in architecture. *Theoretical and Natural Science*, *31*, 42-49. doi: 10.54254/2753-8818/31/20240914

Gupta, G., Tyagi, R., Rajput, S., Maan, R., Jacob, S., & Verma, S. (2021). Review on thermal spray coating methods and property of different types of metal-based coatings. In *Advances in engineering materials: Select proceedings of flame 2020* (p. 427-439). Springer.

Hatte, S., Kant, K., & Pitchumani, R. (2023). Freezing characteristics of a water droplet on a multiscale superhydrophobic surface. *Langmuir*, *39*(33), 11898–11909.

He, Z., Zhuo, Y., Zhang, Z., & He, J. (2021). Design of icephobic surfaces by lowering ice adhesion strength: A mini review. *Coatings*, *11*(11). doi: 10.3390/coatings11111343

Homola, M. C., Virk, M. S., Wallenius, T., Nicklasson, P. J., & Sundsbø, P. A. (2010). Effect of atmospheric temperature and droplet size variation on ice accretion of wind turbine blades. *Journal of wind engineering and industrial aerodynamics*, *98*(12), 724–729.

Hoshian, S., Jokinen, V., Somerkivi, V., Lokanathan, A. R., & Franssila, S. (2015). Robust superhydrophobic silicon without a low surface-energy hydrophobic coating. *ACS applied materials & interfaces*, *7*(1), 941–949.

Jacobs, T. D., Pastewka, L., & Editors, G. (2022). Surface topography as a material parameter. *MRS bulletin*, *47*(12), 1205–1210.

Jain, R., & Pitchumani, R. (2017). Fractal model for wettability of rough surfaces. *Langmuir*, *33*(28), 7181–7190.

Jiang, J., Shen, Y., Xu, Y., Wang, Z., Tao, J., Liu, S., … Chen, H. (2024). An energy-free strategy to elevate anti-icing performance of superhydrophobic materials through interfacial airflow manipulation. *Nature Communications*, *15*(1), 777.

Josyula, T., Kumar Malla, L., Thomas, T. M., Kalichetty, S. S., Sinha Mahapatra, P., & Pattamatta, A. (2024). Fundamentals and applications of surface wetting. *Langmuir*, *40*(16), 8293–8326.

Jung, S., Dorrestijn, M., Raps, D., Das, A., Megaridis, C. M., & Poulikakos, D. (2011). Are superhydrophobic surfaces best for icephobicity? *Langmuir*, *27*(6), 3059–3066.

Koivuluoto, H., Hartikainen, E., & Niemelä-Anttonen, H. (2020). Thermally sprayed coatings: Novel surface engineering strategy towards icephobic solutions. *Materials*, *13*(6), 1434. doi: 10.3390/ma13061434

Krantz, S. G. (1989). Fractal geometry. *The Mathematical Intelligencer*, *11*(4), 12–16.

Kreder, M. J., Alvarenga, J., Kim, P., & Aizenberg, J. (2016a). Design of anti-icing surfaces: Smooth, textured or slippery? *Nature Reviews Materials*, *1*(1), 15003.

Kreder, M. J., Alvarenga, J., Kim, P., & Aizenberg, J. (2016b). Design of anti-icing surfaces: smooth, textured or slippery? *Nature Reviews Materials*, *1*(1), 1–15.

Krishnan, A., Liu, Y.-H., Cha, P., Woodward, R., Allara, D., Vogler, E. A., et al. (2005). An evaluation of methods for contact angle measurement. *Colloids and Surfaces B: Biointerfaces*, *43*(2), 95–98.

Kulinich, S. A., & Farzaneh, M. (2009). How wetting hysteresis influences ice adhesion strength on superhydrophobic surfaces. *Langmuir*, *25*(16), 8854–8856.

Kumar, R., & Kumar, S. (2018). International journal of engineering sciences & research technology thermal spray coating: a study 1. *Int. J. Eng. Sci. Res. Technol.*, *7*, 610–617.

Kuroda, S., Kawakita, J., Watanabe, M., & Katanoda, H. (2008). Warm spraying—a novel coating process based on high-velocity impact of solid particles. *Science and technology of advanced materials*.

Kwok, D. Y., & Neumann, A. W. (1999). Contact angle measurement and contact angle interpretation. *Advances in colloid and interface science*, *81*(3), 167–249.

Laforte, C., Brassard, J.-D., & Volat, C. (2019). Extended evaluation of icephobic coating regarding their field of application. In *Proc. international workshop on atmospheric icing of structures (iwais).* Reykjavik, Iceland.

Laforte, J.-L., Allaire, M.-A., & Laflamme, J. (1998). State-of-the-art on power line de-icing. *Atmospheric Research*, *46*(1), 143–158.

Lafuma, A., & Quéré, D. (2003). Superhydrophobic states. *Nature Materials*, *2*, 457–460.

Łatka, L. (2018). Thermal barrier coatings manufactured by suspension plasma spraying-a review. *Advances in Materials Science*, *18*(3), 95–117.

Łatka, L., Pawłowski, L., Winnicki, M., Sokołowski, P., Małachowska, A., & Kozerski, S. (2020). Review of functionally graded thermal sprayed coatings. *Applied Sciences*, *10*(15), 5153.

Latthe, S. S., Terashima, C., Nakata, K., & Fujishima, A. (2014). Superhydrophobic surfaces developed by mimicking hierarchical surface morphology of lotus leaf. *Molecules*, *19*(4), 4256–4283.

Li, B., Bai, J., He, J., Ding, C., Dai, X., Ci, W., … Yuan, Y. (2023). A review on superhydrophobic surface with anti-icing properties in overhead transmission lines. *Coatings*, *13*(2). doi: 10.3390/coatings13020301

Li, C.-J., Yang, G.-J., & Li, C.-X. (2013). Development of particle interface bonding in thermal spray coatings: a review. *Journal of thermal spray technology*, *22*(2), 192–206.

Li, S., & Paoli, R. (2022). Aircraft icing severity evaluation. *Encyclopedia*, *2*(1), 56–69. doi: 10.3390/encyclopedia2010005

Liu, X. Y. (2000). Heterogeneous nucleation or homogeneous nucleation? *The Journal of Chemical Physics*, *112*(22), 9949–9955.

Maghsoudi, K., Momen, G., & Jafari, R. (2023). The thermodynamic stability of the cassie–baxter regime determined by the geometric parameters of hierarchical superhydrophobic surfaces. *Applied Materials Today*, *34*, 101893. doi: https://doi.org/10.1016/j.apmt.2023.101893

Makkonen, L., Lehtonen, P., & Hirviniemi, M. (2014). Determining ice loads for tower structure design. *Engineering Structures*, *74*, 229–232.

Menini, R., & Farzaneh, M. (2011). Advanced icephobic coatings. *Journal of Adhesion Science and Technology*, *25*(7), 971–992.

Milani, Z. R., Matida, E., Razavi, F., Ronak Sultana, K., Timothy Patterson, R., Nichman, L., …

Bala, K. (2024). Numerical icing simulations of cylindrical geometry and comparisons to flight test results. *Journal of Aircraft*, *61*(4), 1272–1282.

Milles, S., Vercillo, V., Alamri, S., Aguilar-Morales, A. I., Kunze, T., Bonaccurso, E., & Lasagni, A. F. (2021). Icephobic performance of multi-scale laser-textured aluminum surfaces for aeronautic applications. *Nanomaterials*, *11*(1), 135.

Mohammadi, M., De Pauw, D., Tembely, M., & Dolatabadi, A. (2013). Droplet impact and solidification on hydrophilic and superhydrophobic substrates in icing conditions. In *43rd aiaa fluid dynamics conference* (p. 2486).

Mohseni, M., Recla, L., Mora, J., García Gallego, P., Agüero, A., & Golovin, K. (2021). Quasicrystalline coatings exhibit durable low interfacial toughness with ice. *ACS Applied Materials & Interfaces*, *13*(30), 36517–36526. doi: 10.1021/acsami.1c08740

Mora, J., García, P., Muelas, R., & Agüero, A. (2020). Hard quasicrystalline coatings deposited by hvof thermal spray to reduce ice accretion in aero-structures components. *Coatings*, *10*(3), 290. doi: 10.3390/coatings10030290

Nguyen, T. B., Park, S., & Lim, H. (2018). Effects of morphology parameters on anti-icing performance in superhydrophobic surfaces. *Applied Surface Science*, *435*, 585–591.

Nistal, A., Sierra-Martín, B., & Fernández-Barbero, A. (2024). On the durability of icephobic coatings: A review. *Materials*, *17*(1), 235.

Nohooji, S. G., & Tembely, M. (2025). Analysis of electro-thermal de-icing on a naca0012 airfoil under harsh sld conditions and different angles of attack. *Aerospace*, *12*(10). doi: 10.3390/aerospace12100883

Nosonovsky, M., & Hejazi, V. (2012). Why superhydrophobic surfaces are not always icephobic. *ACS Nano*, *6*(10), 8488–8491.

Parent, O., & Ilinca, A. (2011). Anti-icing and de-icing techniques for wind turbines: Critical review. *Cold Regions Science and Technology*, *65*(1), 88–96.

Parvate, S., Dixit, P., & Chattopadhyay, S. (2020). Superhydrophobic surfaces: insights from theory and experiment. *The Journal of Physical Chemistry B*, *124*(8), 1323–1360.

Petty, K. R., & Floyd, C. D. (2004). A statistical review of aviation airframe icing accidents in the us. In *Proceedings of the 11th conference on aviation, range, and aerospace hyannis.*

Piscitelli, F., Fanciullo, M., Sarcinella, A., Costantini, M., & Frigione, M. (2025). Icephobic properties of superhydrophobic coatings developed for aeronautical applications. *Coatings*, *15*(6), 621.

Ratvasky, T., Barnhart, B., & Lee, S. (2008). *Current methods for modeling and simulating icing effects on aircraft performance. stab. control* (Report). NASA/TM-2008-215453.

Reehorst, A. L., Jr., H. E. A., & Colantonio, R. O. (2010, August). Examination of icing induced loss of control and its mitigations. In *Aiaa atmospheric and space environments conference.* Toronto, Ontario, Canada. (AIAA Paper 2010-8140) doi: 10.2514/6.2010-8140

Ringdahl, S., Xiao, S., He, J., & Zhang, Z. (2021). Machine learning based prediction of nanoscale ice adhesion on rough surfaces. *Coatings*, *11*(1), 33.

Safety, A. (2010). Preliminary information on aircraft icing and winter operations. *AVIATION SAFETY*.

Samayoa, D., Garcia-Otamendi, E. I., & Balankin, A. S. (2025). Fractal geometry: Historical and conceptual background.

Sarshar, M. A., Song, D., Swarctz, C., Lee, J., & Choi, C.-H. (2018). Anti-icing or deicing: Icephobicities of superhydrophobic surfaces with hierarchical structures. *Langmuir*, *34*(46), 13821–13827.

Schaefer, S., Levin, D., & Goldman, R. (2005). Subdivision schemes and attractors. In *Symposium on geometry processing* (pp. 171–180).

Schutzius, T. M., Jung, S., Maitra, T., Graeber, G., Köhme, M., & Poulikakos, D. (2015). Spontaneous droplet trampolining on rigid superhydrophobic surfaces. *Nature*, *527*(7576), 82–85.

Sharifi, N., Dolatabadi, A., Pugh, M., & Moreau, C. (2019). Anti-icing performance and durability of suspension plasma sprayed tio_2 coatings. *Cold Regions Science and Technology*, *159*, 1–12. doi: 10.1016/j.coldregions.2018.11.018

Sharifi, N., Ettouil, F. B., Moreau, C., Dolatabadi, A., & Pugh, M. (2017). Engineering surface texture and hierarchical morphology of suspension plasma sprayed tio2 coatings to control wetting behavior and superhydrophobic properties. *Surface and Coatings Technology*, *329*, 139–148.

Singh, H., Sidhu, T., & Kalsi, S. (2012). Cold spray technology: future of coating deposition processes. *Fracture and Structural Integrity*, *6*(22), 69–84.

Sojoudi, H., Wang, M., Boscher, N., McKinley, G. H., & Gleason, K. K. (2016). Durable and scalable icephobic surfaces: similarities and distinctions from superhydrophobic surfaces. *Soft matter*, *12*(7), 1938–1963.

Sun, Z. X., Liu, H., Li, H. Q., & Zhang, Y. (2024). Unsteady aerodynamics of an oscillating airfoil with leading-edge horn-ice shape. *Available at SSRN 5044637*.

Susoff, M., Siegmann, K., Pfaffenroth, C., & Hirayama, M. (2013). Evaluation of icephobic coatings: Screening of different coatings and influence of roughness. *Applied Surface Science*, *282*, 870–879.

Tejero-Martin, D., Rezvani Rad, M., McDonald, A., & Hussain, T. (2019). Beyond traditional coatings: a review on thermal-sprayed functional and smart coatings. *Journal of thermal spray technology*, *28*(4), 598–644.

Vaßen, R., Kaßner, H., Mauer, G., & Stöver, D. (2010). Suspension plasma spraying: process characteristics and applications. *Journal of thermal spray technology*, *19*(1), 219–225.

Wang, L., Li, D., Jiang, G., Hu, X., Peng, R., Song, Z., … Zhong, M. (2024). Dual-energy-barrier stable superhydrophobic structures for long icing delay. *ACS nano*, *18*(19), 12489–12502.

Wang, Y., Li, J., Song, H., Wang, F., Su, X., Zhang, D., & Xu, J. (2025). Biomimetic superhydrophobic surfaces: From nature to application. *Materials*, *18*(12), 2772.

Wang, Z., Kong, J., Zhou, Q., & Chen, X. (2022). Natural superhydrophobic surfaces and application. In *Journal of physics: Conference series* (Vol. 2390, p. 012115).

Wong, T.-S., Kang, S. H., Tang, S. K. Y., Smythe, E. J., Hatton, B. D., Grinthal, A., & Aizenberg, J. (2011). Bioinspired self-repairing slippery surfaces with pressure-stable omniphobicity. *Nature*, *477*(7365), 443–447.

Yamazaki, M., Jemcov, A., & Sakaue, H. (2021). A review on the current status of icing physics and mitigation in aviation. *Aerospace*, *8*(7), 188.

Yang, Q., Au, S., Dijvejin, Z. A., Zarasvand, K. A., Dolatabadi, A., & Golovin, K. (2025). Superhydrophobic surfaces exhibiting low interfacial toughness with ice. *Chemical Engineering Journal*, *508*, 160929.

Yeadon, K., Lai, E. P. C., Huang, X., & Song, N. (2025). Influence of surface roughness and metal oxide nanoparticles on airframe with icephobic coatings. , *2*(1), 82–93. (Publisher: RSC) doi: 10.1039/D4LF00279B

Zdero, R., & Turan, O. F. (2010). The effect of surface strands, angle of attack, and ice accretion on the flow field around electrical power cables. *Journal of wind engineering and industrial aerodynamics*, *98*(10-11), 672–678.

Zhan, Y., Pang, Z., & Tan, G. (2025). Advances in icephobic coatings: Concepts, mechanisms, classifications and prospects. *Cold Regions Science and Technology*, *239*, 104596.

Zhang, Y., Yu, X., Wu, H., & Wu, J. (2012). Facile fabrication of superhydrophobic nanostructures on aluminum foils with controlled-condensation and delayed-icing effects. *Applied Surface Science*, *258*, 8253–8257.